# OPTICAL PERFORMANCE OF RANDOM ANTIREFLECTION STRUCTURED SURFACES ON NON-VITREOUS SUBSTRATES AND FUSED SILICA MICROLENS ARRAYS

by

Abigail Peltier Eckart

A dissertation submitted to the faculty of
The University of North Carolina at Charlotte
in partial fulfillment of the requirements
for the degree of Doctor of Philosophy in
Optical Science and Engineering

Charlotte

2018

Approved by:

_____
Dr. Menelaos Poutous

_____
Dr. Glenn Boreman

_____
Dr. Tino Hofmann

_____
Dr. Michael Fiddy

_____
Dr. Ryan Adams

# ABSTRACT

ABIGAIL PELTIER ECKART. Optical Performance of Random Antireflection Structured Surfaces on Non-Vitreous Substrates and Fused Silica Microlens Arrays. (Under the direction of DR. MENELAOS K. POUTOUS)

Random anti-reflection surface structures (rARSS) are randomly spaced, densely packed, sub-wavelength cylindrical or conical features that are fabricated on the surface of optical substrates. As light passes from the superstrate to the substrate medium through the rARSS, it propagates in a gradually increasing ratio of glass to air volume fraction, effectively reducing or eliminating Fresnel reflection. Studies found in the literature to date focus on fabricating and testing rARSS on planar substrates, and typically provide normal incidence transmission or reflection measurements over a variable wavelength range. In this work, rARSS are first fabricated on planar fused silica substrates through a metal mask reactive ion etching (RIE) process. Granulometry values, roughness measurements, and spectroscopy data are presented relating the physical characteristics of the gold mask statistical populations, and the resulting rARSS features population, as well as spectral transmission properties of the final surfaces. The rARSS silica fabrication process is attempted on non-vitreous substrates, using three different fabrication methods, and the results are evaluated using spectral transmission measurements, SEM images, and laser confocal microscope images. These results show that the silica rARSS fabrication process is not transferrable to non-vitreous materials. Finally, the rARSS fabrication process for planar fused silica samples is applied to microlens arrays (MLA) of varying aspect ratio, and found to be transferrable. The focal spot of each MLA is measured using a beam profiler and compared to simulated and unprocessed MLA results. Transmission

enhancement for rARSS processed MLAs is verified to be comparable to processed fused silica flats, and the propagation characteristics of the beam through focus are shown to be unchanged by the application of the rARSS. Tests are also performed to look at the far-field propagation characteristics of the unprocessed and rARSS processed MLAs by examining their Fourier transforms. It is shown that the rARSS processed MLAs have only slight differences in their far-field diffraction response compared to unprocessed MLAs, indicating that rARSS can be applied to MLAs without negatively affecting the lens' wavefront propagation properties or focusing abilities.

# DEDICATION

This dissertation is dedicated to…

…my parents, who have always been, and continue to be, the most amazing role models. I would not have made it this far without their constant unconditional support and encouragement.

…my sister, Julia, who has always been willing to participate in my crazy ideas and is available any time I need her, armed with a creative pep talk.

…my husband, Chris, who has been my rock throughout this long graduate school process. His love, patience, and unwavering dedication to keeping me fed and well rested have kept me going when I thought of giving up.

# ACKNOWLEDGMENTS

First and foremost, I would like to thank my advisor, Dr. Menelaos Poutous for his guidance and encouragement over the last five years. His support has been invaluable and I am grateful for all of the time and energy he has given to me in my time at UNC Charlotte. I would also like to thank my committee members, Dr. Glenn Boreman, Dr. Michael Fiddy, Dr. Tino Hofmann, and Dr. Ryan Adams for their feedback and advice throughout the dissertation process. I greatly appreciate all of the time my committee has invested in me.

Thank you to Dr. Ishwar Aggarwal, the Naval Research Laboratory, and the Science, Mathematics, & Research for Transformation (SMART) Scholarship for funding me during my graduate school career. I know that I am incredibly lucky to have been given such generous financial support and that without it completing this dissertation would have been much more difficult.

I would also like to thank the Center for Optoelectronics and Optical Communications for the use of its equipment and facilities. Thank you also to Dr. Robert Hudgins, Dr. Lou Deguzman, and Mr. Scott Williams for their patient training sessions and frequent help with equipment issues.

Thank you to the past and present members of the Optical Micro-Structured Interfaces Laboratory, Kevin Major, Courtney Taylor, Karteek Kunala, Jason Case, Gopal Sapkota, Chris Wilson, Tom Hutchins, Anton Chernenko, and Raj Joshi, for all of the training, troubleshooting, brainstorming, and general support they've given me. I consider myself very lucky to have had such a supportive lab team.

And finally, I'm incredibly grateful to all of my friends and family who have been

so confident in my abilities even when my own confidence was lacking. I'd especially like to thank my husband, Chris, my parents, and my sister Julia, who have all listened to more optics talk than any of them could ever have wanted to hear. The four of you have been there for me through all the ups and downs that graduate school brings, and I truly could not have done this without you.

TABLE OF CONTENTS

LIST OF TABLES xi

LIST OF FIGURES xii

LIST OF ABBREVIATIONS xxiii

CHAPTER 1: INTRODUCTION 1

1.1 Anti-Reflection Methods 1

1.2 Introduction to Reactive Ion Etching (RIE) 7

1.3 Physical and Chemical Deposition Methods 10

1.4 Testing rARSS Performance and Properties 12

1.5 Introduction to Microlens Arrays (MLAs) 17

1.6 Dissertation Overview 19

CHAPTER 2: FABRICATION TECHNIQUES AND TESTING 22

2.1 Introduction 22

2.2 Spectral Transmission Enhancement Properties of Random Anti-Reflecting Surface Structures Fabricated on Vitreous Substrates 23

2.2.1 Introduction 23

2.2.2 Fabrication, Transmission Enhancement, and Surface Characterization 24

2.2.3 Summary 32

2.3 rARSS Fabrication on Non-Vitreous Materials: Difficulties and Potential Solutions 32

2.3.1 Introduction 32

2.3.2 Spinel Results 33

2.3.3 Initial Testing of PECVD Deposited $SiO_2$ and Etching 35

2.3.4 Summary 40

2.4 Gradient-Optical-Index Porous (GrIP) Coatings by Layer Co-Deposition and Sacrificial Material Removal 41

2.4.1 Introduction 41

2.4.2 Fabrication of GrIP Coatings 42

2.4.3 Results and Discussion 47

2.4.4 Summary 61

2.5 Summary of Fabrication Methods Chapter 61

CHAPTER 3: INVESTIGATION OF THE OPTICAL PERFORMANCE OF MICROLENS ARRAYS PROCESSED WITH RANDOM ANTI-REFLECTION STRUCTURED SURFACES 63

3.1 Introduction 63

3.2 Fabrication of rARSS on Fused Silica Microlens Arrays 67

3.2.1 Fabrication Steps 67

3.2.2 Scanning Electron Microscope Images and Granulometry Results 70

3.3 Microlens Array Focal Spot and Beam Propagation Testing 77

3.3.1 Microlens Array Focal Spot Imaging System: Simulations and Tests 77

3.3.2 Microlens Array Beam Propagation Tests 82

3.3.3 Microlens Array Transmission Enhancement Tests 85

3.4 Investigating the Far-Field Diffraction of Microlens Arrays with rARSS 87

3.4.1 Experimental Setup and Analysis 87

3.4.2 Fourier Transform Results and Analysis 90

3.5 Summary of Microlens Array Optical Performance Chapter 97

CHAPTER 4: CONCLUSIONS 99

4.1 Summary of the Optical Performance of Random Antireflection Structured Surfaces on Planar Substrates 99

4.2 Summary of the Optical Performance of Random Antireflection Structured Surfaces on Microlens Arrays 102

4.3 Potential Future Work 103

REFERENCES 105

APPENDIX A: PUBLICATIONS AND PRESENTATIONS 109

APPENDIX B: LIST OF OPTICAL COMPONENTS FOR MLA TESTING 110

APPENDIX C: FOURIER TRANSFORM FOR A SINGLE MICROLENS PROFILE: ANALYTICAL SOLUTION 111

LIST OF TABLES


| | | |
|---|---|---|
| TABLE 1: | Measurement methodology for each fused silica sample tested, after each of the three main process steps. | 24 |
| TABLE 2: | Etch parameters used on the PlasmaTherm RIE 7000 tool for etches that resulted in the successful roughening of a PECVD deposited thin film of $SiO_2$ on silicon. | 39 |
| TABLE 3: | Thermal conductivity and specific heat capacity values for the four substrates used in the GrIP coating tests. These values were compiled from several references [49, 61-63]. | 52 |
| TABLE 4: | Wavelength ranges over which the measured TE is positive (transmission is higher than unprocessed spinel) and over which the measured TE is >3% (arbitrarily selected baseline). The results shown are for each deposition on spinel, and are only for the etches with the highest transmission values (found in Fig. 32). Deposition III does not have TE higher than 3% at any point. | 56 |
| TABLE 5: | Specifications for the MLAs used in Chapter 3. | 66 |
| TABLE 6: | Distances shown in Fig. 42 for each MLA for measurements taken at focus. As the beam profile was observed through focus, the LP value would decrease. | 79 |

LIST OF FIGURES


| | | |
|---|---|---|
| FIGURE 1: | A schematic of a single layer anti-reflective thin film and refractive index profile with propagation distance into the material (z). If the thin film is of the appropriate refractive index (ideally $\sqrt{n_{substrate}}$ for materials in air) and the appropriate thickness (an odd multiple of λ/4) then the light reflecting from the top and bottom surfaces of the film will destructively interfere, reducing or eliminating the specular reflection. | 2 |
| FIGURE 2: | Simulation of transmission from a perfect AR thin film (PAR) applied to both sides of a fused silica (FS) substrate. In this simulation the index of the thin film is equal to the square root of the refractive index of FS and the thickness is 159nm. The plot on the left shows how the transmission changes with wavelength at normal incidence, and the plot on the right shows how the transmission changes with incident angle at 780 nm (the peak transmission wavelength). | 3 |
| FIGURE 3: | Simulations performed in VirtualLab, using a planar air/fused silica boundary, a periodic rectangular subwavelength grating and a periodic triangular subwavelength grating each optimized for minimum reflectivity at 1000 nm wavelength. The graphs show how the reflection efficiency changes with wavelength from 200 nm to 4000 nm for the p polarization (left) and s polarization (right). The purple lines are the plane air-FS boundary, the red lines are the rectangular grating, and the blue lines are the triangular grating. Graphics included on the plots show schematics of the grating shapes for each configuration. | 4 |
| FIGURE 4: | Schematic depicting rARSS on a substrate, and the increasing refractive index with propagation distance into the material *n(z).* In fabricated rARSS the refractive index profile of the features does not have to be linear as depicted here. | 5 |
| FIGURE 5: | Schematic depicting the common process steps for fabricating periodic surface structures onto a substrate. The diagram is adapted from a figure found in Ref. [10]. It should be noted that step 3 can be interference, | 6 |

conventional, or direct-write lithography.

FIGURE 6: Flow chart depicting the steps involved in the three methods of top-down fabrication of rARSS found in the literature. The pre-masking method is evaluated in this dissertation in Chapter 2. Representative SEM images that depict samples at the metallization, rapid thermal annealing (RTA $\Theta$), and final rARSS substrate steps in the fabrication process are included in the illustration [17]. 7

FIGURE 7: Measured spectral transmission data for an unprocessed fused silica substrate (black line) and fused silica samples processed with rARSS on only one side of the substrate. The spectra were taken at normal incidence, from 0.2 μm to 2.0 μm. The rARSS processed samples were fabricated using an etch recipe in which the bias power was changed for each sample, as indicated on the plot. 10

FIGURE 8: Simplified schematic of a DC sputtering system, adapted from Ref. [22]. 12

FIGURE 9: Measured spectral transmission enhancement ($T_{rARSS}/T_{unproc}$) in percent, for fused silica samples processed with rARSS on both sides. The four samples depicted by solid lines (A, B, C, D) were etched with slightly different process parameters. The transmission spectra were measured at normal incidence. The enhancement scale is logarithmic. The horizontal dashed line indicates the theoretical maximum transmission enhancement value for double side processed fused silica, and the vertical dashed line indicates the HeNe laser wavelength at 633nm. The perfect single layer AR thin film (PAR) simulation result is shown as the dashed line. 15

FIGURE 10: Measured normalized transmitted power for s (green points) and p (red points) polarized light through both surfaces of the fused silica samples shown in Fig. 9, taken at 633 nm. Dashed lines shown are the theoretical s and p transmission for an unprocessed fused silica slab. Brewster's angle (55.4°) is also indicated by the vertical dashed line. The labels A, B, C, and D correspond to the substrates shown in Fig. 9. The maximum and minimum measurement values are 16

indicated by the vertical limit bars for each AOI.

FIGURE 11: Fictional example of granulometry with circular disks of four different sizes, adapted from Ref. [34]. (a) Is a random image with 4 sizes of circular disks, (b-d) are after consecutively larger disks have been removed and counted on the histogram plot. 17

FIGURE 12: Measured spectral transmission enhancement (τ), in percent, for fused silica substrates with rARSS on the front surface of the tested samples. Six different substrates are shown, a baseline that was processed with metal deposition but no rapid thermal annealing (NTA) and 5 samples processed with varying rapid thermal annealing (RTA) temperatures. The measurements were taken at normal incidence (AOI = 0°), along the incident ray direction. The vertical scale is logarithmic. The black dashed line indicates the maximum possible transmission enhancement for a single side processed sample, which is equal to the maximum value of Fresnel losses per fused silica surface. 26

FIGURE 13: Scanning electron micrographs of the tested samples taken at 20,000x. The top row shows the gold features produced after Au sputtering and RTA. The bottom row shows the features in the fused silica substrate after etching. 27

FIGURE 14: Plots of vertical roughness ($R_z$ in red), and RMS surface roughness ($R_q$ in blue) values vs. RTA processing temperature from the post masking (a) and post etching (b) steps. Dashed lines indicate baseline (NTA) values. 30

FIGURE 15: Granulometry measurements of the void-feature diameter vs RTA temperature, for the Au (a) and FS samples (b) and, the void-coverage density vs RTA temperature for the Au (c) and FS samples (d). For the void diameter values the error bars indicate standard deviation values around the peak population. For void coverage ratio plots error bars indicate maximum and minimum values across multiple images. The dashed lines in all plots indicate the baseline (NTA) values. Granulometry on the 600 °C and 700 °C RTA samples indicated a dual population of small diameter voids and 30

large diameter voids. For these samples both size populations have been plotted on (b), with the red squares indicating the small features and the blue circles indicating the larger features.

FIGURE 16: (a) Asymptotic values of the scattering edge wavelength from Fig. 12, with increasing RTA temperature. The dashed line indicates the baseline (NTA) scattering edge wavelength. (b) Fractional transmission enhancement for each sample at common laser wavelengths (blue diamonds-633 nm, red squares-780 nm, green triangles-1064 nm and purple circles-1550 nm), also from Fig. 12. Negative values indicate on-axis transmission losses greater than Fresnel values, and positive values indicate specular reflectivity suppression. 31

FIGURE 17: (Left) 5x confocal microscope image of spinel surface fabricated utilizing FS rARSS process parameters. (Right) 3D confocal microscope image showing differences in roughness and etch depth for three adjoining grains with different orientations. The deepest etched areas correspond to the smoothest surface and the shallowest etches correspond to the roughest surfaces. 34

FIGURE 18: Transmission spectra of unprocessed spinel (solid black line), and two rARSS processed spinel samples with the “grainy” appearance shown in Fig. 17. Both processed samples show increased scatter in the visible and near IR regions, and their maximum transmission does not exceed the transmission of the unprocessed spinel sample. 34

FIGURE 19: Plot of the modeled refractive index values of PECVD deposited $SiO_2$ thin films on single side polished silicon from 400 nm to 1600 nm. The refractive index was measured using a J. A. Woollam WVASE32 ellipsometer (model 6460LV) and fit to a Cauchy model. 37

FIGURE 20: Plot of etch rates vs time for PECVD deposited $SiO_2$ on silicon for etch processes with 300 W bias power (green triangles) and 400 W bias power (red squares). Etch rates were measured by taping off a small corner of the sample before etching, then removing the tape 38

after etching and using a profilometer to measure the etch step between the etched material and the area masked with tape. The etch step was then divided by the total etch time, resulting in the etch rate.

FIGURE 21: Top down laser confocal microscope images of roughened $SiO_2$ films on silicon. Sample labels A, B, and C correspond with the sample labels found in Table 2. The bottom rectangle shown for each sample is a cross sectional slice (corresponding to the red line in the upper images) showing the relative height of the surface features. 40

FIGURE 22: Refractive index values for sapphire (solid red line), spinel (dotted blue line) and e-beam deposited $Al_2O_3$ (solid green line with error bars). Sapphire and spinel values are from Refs. [55,56], while the deposited $Al_2O_3$ is a measured average of three different e-beam depositions. The error bars indicate the maximum and minimum values measured for the three trials and the measurements were taken of $Al_2O_3$ deposited on single side polished silicon, using a WVASE ellipsometer. 44

FIGURE 23: Deposition schedules for the $Al_2O_3$ and SiO. Roman numerals indicate the deposition run. Percent power values should not be compared between SiO and $Al_2O_3$ as they are being deposited using two different methods (thermal evaporation and electron beam evaporation, respectively) and thus, have different power requirements to achieve similar deposition rates. However, power rates for the same material can be compared between deposition runs to understand how the intermix region was modulated differently each time. It can be assumed that higher power for a specific material also means a higher deposition rate. 46

FIGURE 24: An overview of the four sequential steps used to form the GrIP layer on non-vitreous substrates from Ref. [54]. A) Physical vapor deposition of the optical index matching material on the substrate; B) Physical vapor co-deposition of the optical index matching material and the sacrificial material; C) Ending the physical vapor deposition cycle, with a sacrificial material cap; D) Etching of the sacrificial material using reactive-ion plasma in vacuum. 47

FIGURE 25: A WVASE spectroscopic ellipsometer was used to measure the deposited layers of $Al_2O_3$, the intermix region, and SiO on single side polished silicon substrates for all three deposition methods shown in Fig. 23. 49

FIGURE 26: Transmission results from the three deposition trials on spinel. The black dashed line is unprocessed spinel, and the solid lines are transmission measurements taken after the deposition step was completed, but before any etching occurred. The Roman numerals correspond to the deposition trial numbers found in Figs. 23 and 25. 50

FIGURE 27: Transmission results from the three deposition trials on fused silica. The black dashed line is unprocessed FS, and the solid lines are transmission measurements taken after the deposition step was completed, but before any etching occurred. The Roman numerals correspond to the deposition trial numbers found in Figs. 23 and 25. 51

FIGURE 28: Scanning electron micrographs taken of deposition I and II samples on all three substrates after 15 minutes of etch time. The images are taken at 25,000x, the top row is deposition I and the bottom row is deposition II. Each column shows the results of the deposition and etch on a different substrate (from left to right: silicon, fused silica, and spinel). SEM images were not collected of deposition III. 52

FIGURE 29: Transmission results with increasing etch time for deposition I on spinel. In both plots the black dashed line is unprocessed spinel, and the solid lines are transmission measurements taken after etches of various total etch time, as indicated on the graphs. 54

FIGURE 30: Transmission results with increasing etch time for deposition II on spinel. In both plots the black dashed line is unprocessed spinel, and the solid lines are transmission measurements taken after etches of various total etch time, as indicated on the graphs. 54

FIGURE 31: Transmission results with increasing etch time for deposition III on spinel. In both plots the black dashed line is unprocessed spinel, and the solid lines are 55

transmission measurements taken after etches of various total etch time, as indicated on the graphs.

FIGURE 32: Transmission enhancement (TE) values from the three deposition trials on spinel shown on a logarithmic plot. The black dashed line is the maximum possible transmission enhancement for single side processed spinel, and the solid lines are the best transmission results seen throughout the etching process for each deposition trial. Each line has the deposition trial numeral as well as the etch time indicated on the graph. 55

FIGURE 33: Transmission results from the three deposition trials on fused silica. The black dashed line is unprocessed FS, and the solid lines are the best transmission results seen throughout the etching process for each deposition trial. Each line has the deposition trial numeral as well as the etch time indicated on the graph. Note that because materials with a higher refractive index than the substrate (FS) have been applied, the normalized transmission can never be higher than the unprocessed substrate. 57

FIGURE 34: Transmission results with increasing etch time for deposition III on sapphire. In both plots the black dashed line is unprocessed sapphire, and the solid lines are transmission measurements taken after etches of various total etch time, as indicated on the graphs. 58

FIGURE 35: Transmission results from deposition III on sapphire. The black dashed line is unprocessed sapphire, the purple dotted line is after the deposition step was completed, but before any etching, and the red solid line is the etch run with the highest transmission result (with the etch time indicated on the graph). Only deposition III was attempted with sapphire because sapphire substrates were unavailable during depositions I and II. 58

FIGURE 36: Scanning electron micrographs taken of deposition I and II samples on fused silica and spinel after 60 minutes of etch time. The images are taken at 25,000x, the top row is deposition I and the bottom row is deposition II. Each column shows the results of the deposition and etch on a different substrate (left, fused 60

silica, right, spinel). SEM images were not collected of deposition III.

FIGURE 37: UV laser confocal microscope images of all three MLAs, both before any processing was done (left column) and after rARSS was applied to the curved side of the array (right column). In all images the Z factor was kept constant and unprocessed samples are indicated by a "U" in front of the sample letter and rARSS samples are indicated by an "AR" in front of the sample letter. Color does not correspond to height differences between images. 69

FIGURE 38: Scanning electron micrographs of samples AR-A (top row) and AR-C (bottom row). All samples were taken with the same working distance and accelerating voltage and all were taken at 20,000 times magnification. Images on each sample were taken a minimum of 100 μm apart to investigate the structures at different points on a microlens. Labeled locations are not necessarily the same across MLAs, due to the lack of identifying features. 72

FIGURE 39: Distributed histograms of islands (top row) and voids (bottom row) from the feature sizes corresponding to the SEM micrographs of the random structure AR boundaries shown in Fig. 38. The identifiers (AR-A and AR-C) correspond to the rARSS processed samples from Table 5. The different color bars relate to SEM images taken from different locations on the MLA, and within a sample, one color of islands relates to the same location and same color with the voids. Since there was no way to globally orient the location of the images, the colors between samples do not necessarily correspond to the same locations. The histograms were computed using granulometry. 74

FIGURE 40: Differential population (top row) and differential normalized distribution (bottom row) of the granule sizes measured from the rARSS processed MLAs. The sample labels AR-A and AR-C correspond to the identifiers in Table 5. Positive numbers indicate a plurality of silica islands, where negative numbers indicate more voids (air) than islands. The trend lines are for ease in viewing. 76

FIGURE 41: Example of results from Zemax simulations to optimize the testing distances with the MLA focal point imaging setup. The image on the top is a ray trace through the designed system. The image in the bottom left is a spot diagram of the beam at the detector, and the image in the bottom right is a cross-sectional slice of the beam profile at the detector. 78

FIGURE 42: Diagram showing the optical test setup for investigating the beam profiles of the MLA at focus and through focus. Distance ML was roughly the sum of the MLA focal length and the focal length of $L_1$, and then further optimized in Zemax for proper collimation after $L_1$. The distance LL was determined by physical constraints on the optical system in the lab such as how much throw distance was needed in the lens tubes. Distance LP was roughly the focal length of $L_2$ but further optimized in Zemax. For the distance measurements for each MLA, see Table 6. The dashed box shown indicates the movable assembly that could be translated along the optic axis, in order to investigate the beam profile through focus. 79

FIGURE 43: Beam profiles of focal point spots, comparing rARSS processed MLAs, with unprocessed MLAs, and with simulations of each MLA. The MLA sample identifier is indicated in the top right corner of each plot, and in all cases the red dotted line is the unprocessed MLA, the solid blue line is the 2-side processed rARSS MLA, and the dashed green line is the MLA simulation. 80

FIGURE 44: Plot comparing the distance between the first nulls of the central peak of the focal point spot for all three MLAs. Each MLA is marked and the blue diamonds are the Zemax simulation values, the open red squares are the 2 side rARSS processed MLA values, and the green triangles are the unprocessed MLA values. Error bars shown indicate the uncertainty caused by the resolution of each measurement or simulation, and if error bars are not seen then they are smaller than the marker. 81

FIGURE 45: Top down UV laser confocal microscope image of unprocessed MLA-C showing the arrangement of the lenses in the array. The periodicity measured is 300 μm. 81

FIGURE 46: Beam profiles of unprocessed (left column) and rARSS processed (right column) MLAs from focus through 7 Rayleigh ranges (6 Rayleigh ranges for MLA-C). 84

FIGURE 47: Plot comparing the full width at half maximum (FWHM) of all three MLAs (processed vs unprocessed) at focus, at 0.25 $z_R$, and 0.5 $z_R$. Green triangles are MLA-A, blue diamonds are MLA-B, and yellow circles are MLA-C. In all cases the colored shape represents the 2 side rARSS processed MLA value, while the black outline of the corresponding shape represents the unprocessed MLA value. 84

FIGURE 48: Measured transmission enhancement in percent, for a FS flat substrate and the three rARSS processed MLAs. The red columns were measured after processing only the curved side of the MLAs and only one side of the FS flat substrate. The green column was measured after the second side of all substrates was processed. All measurements were taken with an expanded HeNe laser at 633 nm. The black dashed line is the maximum possible transmission enhancement for double side processed fused silica, 7.2%. 86

FIGURE 49: Diagram showing the optical setup for investigating the far-field diffraction pattern of the MLA where the MLA is placed at the front focal plane of the Fourier transforming lens, L. In this setup, L was placed one focal length away ($f_L$ = 50 mm) from the scanning slit beam profiler, BP. The MLA was then placed one focal length in front of the Fourier transforming lens. 87

FIGURE 50: Normalized intensity plots for all three MLAs when they are placed at the front focal plane of a Fourier transform lens. In all plots the unprocessed MLA profile is shown in red and the 2 sided rARSS processed MLA data is shown in blue. The green curve is the far-field diffraction result of a single microlens. The separation between the diffraction order peaks is 105 µm. 92

FIGURE 51: Normalized intensity plots of the analytical envelopes of the profiles shown in Fig. 50 for each MLA. The unprocessed data is shown in red and the two-side rARSS processed data is shown in blue. The green 51

curve is the analytic result for a single microlens.

FIGURE 52: Normalized intensity plots of the envelopes of the profiles shown in Fig. 50 for each MLA shown on a logarithmic plot to accentuate differences between the unprocessed and 2 side rARSS processed samples on the limits of the envelopes. The unprocessed data is shown in red and the 2-side rARSS processed data is shown in blue. The green curve is the analytic result for a single microlens. 96

# LIST OF ABBREVIATIONS

| | |
|---|---|
| AFM | atomic force microscope |
| $Al_2O_3$ | aluminum oxide |
| AOI | angle of incidence |
| AR | anti-reflection |
| ARSS | anti-reflection surface structures |
| Au | gold |
| $BCl_3$ | borontrichloride |
| $C_4F_8$ | octafluorocyclobutane |
| CCD | charge-coupled device |
| $CHF_3$ | trifluoromethane |
| Cl | chlorine |
| CVD | chemical vapor deposition |
| DC | direct current |
| e-beam | electron-beam |
| F | fluorine |
| FS | fused silica |
| FWHM | full width at half maximum |
| GrIP | Gradient-Optical-Index Porous |
| HeNe | helium neon |
| ICP | inductively coupled plasma |
| Mb | molybdenum |

| | |
|---|---|
| $MgAl_2O_4$ | spinel/magnesium aluminate |
| MLA | microlens array |
| $N_2O$ | nitrous oxide |
| NIR | near-infrared |
| NTA | no thermal annealing |
| $O_2$ | oxygen |
| PAR | perfect anti-reflection thin film |
| PC | polycarbonate |
| PECVD | plasma enhanced chemical vapor deposition |
| PVD | physical vapor deposition |
| rARSS | random anti-reflective surface structures |
| RF | radio frequency |
| RIE | reactive ion etching |
| $R_q$ | root-mean-square roughness |
| RTA | rapid thermal annealing |
| $R_z$ | maximum roughness |
| sccm | standard cubic centimeter per minute |
| SEM | scanning electron microscope |
| $SF_6$ | sulfur hexafluoride |
| $SiH_4$ | silane |
| $SiO_2$ | silicon dioxide |
| Ta | tantalum |
| TE | transmission enhancement |

| | |
|---|---|
| U | unprocessed |
| UNC | the University of North Carolina |
| UV | ultraviolet |
| W | tungsten |
| $z_R$ | Rayleigh range |

# CHAPTER 1: INTRODUCTION

## 1.1 Anti-Reflection Methods

When light is incident on a boundary separating two regions of different refractive index, some portion of the light will be reflected off of the boundary. This reflected light fraction is known as Fresnel reflection and is detrimental in various applications such as flat panel displays, high performance lenses, photovoltaic devices, screens of mobile electronic devices, and super-luminescent diodes. In these applications, it is essential to reduce unwanted reflections in order to increase the performance of optical systems [1]. Anti-reflection (AR) methods can be grouped in two large categories, homogeneous and inhomogeneous, based on the types of surfaces used in suppressing Fresnel reflectivity [2].

Homogeneous surfaces encompass single and multi-layer AR thin films. These thin films have interfaces where abrupt changes in refractive index occur, but they can be engineered such that the reflections off of each interface will destructively interfere with each other, thus nulling their individual contributions. A schematic example of a single layer AR thin film can be seen in Fig. 1. In order for the reflected waves to be eliminated using a perfect single layer thin film, they must be exactly $\pi$ radians out of phase and they must have the same amplitude. For this to occur using a single layer thin film, the index of the film must be equal to $\sqrt{n_s n_0}$ where $n_s$ is the index of refraction of the substrate and $n_0$ is the index of refraction of the superstrate or ambient. The thickness of the film also must be equal to an odd multiple of $\lambda/4$ [2, 3]. Simulations of perfect AR thin films, such as shown in Fig. 2, indicate that while they could completely eliminate reflection at one

specific wavelength, they cannot eliminate reflection over a broad spectral bandwidth, or at large incident angles. Also, in many cases a material with the refractive index required to make a perfect AR coating does not exist in nature. AR thin film specialists design multi-layer thin films when a material with the appropriate refractive index for a single layer thin film is not available. Multi-layer thin films also make AR thin films more practical for use in applications with a wide range of wavelengths or incident angles. While these films may be complicated to design and fabricate, they can be very effective and have been used in the field for many years as they can suppress Fresnel reflections to nearly zero [3, 4].

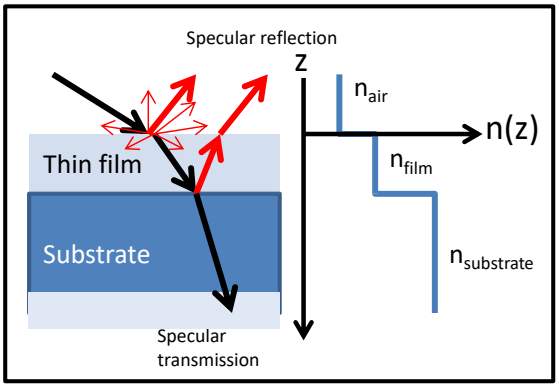


Figure 1: A schematic of a single layer anti-reflective thin film and refractive index profile with propagation distance into the material (z). If the thin film is of the appropriate refractive index (ideally $\sqrt{n_{substrate}}$ for materials in air) and the appropriate thickness (an odd multiple of λ/4) then the light reflecting from the top and bottom surfaces of the film will destructively interfere, reducing or eliminating the specular reflection.

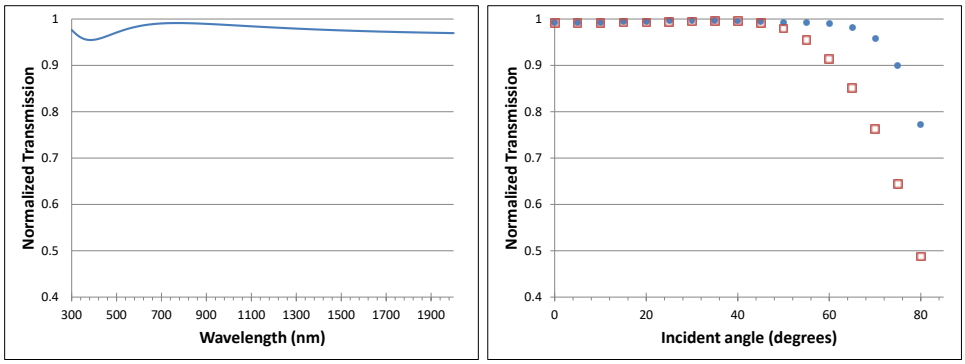


Figure 2: Simulation of transmission from a perfect AR thin film (PAR) applied to both sides of a fused silica (FS) substrate. In this simulation the index of the thin film is equal to the square root of the refractive index of FS and the thickness is 159nm. The plot on the left shows how the transmission changes with wavelength at normal incidence, and the plot on the right shows how the transmission changes with incident angle at 780 nm (the peak transmission wavelength).

Inhomogeneous surfaces rely on gradient index boundary transitions rather than interference to reduce reflection. Because it is the abrupt discontinuity between index values on either side of a boundary that causes Fresnel reflection, gradually varying the index from the superstrate to the substrate value suppresses reflection. Subwavelength anti-reflection surface structures (ARSS) fall into this category, and they can be further classified as periodic or random ARSS.

Periodic ARSS, sometimes also referred to as “Moth Eye” structures or subwavelength gratings, consist of arrays of structures on the surface of the substrate within which the period and feature size is much smaller than the incident light wavelength. Because the feature periodicity is subwavelength, all diffracted light orders higher than zero become evanescent, leaving only the zeroth transmission and reflection orders to propagate [5]. As shown in Fig. 3, by using a shape that allows for a gradual change in refractive index from the superstrate to the substrate (for example, a cone rather than a cylindrical pillar) the reflected light can be suppressed, increasing the zeroth order

transmission efficiency [6, 7]. The design and performance of these periodic ARSS is based on the wavelength, effective feature height, the feature shape, and the period of the array [8]. Because these ARSS are periodic, they will have some wavelength dependence in their AR performance over a large spectral band. To achieve the widest AR bandwidth the ARSS must have very tall features (to make the index transition as gradual as possible) with a very small period (to make the grating subwavelength for as many wavelengths as possible) [2]. This can be difficult to fabricate through conventional lithographic methods.

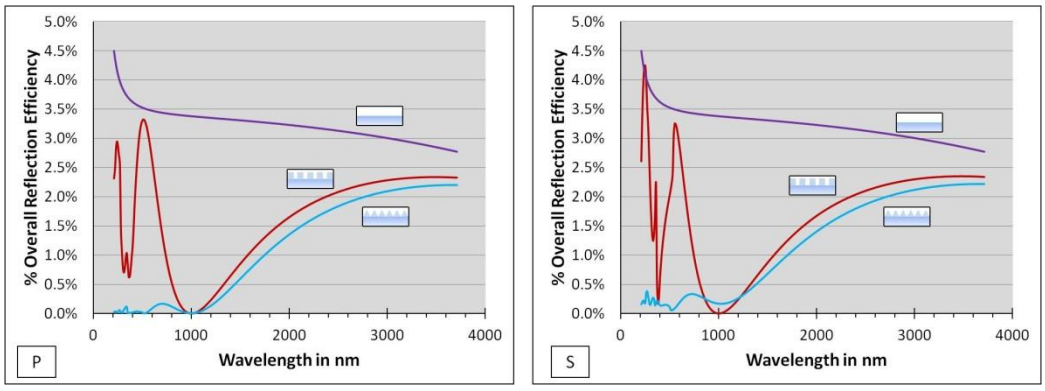


Figure 3: Simulations performed in VirtualLab, using a planar air/fused silica boundary, a periodic rectangular subwavelength grating and a periodic triangular subwavelength grating each optimized for minimum reflectivity at 1000 nm wavelength. The graphs show how the reflection efficiency changes with wavelength from 200 nm to 4000 nm for the p polarization (left) and s polarization (right). The purple lines are the plane air-FS boundary, the red lines are the rectangular grating, and the blue lines are the triangular grating. Graphics included on the plots show schematics of the grating shapes for each configuration.

Random anti-reflection surface structures (rARSS), which are the focus of this dissertation, are randomly spaced, densely packed, sub-wavelength cylindrical features that are fabricated on the surface of a substrate. As light passes from the superstrate to the substrate medium through the rARSS, it propagates through a gradually increasing ratio

of glass to air volume, effectively reducing or eliminating reflection (Fig. 4). Because the rARSS have no periodicity of their spacing, wavelength dependence can be eliminated.

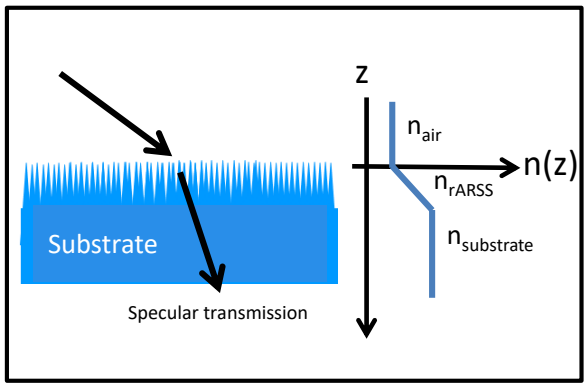


Figure 4: Schematic depicting rARSS on a substrate, and the increasing refractive index with propagation distance into the material *n(z)*. In fabricated rARSS the refractive index profile of the features does not have to be linear as depicted here.

Random ARSS are fabricated differently than periodic ARSS. Periodic ARSS require the application of a masking material such as photoresist, a lithographic fabrication step in which the masking material is patterned, an etch step in which the substrate is removed around the mask, and a resist stripping step where any remaining mask is removed leaving behind the periodic ARSS [9-11]. A diagram of these steps can be found in Fig. 5, adapted from Hobbs and MacLeod [10].

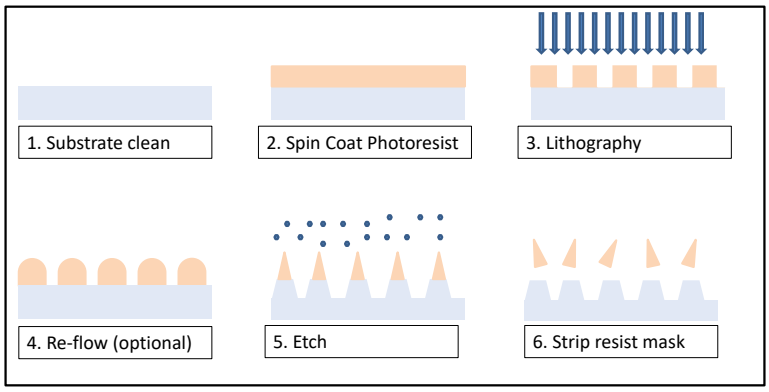


Figure 5: Schematic depicting the common process steps for fabricating periodic surface structures onto a substrate. The diagram is adapted from a figure found in Ref. [10]. It should be noted that step 3 can be interference, conventional, or direct-write lithography.

There are many methods found in the literature today for fabricating rARSS and they can be grouped into two main categories: top down and bottom up fabrication methods [2]. The bottom up fabrication methods involve growing nanowires or porous layers directly onto a substrate's surface [2]. These growth methods can use wet solution processing, where two or more chemical solutions react together [12], or physical or chemical vapor deposition (which are discussed further in section 1.3) [13, 14]. This dissertation focuses on the top-down fabrication category and the three main methods used in this category are depicted in Fig. 6. The first method starts with a metallization masking step, in which a thin discontinuous layer of metal is deposited on the substrate. Another variant of this technique is to deposit a dielectric layer and then overcoat with a metal layer [15]. This metal can either be etched directly, or it can be thermally annealed and then plasma etched. A second method utilizes "active masking" where there is no mask deposited on the surface, but instead a two-cycle plasma etch is used. This 2-cycle plasma etch incorporates an etching step and a passivation step, where a polymer layer is allowed to grow on the substrate surface and effectively create its own mask [16]. The

last method simply involves plasma etching a bare substrate with reactive ion etching (RIE), with or without inductively coupled plasma (ICP) etching processes. While these methods may vary in complexity, they typically are faster than traditional lithography. This dissertation will explore several fabrication methods for rARSS that fall into the top-down fabrication category.

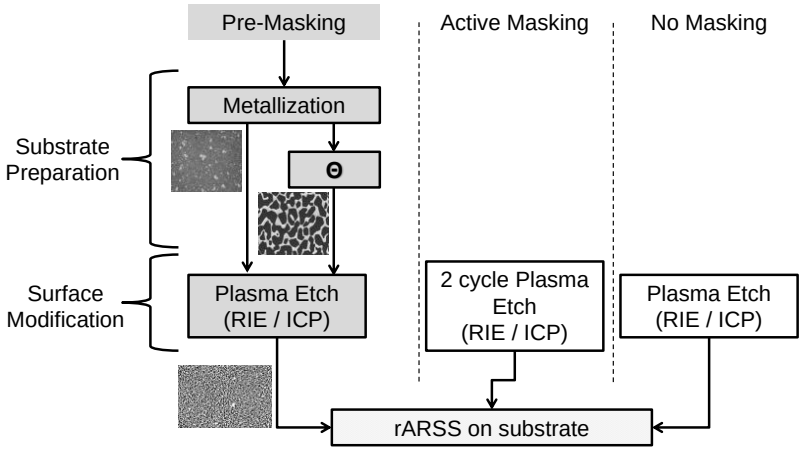


Figure 6: Flow chart depicting the steps involved in the three methods of top-down fabrication of rARSS found in the literature. The pre-masking method is evaluated in this dissertation in Chapter 2. Representative SEM images that depict samples at the metallization, rapid thermal annealing (RTA *Θ*), and final rARSS substrate steps in the fabrication process are included in the illustration [17].

## 1.2 Introduction to Reactive Ion Etching (RIE)

Dry plasma etching is a method that is commonly used in conjunction with a masking step to structure unmasked areas of a substrate. Reactive Ion Etching (RIE) is a type of plasma etching that requires a chamber with two electrodes powered by a radio frequency (RF) power supply. The substrate that is going to be etched sits on the bottom electrode (the cathode), the chamber is evacuated, and a small amount of a reactive gas is pumped into the chamber. The gas, or mixture of gases used, must be chosen carefully

because they react with the specific substrate chosen. For substrates containing silicon, typically fluorine or chlorine based gases are used, such as sulfur hexafluoride ($SF_6$), octafluorocyclobutane ($C_4F_8$), trifluoromethane ($CHF_3$), or boron trichloride ($BCl_3$), and oxygen ($O_2$) is frequently mixed in as well. When the RF power supply is turned on, the plasma is ignited, ripping electrons off of the gas molecules and sending them colliding with other molecules in the gas, breaking them apart. This leads to a mixture of neutral molecules (called radicals- usually Chlorine (Cl) or Fluorine (F)), positive ions, and electrons. All of these chemical species will interact with the walls of the chamber and the surface of the sample, and the voltage difference from the electrodes will result in an electric field perpendicular to the sample surface [18, 19]. Above the surface of the sample the elements in the gas molecules that do not interact with the substrate will remain in the plasma and eventually be removed from the chamber by the constant outgoing gas flow. Some of the neutral radicals will diffuse through the plasma and onto the surface of the sample where they can adsorb to the surface and do one of two things: a) they can simply sit on the surface of the substrate and block the etching process, or b) they can spontaneously react with the material. When this happens the product is volatile and desorbs from the surface, and is eventually removed with the other gas from the chamber [18, 19].

The voltage difference between the surface of the sample and the plasma serves to accelerate positive ions towards the sample, giving the RIE process a perpendicular directionality that wet chemical etching processes do not have. The positive ions will bombard the surface and can either sputter the surface of the substrate through the transfer of their momentum, or they can provide the energy needed to allow a neutral

radical on the surface to react with the substrate and volatilize. When the ions promote the reaction between the radicals and the substrate it is called ion-induced etching. This process is faster than the spontaneous reactions, and doesn't result in the substrate being redeposited on the surface which can happen with sputtering conditions [18, 19].

There are many variables that can be adjusted to achieve the specific etch results desired, such as chamber pressure, bias power, gas composition and flow rate, temperature of the substrate, and the length of time of the etching process. Of course, many of these variables can have both positive and negative effects that must be balanced, which results in a significant amount of time spent on process development [18-21].

Members of the Optical Micro-Structured Interfaces Laboratory at the University of North Carolina at Charlotte have investigated and mapped changes of the RIE variables and how they affect the final transmission spectra of planar fused silica substrates. For example, Fig. 7 shows that as the bias power in the etch process is increased, the peak transmission wavelength of the sample shifts towards the infrared. This information can be very helpful when developing an etch process to target peak transmission at a specific wavelength. Of course, different etching tools and different substrate materials will all etch differently, so while plots like these can serve as a starting point for developing new etch recipes, there is still a significant amount of process optimization that must occur when trying a new etch process.

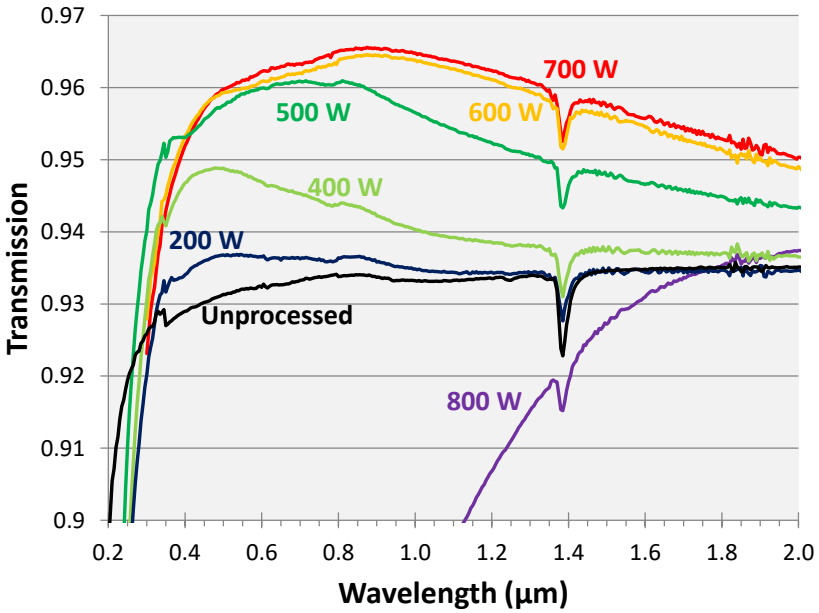


Figure 7: Measured spectral transmission data for an unprocessed fused silica substrate (black line) and fused silica samples processed with rARSS on only one side of the substrate. The spectra were taken at normal incidence, from 0.2 µm to 2.0 µm. The rARSS processed samples were fabricated using an etch recipe in which the bias power was changed for each sample, as indicated on the plot.

## 1.3 Physical and Chemical Deposition Methods

As many methods for fabricating rARSS that are found in the literature and discussed in this dissertation require the deposition of a secondary material onto the substrate, a short discussion of various deposition methods is presented here. The rARSS fabrication methods used in this document incorporated both physical vapor deposition (PVD) and chemical vapor deposition (CVD). Within those broad categories, several methods were used.

Physical vapor deposition is a category that encompasses any methods that use solid or molten sources, use a physical mechanism to turn the source material into a gaseous state, and in general do not utilize chemical reactions to adhere the materials on a

surface [22]. Throughout this document, three PVD methods are used: resistance heating, electron beam evaporation, and sputtering. Resistance heating, also sometimes called thermal evaporation, utilizes a thin piece of metal (typically tungsten (W), tantalum (Ta), or molybdenum (Mb)) that has been shaped into a "boat" or box, into which the material to be evaporated is placed. The boat is attached to a low-voltage, high-current power supply which heats up both the boat and the evaporant inside it. These systems are relatively simple equipment wise, but they are limited by low input power levels, and they are not effective at evaporating materials with high minimum evaporation temperatures [22-24].

Electron-beam evaporation overcomes the difficulties resistance heating has with evaporating materials with high minimum evaporation temperatures, and can be used to evaporate almost all materials. With this method, the material to be deposited is placed in a small crucible at the bottom of the chamber. A heated filament emits electrons that are accelerated and focused towards the evaporant material, and the energy in the electron beam causes the material to melt and evaporate, or sublimate. The deposition rate can be controlled not only by the power of the electron beam, but also by making the focal spot larger or smaller, or by scanning the beam across the evaporant crucible [22, 23].

The final PVD method utilized in this dissertation was sputtering. To use the sputtering method of material deposition, the material to be deposited must be made into a plate. This plate is connected to the negative terminal of the power supply (DC supply for depositing metals, or RF supply for depositing insulators) and a non-reactive gas such as argon is pumped into a pre-evacuated chamber (Fig. 8). When the power to the system is turned on, a plasma discharge is formed. Positive ions from the plasma will strike the

target and neutral atoms of deposition material will be removed from the target due to the transfer of momentum. These neutral atoms will eventually deposit onto the substrate located on the positive terminal of the power supply [22, 24].

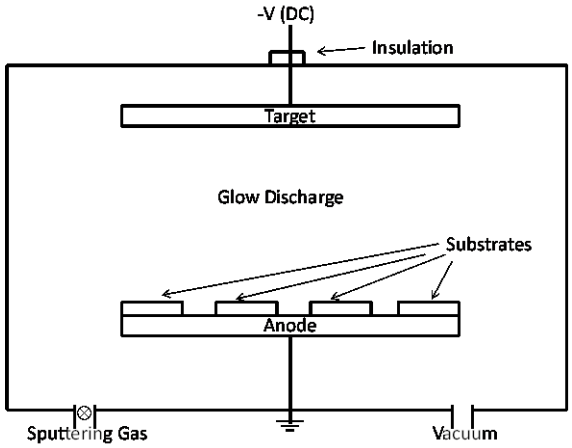


Figure 8: Simplified schematic of a DC sputtering system, adapted from Ref. [22].

Chemical vapor deposition (CVD) is a category that also encompasses many deposition methods, but they all involve two or more chemically reacting gasses to produce a solid that will deposit onto a substrate. The method used in this dissertation, plasma enhanced chemical vapor deposition (PECVD) has the chemical reaction enhanced by the presence of an RF powered plasma discharge. This discharge allows for the chemical reactions to occur at lower temperatures than in a conventional CVD system and also gives the user some control over the stresses on the films, resulting in the ability to deposit thicker films [22].

## 1.4 Testing rARSS Performance and Properties

One of the most important details when developing a process for fabricating rARSS, or when deciding whether or not to use rARSS in a specific application, is having

a complete understanding of how the rARSS perform. Random ARSS performance encompasses many variables, such as how the rARSS perform over various wavelengths, or at various angles of incidence and polarizations. When two different sets of rARSS perform differently in these tests, then it is critical to determine what is physically different between the two sets of rARSS that causes their performance differences. If rARSS is to be applied to optics with focusing capabilities rather than just optical windows, it is important to find out what the rARSS does to the profile of the beam as it passes through the optic. Since there are many different testing methods in the literature [25-29] there are no universal testing methods. This dissertation will examine data collected from many different performance tests, as well as surface metrology investigations, in an effort to characterize as completely as possible the rARSS fabricated.

The most common test used in the literature is a transmission measurement taken at normal incidence, and over a wide range of wavelengths. These tests are important because they confirm the most basic argument about rARSS- that the structures are reducing light reflection over spectral bands. Transmission measurements are the most effective way to prove this concept, as an increase in measured specular transmission must in turn mean a decrease in reflection. Reflection measurements alone are not conclusive, as a reduction in reflection can be the result of an increase in transmission, or perhaps simply an increase in scattered light, which would not be beneficial in most applications. In this dissertation, specular transmission spectra of rARSS fabricated on planar samples were collected on a Cary 5000 (Varian) ultraviolet-visible-near-infrared dual-beam grating spectrophotometer at normal incidence, in a wavelength band from 300 nm to 2,000 nm. In all cases, measurements were also taken with unprocessed

substrates, in order to have a control reference, and the processed samples were compared to the control in order to calculate the transmission enhancement produced by the rARSS. Transmission enhancement will be discussed in section 2.2.2.

Published work by the Optical Micro-Structured Interfaces Laboratory members have shown that samples processed under different conditions may have similar transmission spectra at normal incidence. To better understand how these different processing parameters can affect the performance of rARSS, transmission measurements were taken at 633 nm from $0^{\circ}$ to $75^{\circ}$ angle of incidence for both p and s polarized light. These measurements, shown in Figs. 9 & 10, were some of the first published to show that samples that may perform similarly at normal incidence, can have very different responses to polarized light at off normal angles of incidence [26, 30]. These results are discussed in the references and are mentioned here for completeness.

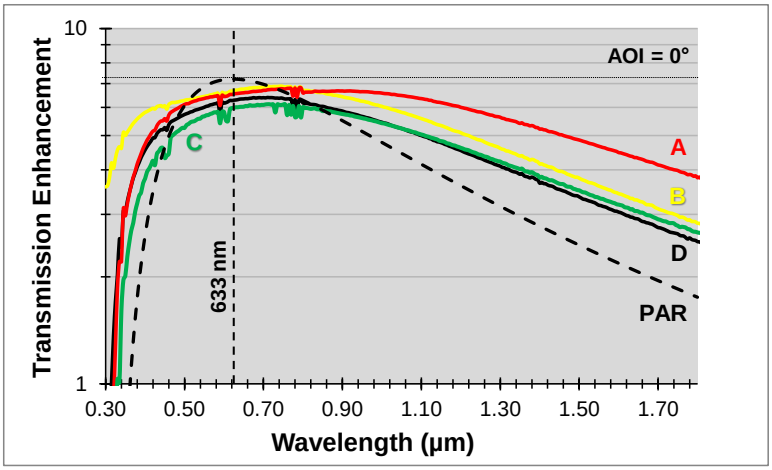


Figure 9: Measured spectral transmission enhancement ($T_{rARSS}/T_{unproc}$) in percent, for fused silica samples processed with rARSS on both sides. The four samples depicted by solid lines (A, B, C, D) were etched with slightly different process parameters. The transmission spectra were measured at normal incidence. The enhancement scale is logarithmic. The horizontal dashed line indicates the theoretical maximum transmission enhancement value for double side processed fused silica, and the vertical dashed line indicates the HeNe laser wavelength at 633nm. The perfect single layer AR thin film (PAR) simulation result is shown as the dashed line.

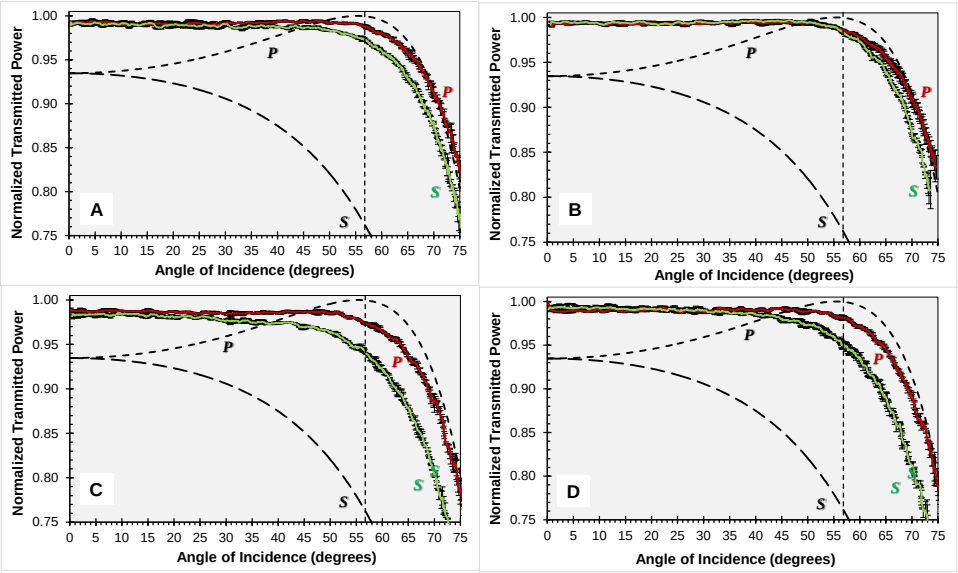


Figure 10: Measured normalized transmitted power for s (green points) and p (red points) polarized light through both surfaces of the fused silica samples shown in Fig. 9, taken at 633 nm. Dashed lines shown are the theoretical s and p transmission for an unprocessed fused silica slab. Brewster's angle (55.4°) is also indicated by the vertical dashed line. The labels A, B, C, and D correspond to the substrates shown in Fig. 9. The maximum and minimum measurement values are indicated by the vertical limit bars for each AOI.

In order for rARSS to become an established method for reducing reflection on optical components, it must be shown that the profile of the beam does not change as it passes through a lens or other components that have been processed with rARSS on one or multiple surfaces. Published work by Courtney Taylor [31, 32] and her dissertation [33] present a study of rARSS on 1" diameter lenses. In the present dissertation, a scanning slit beam profiler has been used to investigate how the beam profile of a microlens array (MLA) changes at focus and through focus, when the MLA has rARSS applied to the front and back surfaces.

Finally, it is important to understand how the transmission properties of surfaces with different rARSS relate to the size distribution of the physical features themselves. To study this, scanning electron microscope images of the processed substrate surfaces are

taken. Granulometry is then used on each image, which looks for either island or void clusters of pixels. It starts this search with one pixel, and then gradually grows the number of pixels it's searching for in an octagonal shape. This program allows for the creation of a histogram showing the size distribution of the islands and voids on a surface (Fig. 11) [34]. By taking multiple images across the sample, performing the granulometry routine and then averaging the results, a reasonable picture of the feature sizes and distributions can be obtained.

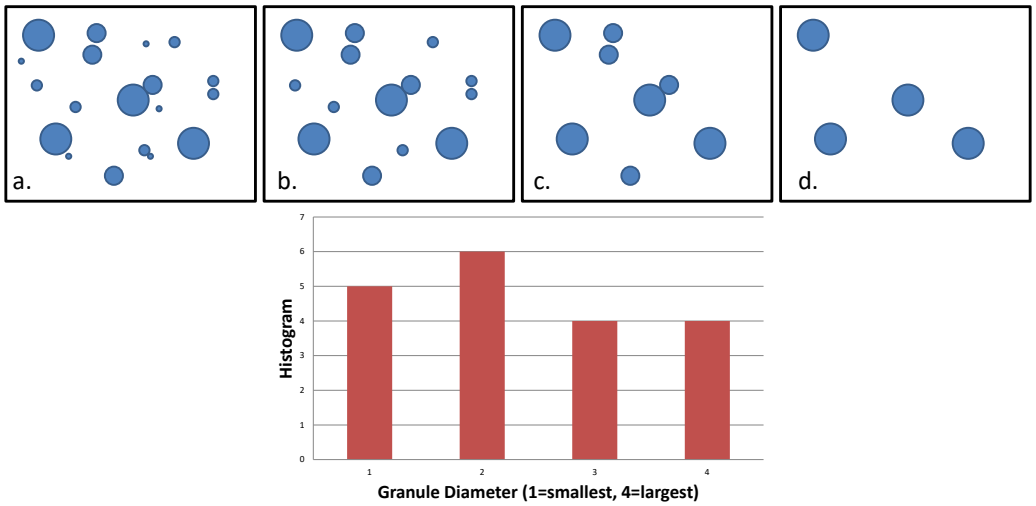


Figure 11: Fictional example of granulometry with circular disks of four different sizes, adapted from Ref. [34]. (a) Is a random image with 4 sizes of circular disks, (b-d) are after consecutively larger disks have been removed and counted on the histogram plot.

## 1.5 Introduction to Microlens Arrays (MLAs)

There is an abundance of studies in the literature of rARSS applied to planar substrates, and Dr. Taylor's previously cited work was an investigation of how rARSS on curved substrates would perform. The curved substrates she studied however, were 1" in diameter and the curvature of the lenses did not change on the micro-scale drastically with radial distance from the center of the optic. The next logical step is to investigate

how rARSS processed onto small and relatively steep lenses, such as on micro-lens arrays (MLAs), would perform.

MLAs on fused silica are typically fabricated by applying photoresist to the substrate surface and using lithography to create a cylinder array mask. Then the wafer is heated, causing the cylinders to melt into hemispheres, and with an appropriate RIE step these photoresist hemispheres are transferred to the fused silica substrate resulting in nearly spherical microlenses [35, 36]. It has also become popular to fabricate MLAs out of polymer materials because there are many ways they can be fabricated such as ink-jet printing [37], photoembossing [38], and thermo-extrusion [39]. Microlens arrays are typically used in two different ways. The first is in applications that require a beam of light to be focused into an array of small spots, such as for coupling light into fiber optic arrays or in CCD camera arrays [38]. The second use is for applications that require a beam with a Gaussian intensity profile to be homogenized into a beam with a flat top intensity profile such as backlighting for LCD displays [39], photolithography [40], or microscopy [41]. All of these applications could benefit from reduced Fresnel reflection, and while applying periodic ARSS to MLAs has been reported in the literature [39, 42], previous work with rARSS on MLAs has been limited.

In a paper by Pacholski et al. [43], random anti-reflecting surface structures (rARSS) were applied to MLAs using various fabrication methods, and SEM images were used to investigate how the structures were different at the top of a microlens, versus on the slope of a microlens, and at the bottom of a microlens. Transmission spectra were also collected and it was shown that all fabrication methods had higher transmission than an unprocessed MLA. However, for rARSS to be a viable option for reducing

reflection on MLAs, it must be shown that the random structures do not negatively affect either the MLAs beam propagation and focusing abilities or its wavefront properties. These tests have not yet been seen in the literature and are presented as a part of this body of work.

## 1.6 Dissertation Overview

This dissertation broadly focuses on random anti-reflecting surface structures (rARSS). Chapter 2 presents the fabrication of these rARSS, how the fabrication affects the physical characteristics of the rARSS, and in turn how that will affect the transmission properties through the structures. This chapter is divided between three topics, starting with an investigation of rARSS fabricated on planar fused silica (FS). The FS rARSS are fabricated by depositing a thin layer of gold onto the FS substrate, then rapid thermal annealing the substrate for one (1.0) minute at various temperatures before etching the samples with an RIE process. Scanning electron microscope images of the samples before and after the RIE step were taken so that the physical characteristics of the gold mask could be compared to the physical characteristics of the FS rARSS. In addition, collecting transmission spectra post etching enables the relation of physical variables throughout the fabrication process and the transmission enhancement properties of the various samples.

The second and third topics of Chapter 2 explore the question of rARSS fabrication on non-vitreous materials. First, it is shown that methods for producing rARSS on FS are not applicable to non-vitreous materials, and a method for circumventing this limitation is proposed, where a layer of silicon dioxide ($SiO_2$) is

deposited onto a non-vitreous substrate, and the $SiO_2$ is etched using the same methods as typical FS substrates. Initial tests of this method are presented as proof of the concept that it is possible to roughen a thin film applied to a substrate. Next, the thin film deposition/etch process is further developed and tested, resulting in Gradient-Optical-Index Porous (GrIP) coatings. The general goal was to approximate index matching coatings, by layering a material with an effective refractive index which closely matches the substrate material's refractive index at the target wavelength range, and a sacrificial material easily removable through RIE. These materials are co-deposited onto the substrate, and then the sacrificial material is removed through RIE, leaving a rough or porous layer of the index matching material behind. This GrIP coating should in principle act as a rARSS on a non-vitreous substrate. This process has not been reported to-date, and several test trials are presented in this dissertation, utilizing various deposition recipes. It is shown that it is possible to increase the transmission for spinel and sapphire substrates and the indications are that this transmission increase is caused by effective medium effects from the intermix layer rather than rARSS effects.

Chapter 3 presents testing of optics with rARSS applied to their surfaces, specifically microlens arrays (MLAs). MLAs with three different effective focal lengths, and identical lens diameters and periodicity were purchased from Edmund Optics. For each focal length available two MLAs were tested: one processed with rARSS on both sides of the array and one unprocessed on both sides. For all of the experiments both MLAs were tested in order to filter out any natural aberrations coming from the test system or MLA itself. Power measurements at a wavelength of 633 nm (HeNe laser) were collected of the processed and unprocessed MLAs, to verify the transmission

increase with application of the rARSS to both sides of the substrates. It was found to be at the level of transmission enhancement measurements on planar fused silica substrates. A set of experiments was developed to determine the optical effects from the application of the rARSS to the MLA, and possible deviations in the focusing abilities of the microlenses. A telescope system was built to image the focal point of the MLA to a beam profiler, and beam profile measurements were taken at focus and at increasing Rayleigh range ($z_R$) distances. Simulations of the test system were also performed in Zemax and by comparing the simulated, the processed and the unprocessed MLAs it was shown that the rARSS do not impact the focusing performance of MLAs.

While the beam profile measurements were helpful for determining if a rARSS processed MLA could still focus light to the same size spot as an unprocessed MLA, it was important to develop a test that could determine if and how the phase of a processed MLA differed from an unprocessed MLA. To study this, the MLAs, a positive external lens, and a beam profiler were used, to measure the Fourier transform profile of the MLA at the focal plane of the positive lens. Since the far-field diffraction is sensitive to changes in phase, these tests highlight any phase differences between the unprocessed and processed MLAs. The data presented in Chapter 3 will show that while adding rARSS to the surfaces of a MLA does not affect the focusing abilities of the lenses, changes to the phase of the wavefront passing through the lenses are measurable.

Chapter 4 of this dissertation contains the final conclusions drawn from the work presented in Chapters 2 and 3. It also discusses some potential future work that could be explored to expand on the work presented here.

# CHAPTER 2: FABRICATION TECHNIQUES AND TESTING

## 2.1 Introduction

In this chapter, methods of fabricating rARSS onto vitreous and non-vitreous substrates are studied. In section 2.2, rARSS were fabricated on fused silica substrates using gold masking and rapid thermal annealing (RTA). Data is presented relating the physical characteristics of the gold mask statistical populations, and the resulting rARSS population, as well as spectral transmission properties of the final surfaces. This section focuses on comparing results between samples processed at different RTA temperatures, as well as samples fabricated without undergoing RTA, to relate fabrication process statistics to transmission enhancement values.

In section 2.3, recipes for producing rARSS on fused silica substrates were tested on spinel substrates. Spinel is a polycrystalline material, and the results of these tests show that recipes for vitreous materials like fused silica are not transferrable to non-vitreous materials. In order to try to circumvent this issue, the idea of applying a thin film of $SiO_2$ to a spinel substrate and then fabricating rARSS into the thin film was proposed, and section 2.3.3 will show preliminary results from these tests.

Section 2.4 discusses a new method for fabricating rARSS onto non-vitreous materials. In this method, called Gradient-Optical-Index Porous (GrIP) coatings, an index matching material and a sacrificial material are co-deposited onto a substrate and the sacrificial material is etched away, leaving a porous index matching layer with AR properties. Three different deposition methods are tried, and the etching is conducted in short increments so that the transmission of the GrIP coating and substrate can be tested

as the optical surface evolves through the process. Transmission spectra, confocal microscope images, and scanning electron microscope images are all presented in an effort to understand this new process.

Section 2.5 summarizes the fabrication efforts, relates them, and draws some final conclusions.

## 2.2 Spectral Transmission Enhancement Properties of Random Anti-Reflecting Surface Structures Fabricated on Vitreous Substrates

### 2.2.1 Introduction

As was discussed in Chapter 1, there are many ways rARSS can be fabricated onto fused silica. In this section, the method which starts with a metallization masking step has been used, and the metal layer was subjected to a RTA step before plasma etching. This method was selected because it allows for multiple control variables that change the transmission performance of the finished rARSS, and it allows for the measurement of a random feature distribution (the annealed metal) to correlate with the final random etched structure (the fused silica).

Results are presented to relate the dimensional features of the rARSS (diameter and height statistical distributions), before and after etching, to the optical properties of the rARSS, such as, the short wavelength off-axis scattering edge and spectral specular transmission. One side of six (6) fused silica substrates was processed with varying RTA temperatures, and then all substrates were etched together. Data was collected with the various methods listed in Table 1 below, and correlations between RTA temperature, the

final rARSS physical feature sizes, and the final rARSS on-axis transmission performance are identified.

Each measurement provides a certain surface characterization result or an optical performance result. The initial metallization of the substrates is evaluated using variable-angle spectroscopic ellipsometry (Woollam WVASE model 6460LV), in order to obtain an effective layer thickness of the gold (Au) layer deposited, and assure the consistency from sample to sample. Top-down scanning electron microscope (SEM) images were collected on a Raith 150, and granulometry was performed to obtain information about the feature diameters and densities across the sample. Broadband transmission spectra were measured from 300 nm to 2000 nm with a Cary-5000 spectrophotometer at normal incidence.

Table 1: Measurement methodology for each fused silica sample tested, after each of the three main process steps.

| **Metallization** | **Rapid Thermal Annealing (Θ)** | **Plasma Etch (RIE/ICP)** |
|---|---|---|
| *Ellipsometry* | | |
| *Scanning Electron Microscope (SEM)* | | |
| | *Granulometry* | |
| | *Scattering* | |
| | | *Transmission* |

### 2.2.2 Fabrication, Transmission Enhancement, and Surface Characterization

A thin discontinuous layer of Au (less than 20nm) was deposited on all of the substrates at once, using an AJA sputter deposition system (ATC 1800-F). Very thin sputtered Au films tend to be non-uniform and in many cases discontinuous [44, 45]. For this application the randomness of the Au film is used to "seed" the random etch process

as a partial "perforated" mask. The coating thickness listed above is more of an estimated average across the substrate surface. The NTA sample was coated with gold and not annealed, while another 5 samples were annealed at gradually increasing temperatures for the same 1 minute time interval. After the annealing step, all 6 samples were processed with RIE under previously optimized processing parameters. All samples were only processed with rARSS on one side of the substrate.

Figure 12 shows the measured specular spectral transmission enhancement ($\tau$) of the six single-side processed rARSS FS substrates. Spectral transmission measurements from 300 nm to 2000 nm at normal incidence were made through the center of the processed samples and an unprocessed fused silica substrate, using a Cary 5000 (Varian) ultraviolet-visible-near-infrared dual-beam grating spectrophotometer. The normal incidence ($\theta$ = 0°) transmittance of the rARSS samples $T_{ARSS}$ was normalized to the respective measured transmittance of plain polished FS substrates $T_{FS}$, and the spectral transmission enhancement was calculated using the relation:

$$\tau(\lambda, \theta = 0) = \tau_o(\lambda) = \left(\frac{T_{ARSS}(\lambda,0)}{T_{FS}(\lambda,0)} - 1\right) \quad (1)$$

The dimensionless quantity $\tau(\lambda,\theta)$ is the fractional increase in transmittance above the unprocessed FS values for values of $\tau>0$, and a decrease in transmittance for $\tau<0$. For FS optical components, since the Fresnel losses per interface are an average of -3.7% of the incident intensity in the spectral region of interest, the total maximum transmission enhancement is an average of +7.2% accounting for both substrate surfaces. In this case, the transmission enhancement plots are shown on a logarithmic (base 10) scale and only display values of positive $\tau$ [32]. The measurements show a red-shifting trend for the

short-wavelength scattering edge with increasing RTA temperature, as well as decreasing transmission enhancement values in the NIR wavelength region (750 nm – 1950 nm).

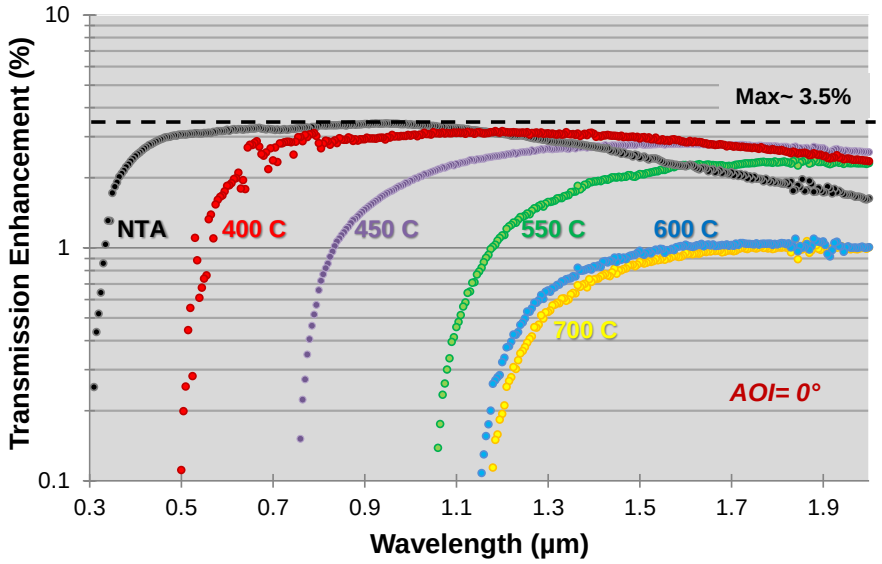


Figure 12: Measured spectral transmission enhancement ($\tau$), in percent, for fused silica substrates with rARSS on the front surface of the tested samples. Six different substrates are shown, a baseline that was processed with metal deposition but no rapid thermal annealing (NTA) and 5 samples processed with varying rapid thermal annealing (RTA) temperatures. The measurements were taken at normal incidence (AOI = 0°), along the incident ray direction. The vertical scale is logarithmic. The black dashed line indicates the maximum possible transmission enhancement for a single side processed sample, which is equal to the maximum value of Fresnel losses per fused silica surface.

To understand how the effective medium thickness is evolving with the changing RTA temperature for these samples, depth and roughness measurements of the surfaces are used. Measuring the lateral feature size distributions can show what kind of statistical size distributions are found across the processed sample. Together, these measurements can start to quantify the effective index density of the fabricated surfaces.

Figure 13 shows high-resolution (1024 x 768 pixel) top-down, surface gray-scale images of the center of the samples, obtained at 20,000 times magnification, with a constant working distance and accelerating voltage for all images. The top row shows each sample after the metallization and RTA steps (Au samples), and the bottom row shows each sample after an identical RIE process (FS samples). It is qualitatively observed that the Au samples have "voids" (dark holes in the Au film) in the baseline, 400 °C, 450 °C, and 550 °C samples, which are gradually increasing in size with increasing annealing temperature. With the 600 °C and 700 °C samples the voids become so large that the dominant features are gold islands left behind. Looking at the fused silica samples after etching, a similar trend can be seen, with the etched voids increasing and becoming large craters.

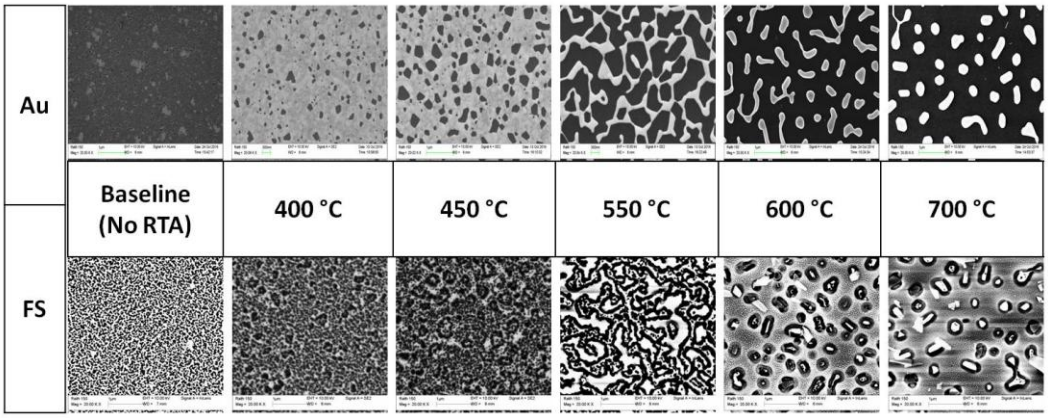


Figure 13: Scanning electron micrographs of the tested samples taken at 20,000x. The top row shows the gold features produced after Au sputtering and RTA. The bottom row shows the features in the fused silica substrate after etching.

To measure the depth of the surface features after RTA and after etching, an Olympus LEXT UV-confocal microscope was used. The confocal measurement yields

the vertical distance (depth) between the highest peak and the lowest valley ($R_z$), and the RMS roughness of the surface height ($R_q$) for each sample [46]. Figure 14 shows the $R_z$ and $R_q$ values measured with relation to each other, as a function of the RTA temperature at which the sample was processed, both after the RTA step and after the RIE step. The expectation from this comparison is to relate a surface with large mask features (i.e. the 600 °C or 700 °C Au samples) before and after etching. The $R_z$ and $R_q$ values show that the highest RTA temperatures are actually the shallowest of the etched samples. This is supporting the measured decrease in transmission enhancement with increasing RTA temperature shown in Fig. 12, because a shallow etch means a thin effective medium layer, which would not effectively reduce reflection for long wavelengths.

To determine the lateral dimensions (average diameters) of the mask and etched features, a granulometry routine was employed (discussed in section 1.4). The granules used for classification were octagons, varying from 2 to 158 pixels in diagonal, and scaled to the dimensional bar for each SEM image. Multiple areas of each sample were imaged, and the results were averaged. At the sample surfaces (Fig. 13) both islands and voids were identified, and the diameter of the voids was measured for all samples. A histogram of feature sizes (voids) was collected from the sample SEM images, resulting in the peak feature size (highest incidence of average diameter) and the standard deviation of the population's distribution. These values along with the surface density values (surface coverage ratio) are shown in Fig. 15. The qualitative observation that the void size and density was increasing with increasing RTA temperature for the Au samples is confirmed.

For the fused silica samples shown in Fig. 15 (b) and (d) the trend is not simply a linear increase in size and density as it is for the Au masked (pre-etched) samples. Figure 15 (b) shows an increase in void size for the lower RTA temperatures, and then a leveling off in size for the large features on the highest temperature samples. Since the feature diameters correlate to the scattering properties of the sample, it is not surprising to see a similar trend in Figure 16 (a) where the scattering edge wavelength increases linearly with the lower RTA temperatures and then levels off for the highest temperatures. Clearly increasing the RTA temperature increases the final feature sizes and thus, further red-shifts the short wavelength scattering edge, however it is interesting that this linear trend does not seem to continue indefinitely. The leveling of the void density measurements in Fig. 15 (c) are an indication of the actual masking island population becoming sparser, with Au islands isolated and further apart from each other, in a "sea" of bare substrate surface, indicated by the 80% void surface coverage. In contrast, Fig. 15 (d) shows the distribution of voids remains around 50% for all of the RTA temperatures in the final etched silica surface. Even on the high temperature samples which had both small and large void structural features the overall surface coverage remains at approximately 50%. This observation is verified by the SEM images shown in Fig. 13.

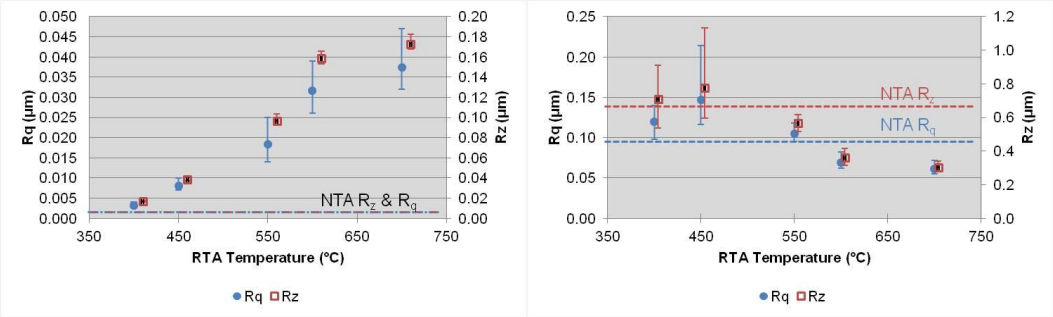


Figure 14: Plots of vertical roughness ($R_z$ in red), and RMS surface roughness ($R_q$ in blue) values vs. RTA processing temperature from the post masking (a) and post etching (b) steps. Dashed lines indicate baseline (NTA) values.

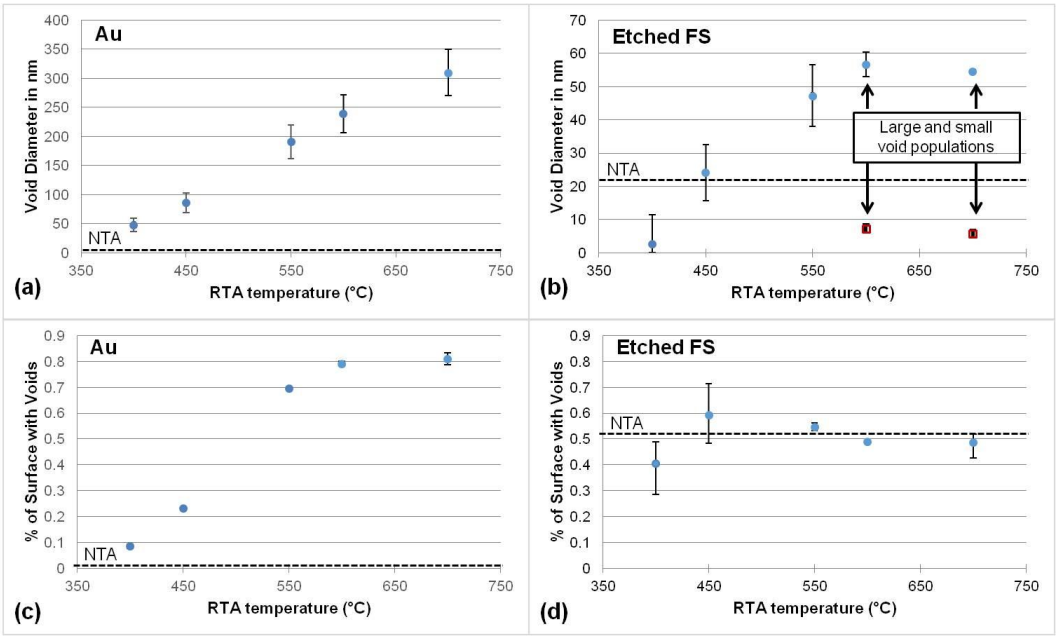


Figure 15: Granulometry measurements of the void-feature diameter vs RTA temperature, for the Au (a) and FS samples (b) and, the void-coverage density vs RTA temperature for the Au (c) and FS samples (d). For the void diameter values the error bars indicate standard deviation values around the peak population. For void coverage ratio plots error bars indicate maximum and minimum values across multiple images. The dashed lines in all plots indicate the baseline (NTA) values. Granulometry on the 600 °C and 700 °C RTA samples indicated a dual population of small diameter voids and large diameter voids. For these samples both size populations have been plotted on (b), with the red squares indicating the small features and the blue circles indicating the larger features.

Looking at Fig. 16 (b) a general trend of transmission enhancement ($\tau$) decreasing with increasing RTA temperature is observed. To explain this, we refer back to Fig. 14 (b) where it was shown that as the RTA temperature increased, the $R_q$ and $R_z$ values across the surface increased slightly, and then dropped for the higher temperature samples. Because the thickness of the effective medium layer should be on the order of or larger than the wavelength being used, one can conclude that as the surface feature depth decreases, the transmission enhancement for the longer wavelengths decreases. If this decrease in thickness was the only change to the surface we would expect to see the peak transmission enhancement wavelength shift to the UV, but the scattering from the large feature diameters on the high temperature samples is impacting this shift. The red shifting of the scattering edge from increasing feature size and the blue shifting of the peak transmission enhancement wavelength from the decreasing effective thickness of the samples with increasing RTA are working against each other.

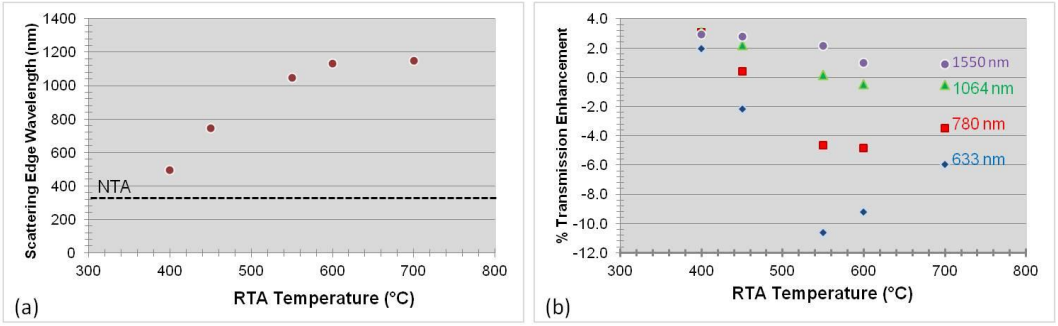


Figure 16: (a) Asymptotic values of the scattering edge wavelength from Fig. 12, with increasing RTA temperature. The dashed line indicates the baseline (NTA) scattering edge wavelength. (b) Fractional transmission enhancement for each sample at common laser wavelengths (blue diamonds-633 nm, red squares-780 nm, green triangles-1064 nm and purple circles-1550 nm), also from Fig. 12. Negative values indicate on-axis transmission losses greater than Fresnel values, and positive values indicate specular reflectivity suppression.

### 2.2.3 Summary

Random anti-reflection structured surfaces were fabricated on fused silica substrates using a three step process: gold layer deposition, rapid thermal annealing (RTA) forming a mask of random islands, and reactive ion etching (RIE). Increasing RTA temperatures led to increasing Au mask feature diameters and isolation of sparse masking islands. Once the samples were etched fused silica feature sizes showed a trend of increasing and then leveling off with increasing temperature, which matched the shifting scattering edge wavelength. Increasing RTA temperature also led to an eventual decrease in the effective layer thickness leading to a decrease in the transmission enhancement for longer wavelengths. These two processes together resulted in the overall decrease in AR ability for samples with increasing RTA temperature [17].

## 2.3 rARSS Fabrication on Non-Vitreous Materials: Difficulties and Potential Solutions

### 2.3.1 Introduction

While fabricating rARSS on vitreous materials such as FS has been demonstrated, and is mostly a question of optimizing the fabrication process for a specific tool or target wavelength for maximum transmission, the same cannot be said for non-vitreous materials. For many applications optical components need to be made of a polycrystalline, crystalline, or compressed powder material, and so it is desirable to have a rARSS fabrication process that will work on these materials.

### 2.3.2 Spinel results

A material that is moderately used at present, for its near-ultra violet, visible, and mid-infrared transmission abilities, as well as its extremely durable physical properties, is spinel ($MgAl_2O_4$) [47]. Synthetic spinel is manufactured from a compressed powder and therefore it is neither vitreous nor single crystal. Instead, it is made up of many crystalline grains, each with their own random orientation [48].

Transferring the FS rARSS fabrication process to spinel was originally attempted, without major modifications, except that spinel is a much harder material than FS [49], and so it was expected that a longer or harsher etch process may be needed. After many different iterations of etch processes (changing various etch parameters such as power, gas chemistry, etch time, and gas flow rates, and using different metals as a masking layer) typical results looked like the images shown in Fig. 17. Various different orientation grains etched differently, resulting in an extremely inhomogeneous surface. In the example shown here the shallowest etch was also the roughest surface, and as the etch depth increased, the roughness decreased. This inhomogeneity led to increased scatter and a loss of transmission compared to unprocessed spinel as shown in Fig. 18. A rARSS fabrication process requiring direct etching of the spinel substrate was ineffective.

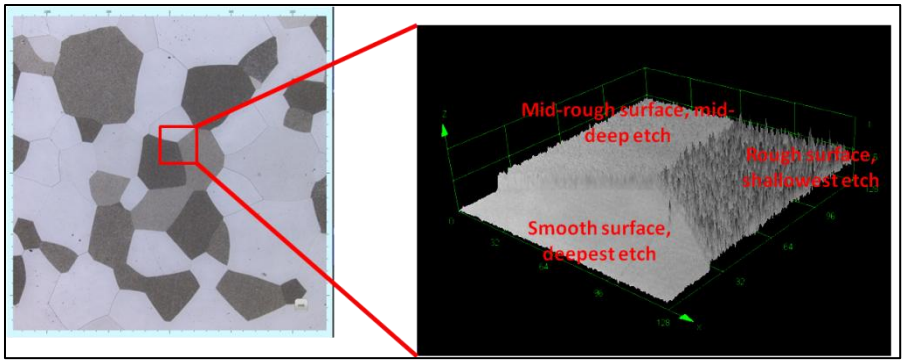


Figure 17: (Left) 5x confocal microscope image of spinel surface fabricated utilizing FS rARSS process parameters. (Right) 3D confocal microscope image showing differences in roughness and etch depth for three adjoining grains with different orientations. The deepest etched areas correspond to the smoothest surface and the shallowest etches correspond to the roughest surfaces.

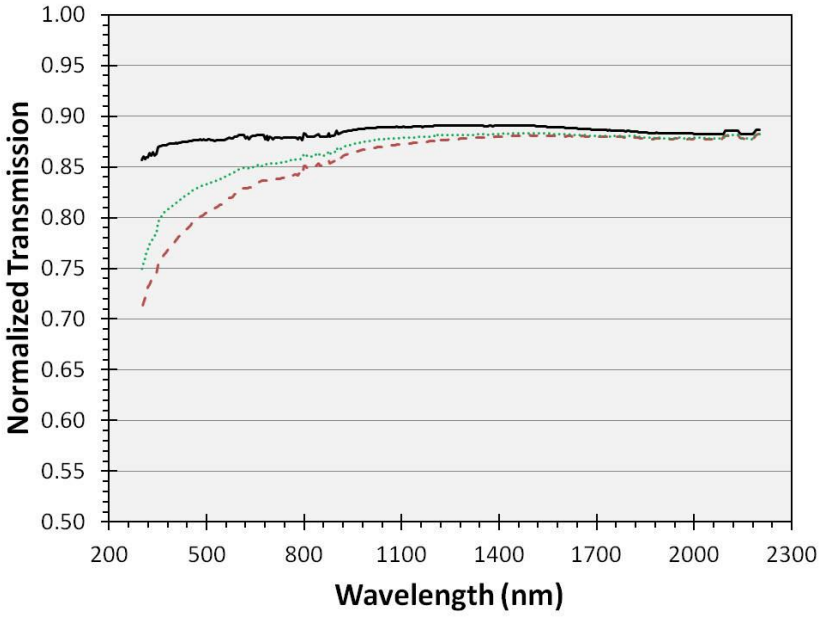


Figure 18: Transmission spectra of unprocessed spinel (solid black line), and two rARSS processed spinel samples with the "grainy" appearance shown in Fig. 17. Both processed samples show increased scatter in the visible and near IR regions, and their maximum transmission does not exceed the transmission of the unprocessed spinel sample.

### 2.3.3 Initial Testing of PECVD Deposited $SiO_2$ and Etching

With direct etching of the spinel substrate's surface shown to not be a viable option for fabricating rARSS on this material, another method was attempted. Since the key to the randomized etch process success seemed to be dependent on the amorphous nature of fused silica, the question became how could we obtain this property on a polycrystalline substrate? Since the substrate's composition cannot be changed, adding a layer of amorphous material on top of the substrate and roughening that material could be a solution to allow for rARSS fabrication on all types of substrates.

Applying a thin film to a substrate and then roughening it with rARSS will still involve a refractive index mismatch at the boundary between the thin film and the substrate, which will cause Fresnel reflection. However, if the index of refraction of the thin film and the substrate are very closely matched, the reflection coefficient should be a small percentage of the total incident light. For example, at 1 μm the refractive index of spinel is 1.70 [49]. Aluminum oxide ($Al_2O_3$) deposited via e-beam evaporation on the Kurt J. Lesker PVD 75 in the UNC Charlotte cleanroom was measured via ellipsometry to have an average refractive index of 1.621, also at 1 μm. At normal incidence, the percentage of light reflected as it moves from $Al_2O_3$ to spinel can be found using the Fresnel formula:

$$R = \left(\frac{n_1 - n_2}{n_1 + n_2}\right)^2 \quad (2)[50]$$

where $n_1$ is 1.621 and $n_2$ is 1.703. In this case the reflectance from this boundary would only amount to 0.06%. If the thin film and rARSS were applied to both surfaces of the substrate, and if the rARSS were to eliminate reflection from the air to the thin film, then

the total reflection for the system would only be 0.12%. This is a measurable improvement over the 13.06% reflection from two surfaces of bare spinel.

One of the advantages of rARSS over AR thin films is that rARSS can withstand much higher incident energy levels without damaging compared to thin films [28, 51-53]. It is assumed that this is the case because the rARSS are made up of the same material as the substrate they are applied to, damage thresholds close to the substrate's value are possible. Applying a thin film to the substrate's surface and adding rARSS to the thin film could result in the same high energy damage issues found with AR thin films.

Finally, as discussed in section 1.4, rARSS surfaces show increased polarization insensitivity with variable AOI over unprocessed substrates [26]. By having an unprocessed boundary between the thin film and the substrate, it is likely that this will introduce a polarization response to the layered film system. Also, by having a boundary from a higher index to a lower index on the back side of the system, this will introduce a critical angle to the system which could be observed at large AOI.

Applying rARSS to a thin film on top of spinel could be beneficial for applications where the key need is to have a broad bandwidth of anti-reflection. Also, applying one thin film and processing it with rARSS is a faster method than applying a multi-layer AR thin film. Because of this, it was decided to examine first if it was even possible to roughen a thin film applied to a substrate. It was decided that the first film to test would be silicon dioxide ($SiO_2$), the same chemical makeup as fused silica.

$SiO_2$ was deposited onto three different substrates, fused silica, single side polished silicon, and spinel using a PECVD. The PECVD recipe used called for 900 mTorr deposition pressure, nitrous oxide ($N_2O$) flowing at 1420 sccm, 2% silane ($SiH_4$)

flowing at 400 sccm, high frequency RF power of 30 W, low frequency RF power of 0 W, and a processing time of 14 minutes, 44 seconds. Three substrates were used in order to increase the number of trials. Once the deposition was complete, the thickness and index of refraction of the thin film on the silicon were measured using a J. A. Woollam WVASE32 ellipsometer (model 6460LV). The thickness was found to be approximately 950 nm and the refractive index measured is shown in Fig. 19.

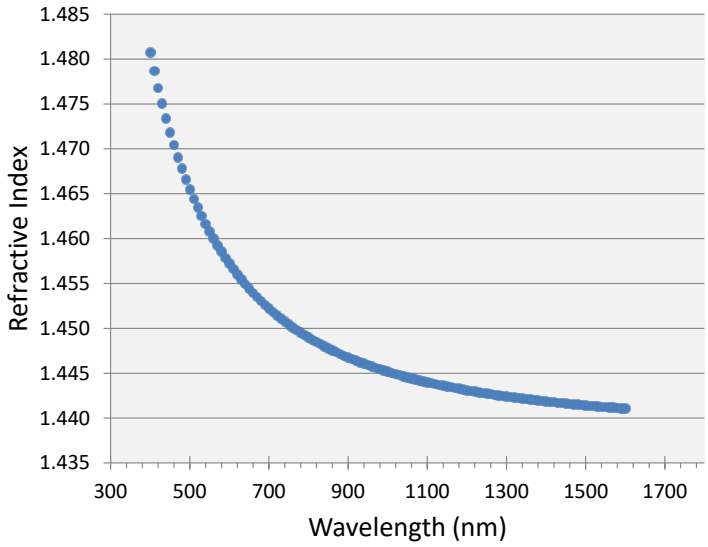


Figure 19: Plot of the modeled refractive index values of PECVD deposited $SiO_2$ thin films on single side polished silicon from 400 nm to 1600 nm. The refractive index was measured using a J. A. Woollam WVASE32 ellipsometer (model 6460LV) and fit to a Cauchy model.

Once the thickness of the thin film was determined, the samples were etched. Since there was no prior knowledge of how to etch thin films to induce roughness without completely stripping them away, many different etch recipes were tried, and after each etch the thickness of the film was measured via an Alpha Step Profilometer, and the roughness of the film was measured via a LEXT OLS4000 3D Measuring Laser Confocal

Microscope. The thickness measurements, combined with the etch time and other etch parameters allowed for the mapping of thin film etch rate, as shown in Fig. 20. Determining these etch rates was critical for further development of the rARSS on a thin film process because it helped to guarantee that an etch process that would completely strip away the deposited thin film would not be used. Since these tests were only designed to be a proof of concept, to the effect that thin films applied to substrates can be roughened, the transmission spectra of the samples were not collected.

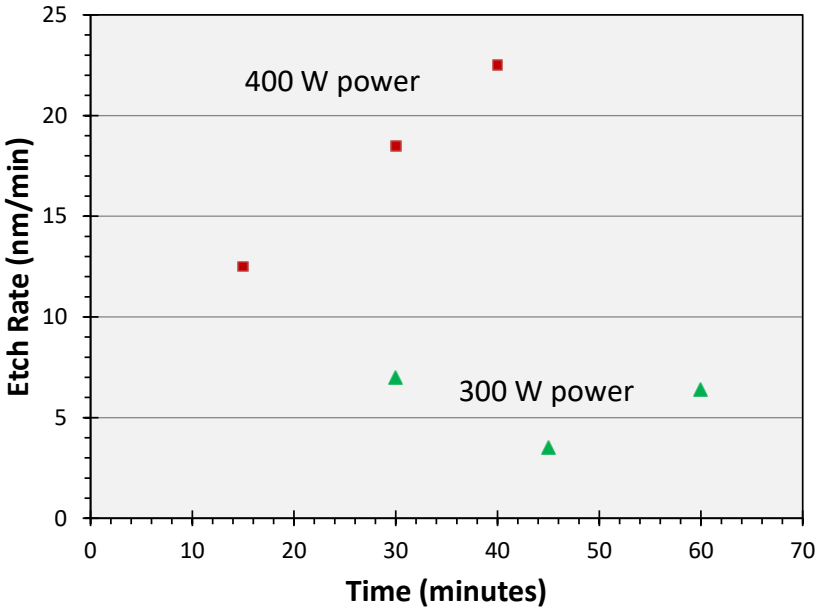


Figure 20: Plot of etch rates vs time for PECVD deposited $SiO_2$ on silicon for etch processes with 300 W bias power (green triangles) and 400 W bias power (red squares). Etch rates were measured by taping off a small corner of the sample before etching, then removing the tape after etching and using a profilometer to measure the etch step between the etched material and the area masked with tape. The etch step was then divided by the total etch time, resulting in the etch rate.

While not all of the etch trials for this experiment resulted in successful etching of the $SiO_2$ thin film, there were three that successfully roughened the thin film on silicon and the etch parameters can be found in Table 2. None of the spinel substrates showed any roughness in the $SiO_2$ films. The confocal microscope images of the roughened $SiO_2$ on silicon samples allowed for a comparison of the roughness found on the thin film to the roughness of a rARSS processed FS substrate and can be found in Fig. 21. Sample C showed roughness closest to the FS roughness, and was considered a successful proof of concept test of roughening a thin film applied to a substrate. Next it was important to study if a rARSS thin film system could be optimized for transmission enhancement.

Table 2: Etch parameters used on the PlasmaTherm RIE 7000 tool for etches that resulted in the successful roughening of a PECVD deposited thin film of $SiO_2$ on silicon.

| Sample | Power | Gas Flow Rate | Pressure | Time |
|---|---|---|---|---|
| A | 400 W | $O_2$: 5 sccm<br>$SF_6$: 50 sccm | 24 mTorr | 30 min |
| B | 300 W | $O_2$: 5 sccm<br>$SF_6$: 50 sccm | 24 mTorr | 45 min |
| C | 300 W | $O_2$: 5 sccm<br>$SF_6$: 50 sccm | 24 mTorr | 60 min |

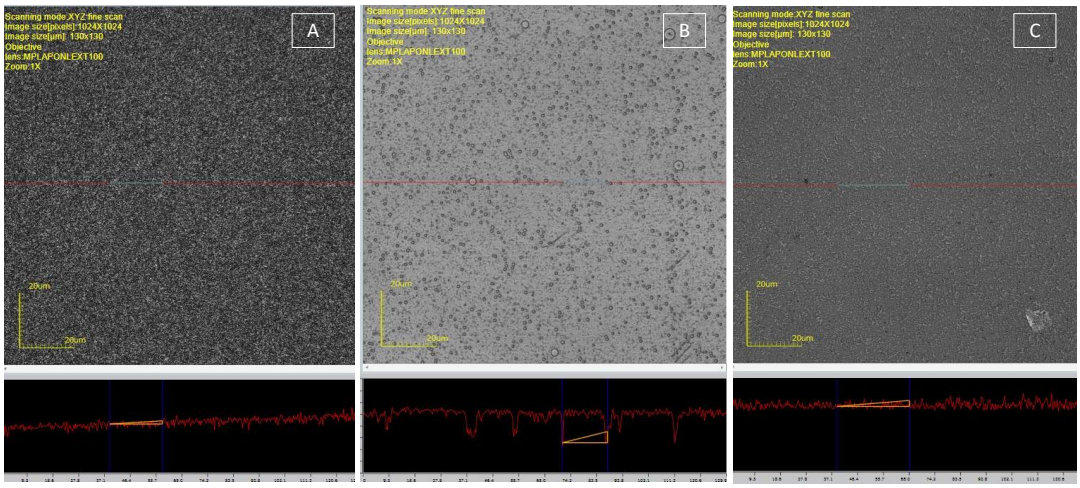


Figure 21: Top down laser confocal microscope images of roughened $SiO_2$ films on silicon. Sample labels A, B, and C correspond with the sample labels found in Table 2. The bottom rectangle shown for each sample is a cross sectional slice (corresponding to the red line in the upper images) showing the relative height of the surface features.

### 2.3.4 Summary

Attempts to produce optimized rARSS on spinel substrates using the fabrication process optimized for fused silica resulted in different roughness depths for spinel grains with different orientations. This caused increase scatter on the surface rather than increased transmission, and was determined to be an unviable method for fabricating rARSS onto such non-vitreous materials. An alternative method, where a thin film is applied to the non-vitreous substrate's surface and then rARSS is fabricated onto the thin film via reactive ion etching was proposed, and proof of concept tests were conducted using PECVD deposited $SiO_2$ on fused silica, spinel, and silicon substrates. The thickness of the film before etching was determined by ellipsometry, and profilometer measurements after etching allowed for the etch rates of the thin film to be plotted for

multiple etch powers. Three samples of $SiO_2$ on silicon were successfully roughened, and the proof of concept was demonstrated.

## 2.4 Gradient-Optical-Index Porous (GrIP) Coatings by Layer Co-deposition and Sacrificial Material Removal

### 2.4.1 Introduction

The experiment discussed in section 2.3.3 proved that it was possible to deposit a thin film onto the surface of a substrate and roughen the film using reactive ion etching. However the etch rate and confocal microscope data collected in that experiment showed that it is very difficult to get deep enough features to mimic the results seen with rARSS on FS in a thin film because the film etches away too quickly. Also, it was not possible to achieve roughness in $SiO_2$ films on spinel substrates. A material that would roughen easily but not etch so quickly that it removed the thin film completely was needed, but since there is not a material like this readily available, a method was developed to artificially create a thin film with both of those properties. This process was named "Gradient-Optical-Index Porous (GrIP) coating" [54] and relies on co-depositing an index matching material that is difficult to etch, and a sacrificial material that etches easily. After the co-deposition step is complete, an etch step removes the sacrificial material, leaving a rARSS surface made of the index-matching material. More details about the fabrication steps involved as well as the measured roughness and transmission results can be found in the following sections.

### 2.4.2 Fabrication of GrIP coatings

The principle behind the fabrication of GrIP coatings is that if a deposited thin film has two materials intermixed in such a way that the removal of one material leaves a grass like or porous structure of the second material behind, then rARSS structures could be created without using a direct etching process to roughen the thin film. This would address the problem of thin films either etching too quickly, and being removed completely, or etching too slowly, and not roughening at all. The formation of thin films has already been shown to begin with mobile clusters of the deposited material forming on the substrate and merging together to form larger islands, until the spaces between the islands eventually fill in and a continuous film is formed. The Stranski-Krastanov growth method theorizes that once the continuous film formation period has begun, any disruption to the binding energy of the film growth can cause the formation of islands on top of the thin film [22, 24]. The theory behind the GrIP coating fabrication method heavily relies on this island formation process to create an ideal intermix layer.

For this experiment, the goal was to produce rARSS on either spinel or sapphire, both of which are typically considered useful because of their physical hardness and transmission in the mid-IR wavelengths. Both materials have similar refractive index and Fresnel reflection coefficients (at 1μm the refractive index values are approximately 1.755 for sapphire and 1.703 for spinel [55, 56]), so an index matching material that works for one material should work for the other as well. In this case, $Al_2O_3$ was chosen as the index matching material, and a comparison of the measured refractive index value of electron-beam deposited $Al_2O_3$ vs the refractive indices of sapphire and spinel can be found in Fig. 22. The sacrificial material needed to be a material that etches easily, and so

it has already been shown that $SiO_2$ would be a logical choice. For this method, however, both materials must be deposited at the same time, under high-vacuum conditions, in the same tool. Both the AJA sputtering tool and the Lesker PVD 75 have the ability to deposit two materials at once, but previous attempts to deposit $Al_2O_3$ via sputtering yielded irreproducible results. To use the Lesker PVD to deposit two materials simultaneously, both the e-beam evaporation and thermal evaporation ports must be used. $Al_2O_3$ has a melting point of 2,072 ˚C but requires a temperature of at least 1,550 ˚C to produce $10^{-4}$ torr of vapor pressure (called the minimum evaporation temperature [22]) and can only be deposited using the e-beam method [57]. $SiO_2$ also has a high vapor pressure point (1,025 ˚C) and its preferred method of deposition is also e-beam evaporation [58]. Because it was not possible to have both materials deposited via e-beam evaporation at the same time, the process engineers at Kurt J. Lesker Company were consulted and they recommended using silicon monoxide (SiO) for the sacrificial material instead, because its vapor pressure point (850 ˚C ) is much more conducive to thermal evaporation methods [59]. Because SiO is silicon based, it would still etch quickly in the RIE tools available.

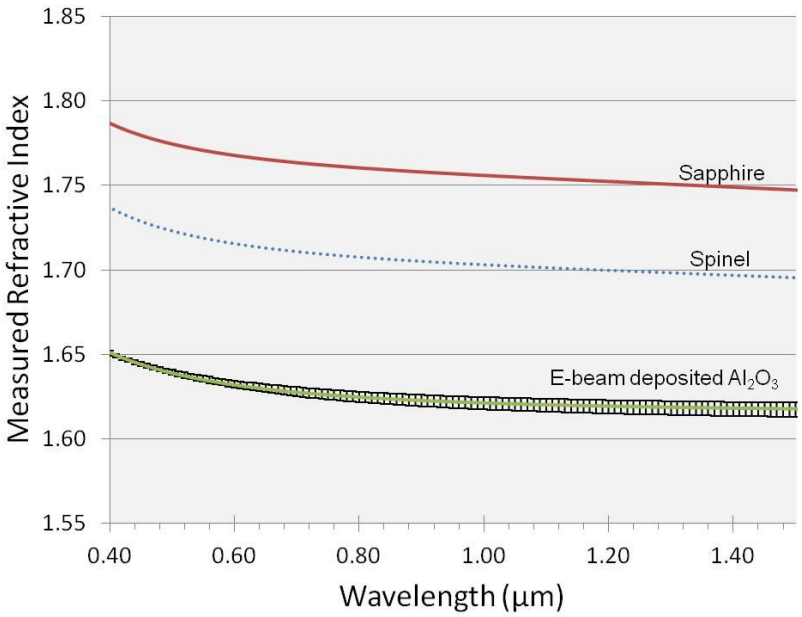


Figure 22: Refractive index values for sapphire (solid red line), spinel (dotted blue line) and e-beam deposited $Al_2O_3$ (solid green line with error bars). Sapphire and spinel values are from Refs. [55, 56], while the deposited $Al_2O_3$ is a measured average of three different e-beam depositions. The error bars indicate the maximum and minimum values measured for the three trials and the measurements were taken of $Al_2O_3$ deposited on single side polished silicon, using a WVASE ellipsometer.

Four different substrates were used in every test: single side polished silicon was used because the lack of reflection off of the back surface of the substrate made ellipsometry measurements of the deposited films easier, fused silica was used because it was a substrate that was easily obtained and the larger difference in refractive index between it and $Al_2O_3$ could allow for additional information about the deposited thin films to be obtained via spectroscopy, and spinel and sapphire substrates were used as they were the materials for which the process was being developed.

The deposition layers started with the index matching material ($Al_2O_3$) deposited onto the four substrates using e-beam evaporation in the high-vacuum conditions

(approximately 1.5 x $10^{-6}$ torr) of the Lesker PVD 75 tool. By first depositing only the index matching material, it promotes adhesion of the material to the substrate. Without removing the substrates from the vacuum chamber, the thermal evaporation source was activated to start depositing the SiO. During this step, the deposition rates of the $Al_2O_3$ and the SiO were adjusted to create an intermix region, in which the amount of each material was varied. For this stratum, three different modulation methods were attempted, shown in Fig. 23. Method I had the $Al_2O_3$ deposition start at its highest rate and decrease throughout the deposition process, while the SiO was started at its lowest rate and increased throughout the deposition run. Deposition method II had both the $Al_2O_3$ and the SiO start at their highest deposition rates (although not necessarily equal deposition rates) and the deposition rates of both materials were decreased throughout the deposition process. And finally, method III had the $Al_2O_3$ start at its highest deposition rate and decrease throughout the process while the SiO deposition rates stayed constant. The expectation was that with this co-deposition step, the deposition of the $Al_2O_3$ would be disrupted and the result would be a randomized mixture of the two materials which would gradually become more SiO than $Al_2O_3$. Once the modulation schedule was complete, the $Al_2O_3$ deposition was stopped and only the SiO was deposited for a short time. This period of SiO only deposition was used to seal the co-deposition layer with a layer of the sacrificial material.

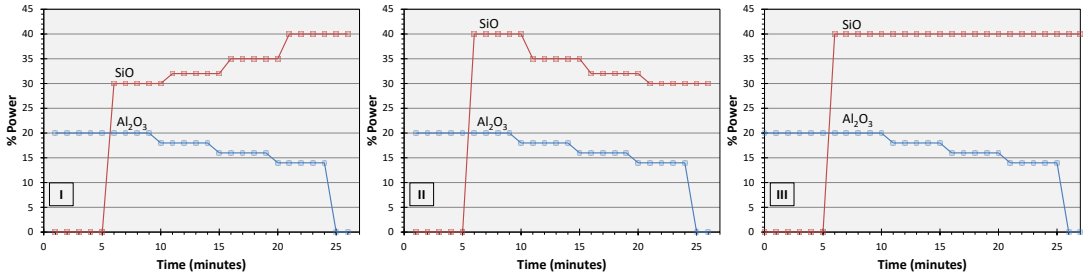


Figure 23: Deposition schedules for the $Al_2O_3$ and SiO. Roman numerals indicate the deposition run. Percent power values should not be compared between SiO and $Al_2O_3$ as they are being deposited using two different methods (thermal evaporation and electron beam evaporation, respectively) and thus, have different power requirements to achieve similar deposition rates. However, power rates for the same material can be compared between deposition runs to understand how the intermix region was modulated differently each time. It can be assumed that higher power for a specific material also means a higher deposition rate.

After the completion of the deposition process described above, the samples were removed from the PVD tool and were examined using the J. A. Woollam WVASE32 ellipsometer. This provided important information about the thicknesses of the $Al_2O_3$, intermix, and SiO layers as well as allowed for modeling of the gradient refractive index of the intermix layer. The samples were also examined using the UV confocal microscope to look for any roughness before etching, and their visible-IR transmission spectra were investigated using the Cary spectrometer.

Next the samples were subjected to a RIE step, which was designed to remove the top layer of SiO as well as the SiO in the intermix layer, leaving behind a porous, rARSS surface ideally consisting only of the $Al_2O_3$ on the substrate. The parameters for the RIE step were 300 W bias power, 24 mTorr chamber pressure, $SF_6$ flow rate of 50 sccm and $O_2$ flow rate of 5 sccm, and the parameters were selected based on information gathered

from previous experiments of etching thin films. To investigate how the material properties changed with etch time, etches were performed in 15 minute intervals, with confocal microscopy and transmission spectroscopy measurements taken after each etch. This provided insight into how the gradient-index effect caused by the rARSS evolved over etch time. An overview of the fabrication process can be found in Fig. 24.

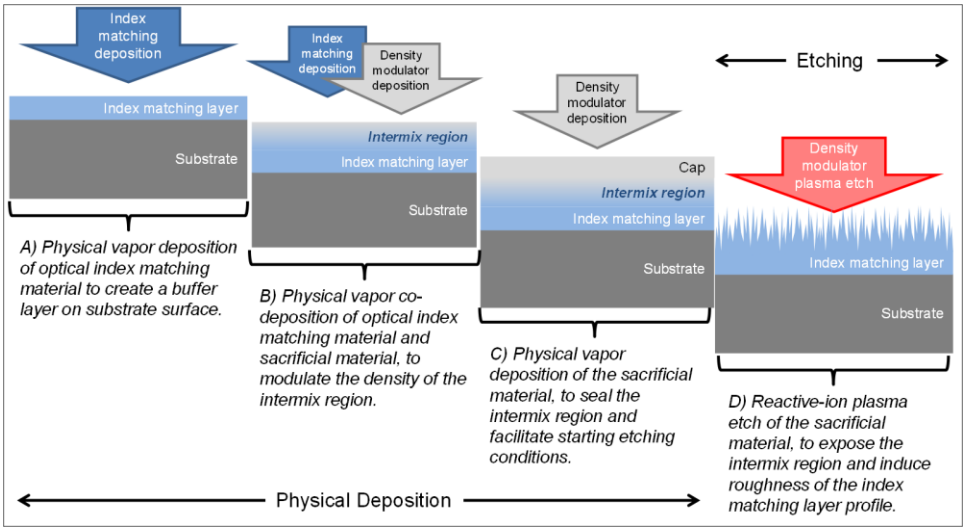


Figure 24: An overview of the four sequential steps used to form the GrIP layer on non-vitreous substrates from Ref. [54]. A) Physical vapor deposition of the optical index matching material on the substrate; B) Physical vapor co-deposition of the optical index matching material and the sacrificial material; C) Ending the physical vapor deposition cycle, with a sacrificial material cap; D) Etching of the sacrificial material using reactive-ion plasma in vacuum.

### 2.4.3 Results and Discussion

Figure 25 shows the film thicknesses measured via ellipsometry for each deposited layer and each deposition method. The Roman numerals correspond to the deposition methods discussed in section 2.4.2 and shown in Fig. 23. As expected, all three depositions have similar thicknesses of the $Al_2O_3$ layer, which can be attributed to

the fact that all three deposition runs started with 5 minutes of only $Al_2O_3$ being deposited at 20% power. The variation in thickness of this layer can be attributed to the fact that the tool was being controlled for electron beam power, not for the $Al_2O_3$ deposition rate and so the deposition rate may have fluctuated during the deposition time. Ideally for each of these steps a target deposition rate would be set and the tool would endeavor to keep the deposition rate constant, for a set amount of time, by varying the power as needed. During these depositions this was not an available option and instead the best alternative was to keep the power constant.

Another similarity between the three deposition methods was they all ended with a 2 minute "sealing" step where only the SiO was deposited. During deposition I and III the sealing step was performed at the highest power setting for the SiO, which should have resulted in a high deposition rate. For deposition II, the SiO sealing step was performed at a lower power setting than for depositions I and III, resulting in the much thinner SiO layer. Each deposition was conducted for the same total amount of time, regardless of how the evaporation powers were controlled during the run. This should result in the total amount of material deposited for each run being similar, and in this case the total material deposited was less than 9% different for all three depositions.

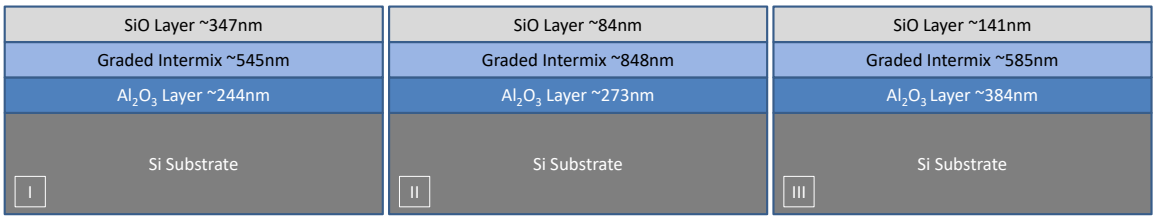


Figure 25: A WVASE spectroscopic ellipsometer was used to measure the deposited layers of $Al_2O_3$, the intermix region, and SiO on single side polished silicon substrates for all three deposition methods shown in Fig. 23.

In addition to the ellipsometer thickness measurements of the film layers, visible-IR transmission spectra at normal incidence were collected from 400 nm to 1600 nm. These transmission measurements were collected after the deposition step, but before any etching was done to the samples as well as after each 15 minute etch step. This allowed for the frequent monitoring of how the AR properties of the GrIP coatings were evolving with etch time. Figure 26 shows the transmission spectra of the deposited films on spinel for each of the three deposition trials, I, II, and III. It should be noted that the drop in transmission seen at wavelengths shorter than approximately 600 nm is caused by an absorption band of the SiO [60], not by scattering as seen in Figs. 7 & 12. Hass and Salzberg show that as a SiO film gets thicker, the transmission from 200 nm to 600 nm decreases (meaning there is more absorption) [60]. This seems to agree with the transmission results shown in Figs 26 and 27; the ellipsometric data indicated the thickest SiO layer was on deposition I, and the thinnest layer was on deposition II and the transmission data shows that deposition I has the steepest absorption features, while deposition II has the shallowest. The transmission results before etching on spinel, FS, and sapphire all also show fringe effects from reflection off the top and bottom surfaces of the various film layers interfering. These fringes are not as deep on the spinel and

sapphire substrates as they are on the FS substrates because there is not as large of a refractive index difference between the substrates and the films, but they are measurable.

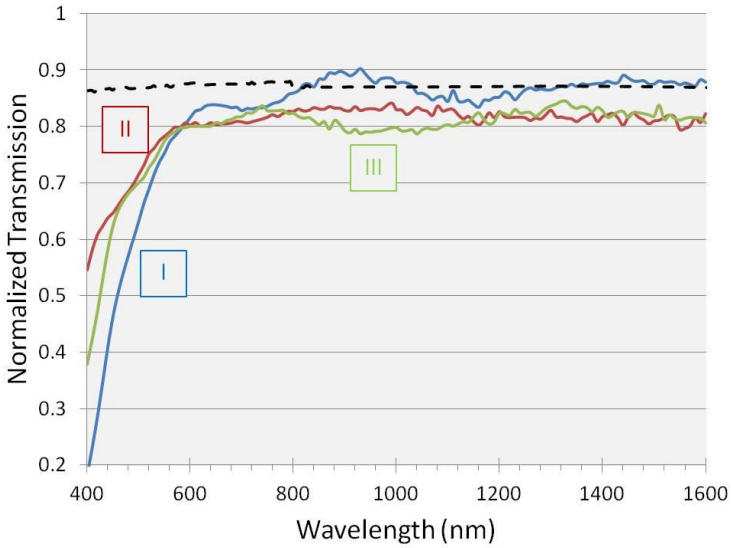


Figure 26: Transmission results from the three deposition trials on spinel. The black dashed line is unprocessed spinel, and the solid lines are transmission measurements taken after the deposition step was completed, but before any etching occurred. The Roman numerals correspond to the deposition trial numbers found in Figs. 23 and 25.

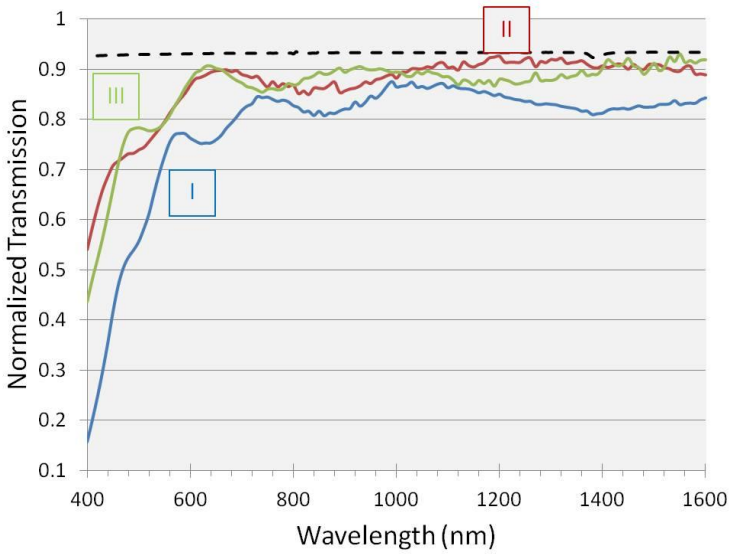


Figure 27: Transmission results from the three deposition trials on fused silica. The black dashed line is unprocessed FS, and the solid lines are transmission measurements taken after the deposition step was completed, but before any etching occurred. The Roman numerals correspond to the deposition trial numbers found in Figs. 23 and 25.

After the deposited samples had been tested, the etching process was begun. As discussed in section 2.4.2 the etch steps were conducted in 15 minute increments so as to allow for frequent transmission testing. Some scanning electron microscope (SEM) images were taken early on in the etching process to see if the films were roughening as intended. Figure 28 shows SEM images of deposition I and II on silicon, spinel, and FS taken after 15 minutes of etching. In these images it is clear that both depositions on all three substrates are roughening, although there is a definite difference in the size of the roughness between the three substrates. This can most likely be attributed to the difference in thermal conductivity and specific heat capacity between the three substrates, as shown in Table 3 [49, 61-63]. These differences result in the substrates heating differently while they etch, which can cause very different roughness results.

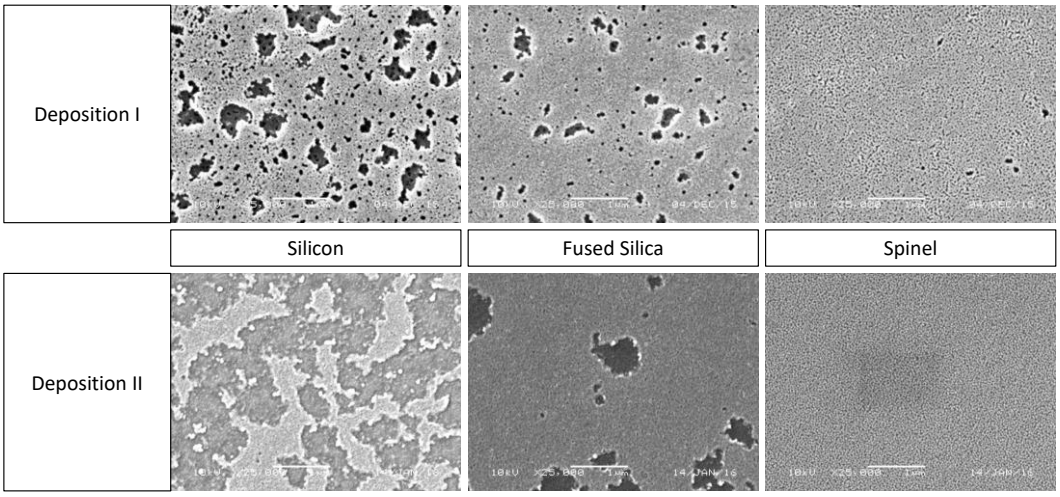


Figure 28: Scanning electron micrographs taken of deposition I and II samples on all three substrates after 15 minutes of etch time. The images are taken at 25,000x, the top row is deposition I and the bottom row is deposition II. Each column shows the results of the deposition and etch on a different substrate (from left to right: silicon, fused silica, and spinel). SEM images were not collected of deposition III.

Table 3: Thermal conductivity and specific heat capacity values for the four substrates used in the GrIP coating tests. These values were compiled from several references [49, 61-63].

| **Material** | **Thermal Conductivity W/m°K @ 25°C** | **Specific Heat Capacity J/(kg°C)** |
|---|---|---|
| Silicon | 148 | $0.712 \times 10^3$ |
| Fused silica | 1.5 | $1.0 \times 10^3$ |
| Spinel | 13.407 | $0.604 \times 10^3$ |
| Sapphire | 42 | $0.75 \times 10^3$ |

Figures 29, 30, 31, and 34 show how the transmission spectra of each deposition on spinel and sapphire change with etch time. Figure 32 shows the transmission enhancement (TE) for the etches with the highest transmission for each deposition, and Figs. 33 and 35 show the normalized transmission for the etches with the highest transmission for each deposition on fused silica and sapphire respectively. Deposition I and II on spinel show a general trend of increasing transmission with increasing etch time

up to a point of maximum transmission, and then decreasing transmission with every etch after that point. This is very different from the etching trends shown previously in Figs. 7 and 12 where changing an etch variable like the bias power or the RTA temperature would result in a red shifting of the whole spectrum, rather than raising or lowering the transmission across the spectral bandwidth. For deposition I on spinel the maximum transmission occurred after 90 minutes of etch time, and for deposition II the maximum transmission occurred after 45 minutes of etch time. Deposition III on spinel behaved slightly differently, with the transmission initially increasing with etch time, then decreasing, and then increasing again, while also flattening out. Deposition III comes the closest to the preferred shape of the transmission spectrum (generally flat over a broad spectral range) and shows an almost complete removal of the SiO absorption band, indicating that it is the sample containing the least amount of SiO at the end of the etch trials. Deposition II shows both the highest TE as well as the largest wavelength band for TE >3% of all of the depositions on spinel. This wavelength range is found to be  550 nm to 1220 nm, and then the TE increases again to over 3% at 1600 nm. It is important to remember that these substrates are only being processed with GrIP coatings on one side, leaving the back side of the substrate to still have approximately 7% reflection. This means that the maximum transmission enhancement obtainable in these experiments is approximately 7%, which deposition II attains from 800 nm to 820 nm.

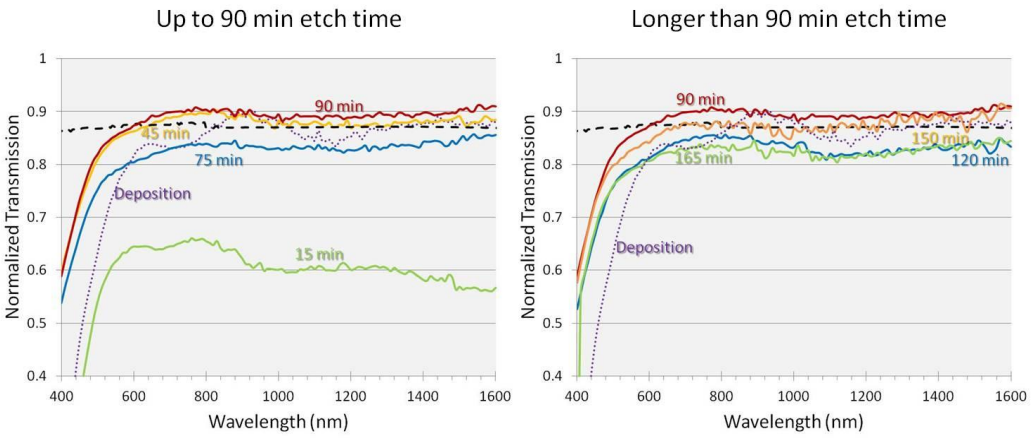


Figure 29: Transmission results with increasing etch time for deposition I on spinel. In both plots the black dashed line is unprocessed spinel, and the solid lines are transmission measurements taken after etches of various total etch time, as indicated on the graphs.

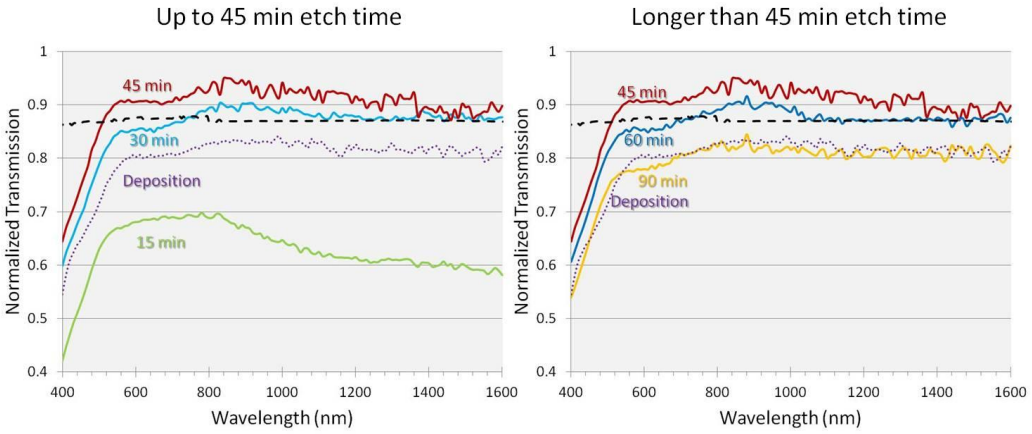


Figure 30: Transmission results with increasing etch time for deposition II on spinel. In both plots the black dashed line is unprocessed spinel, and the solid lines are transmission measurements taken after etches of various total etch time, as indicated on the graphs.

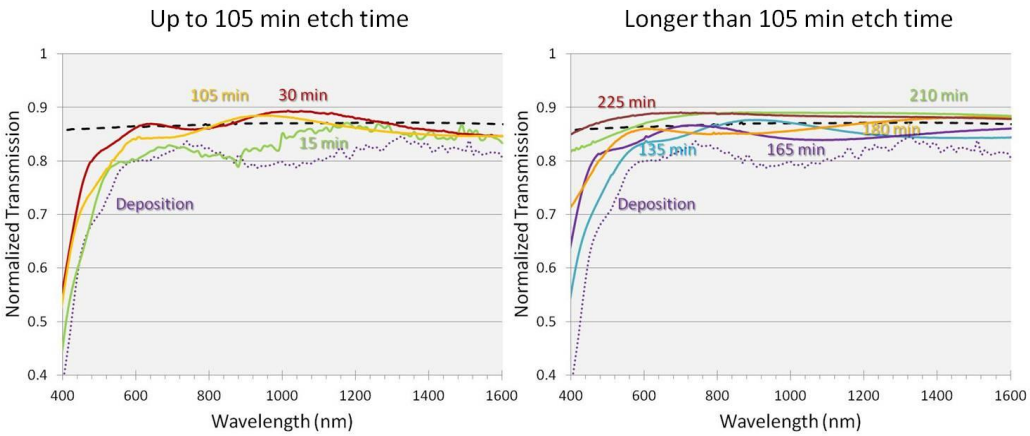


Figure 31: Transmission results with increasing etch time for deposition III on spinel. In both plots the black dashed line is unprocessed spinel, and the solid lines are transmission measurements taken after etches of various total etch time, as indicated on the graphs.

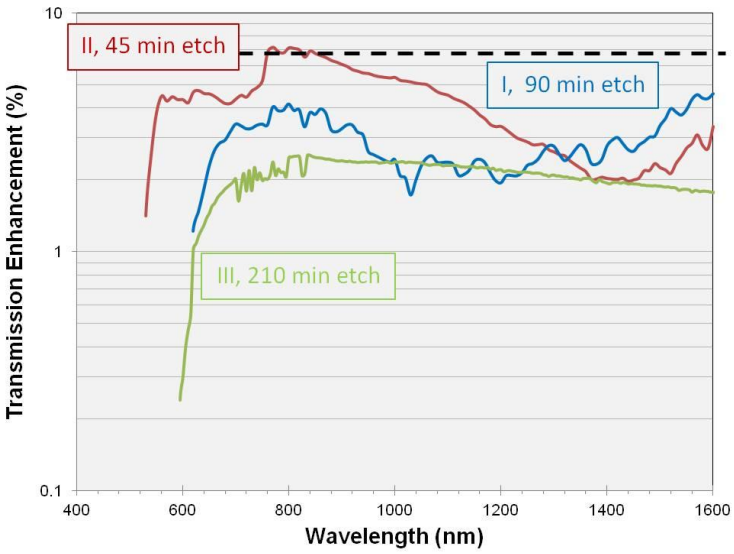


Figure 32: Transmission enhancement (TE) values from the three deposition trials on spinel shown on a logarithmic plot. The black dashed line is the maximum possible transmission enhancement for single side processed spinel, and the solid lines are the best transmission results seen throughout the etching process for each deposition trial. Each line has the deposition trial numeral as well as the etch time indicated on the graph.

Table 4: Wavelength ranges over which the measured TE is positive (transmission is higher than unprocessed spinel) and over which the measured TE is >3% (arbitrarily selected baseline). The results shown are for each deposition on spinel, and are only for the etches with the highest transmission values (found in Fig. 32). Deposition III does not have TE higher than 3% at any point.

| **Deposition and etch time of spectrum with highest %T** | **Wavelength range with positive TE** | **Wavelength range with TE above 3%** |
|---|---|---|
| Deposition I 90 min etch | 610 nm - 1600 nm | 690 nm - 950 nm<br>1480 nm - 1600 nm |
| Deposition II 45 min etch | 520 nm - 1600 nm | 550 nm - 1220 nm<br>1600 nm |
| Deposition III 210 min etch | 590 nm - 1600 nm | N/A |

Because fused silica was not the target substrate for the GrIP coatings, the transmission spectrum evolution with etch time is not included here. However, Fig. 33 does show the transmission spectra with maximum normalized transmission for each of the depositions on fused silica. It can be observed that none of the depositions result in transmission above the transmission of unprocessed FS, and this can be attributed to the fact that $Al_2O_3$ and SiO have a higher refractive index than FS. This means that the best transmission achievable is the transmission of unprocessed FS.

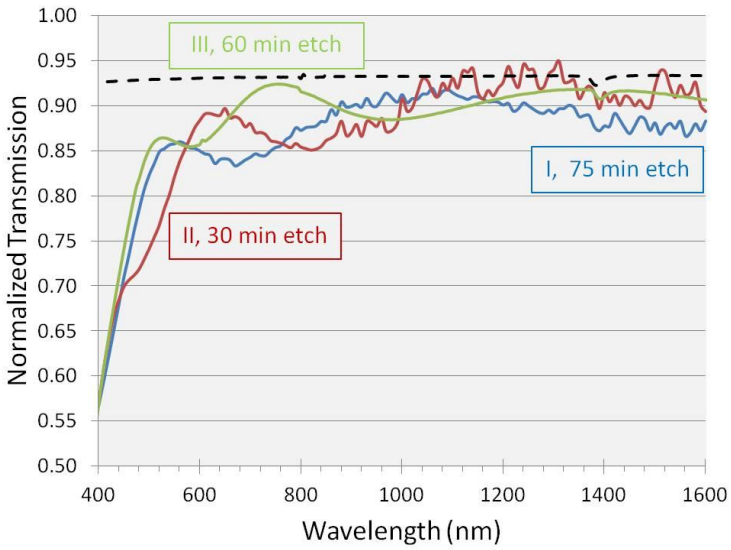


Figure 33: Transmission results from the three deposition trials on fused silica. The black dashed line is unprocessed FS, and the solid lines are the best transmission results seen throughout the etching process for each deposition trial. Each line has the deposition trial numeral as well as the etch time indicated on the graph. Note that because materials with a higher refractive index than the substrate (FS) have been applied, the normalized transmission can never be higher than the unprocessed substrate.

Sapphire substrates were obtained and added to the deposition III process. Since sapphire has a very similar refractive index to spinel, the deposition materials already selected would also be ideal for this substrate. Figure 34 shows the transmission spectra evolution with etch time for deposition III on sapphire. As expected, the transmission spectra trend seems to follow the trend seen with deposition III on spinel. In both cases the transmission increases to a relative maximum after 30 minutes, and then the transmission decreases again. Eventually the transmission increases again, finally resulting in a relatively flat transmission spectrum, with very little indication of a SiO absorption band at the lower wavelengths. This would indicate that of all of the depositions, method III results in the least amount of trapped SiO.

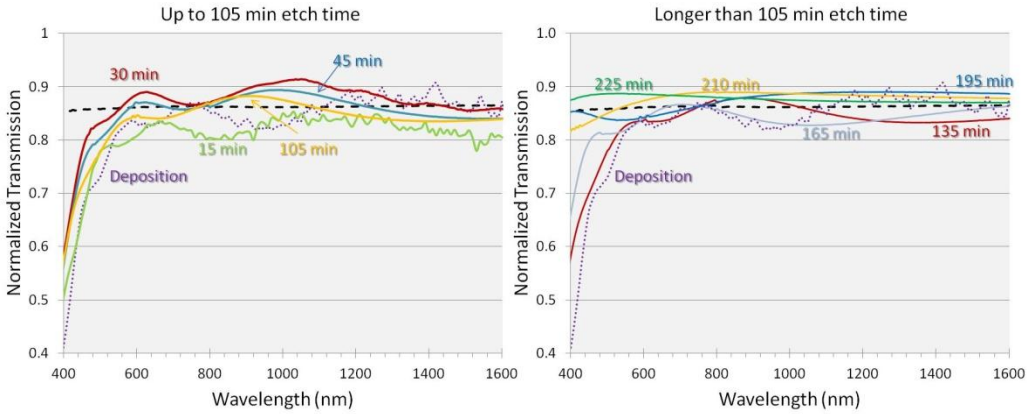


Figure 34: Transmission results with increasing etch time for deposition III on sapphire. In both plots the black dashed line is unprocessed sapphire, and the solid lines are transmission measurements taken after etches of various total etch time, as indicated on the graphs.

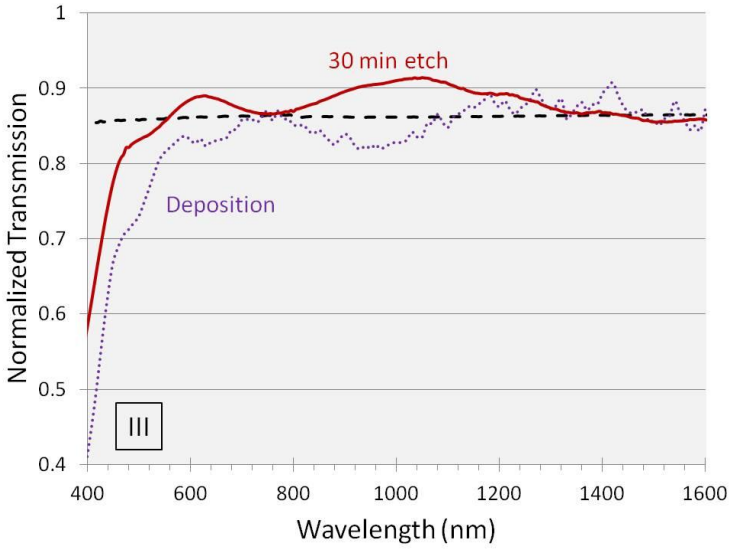


Figure 35: Transmission results from deposition III on sapphire. The black dashed line is unprocessed sapphire, the purple dotted line is after the deposition step was completed, but before any etching, and the red solid line is the etch run with the highest transmission result (with the etch time indicated on the graph). Only deposition III was attempted with sapphire because sapphire substrates were unavailable during depositions I and II.

The ideal result for the GrIP process would have been that the removal of the SiO material left behind a rough, rARSS aluminum oxide surface. The best way to observe the shape of the surface of the material was by imaging with an SEM, but this method requires sputtering the sample with gold for imaging, and then removing the material before starting the next etch. Because of the concern that this gold removal and subsequent surface cleaning might damage the deposited films, the SEM imaging was only completed for the first 60 minutes of etching on the fused silica and spinel samples deposited with methods I and II. Figure 36 shows that the spinel samples appear to be smoothing out with increased etch time rather than the preferred roughening. If this is the case for deposition III as well, then it would appear that the transmission enhancement seen in these trials is actually caused by the effect of a gradient thin film rather than by rARSS.

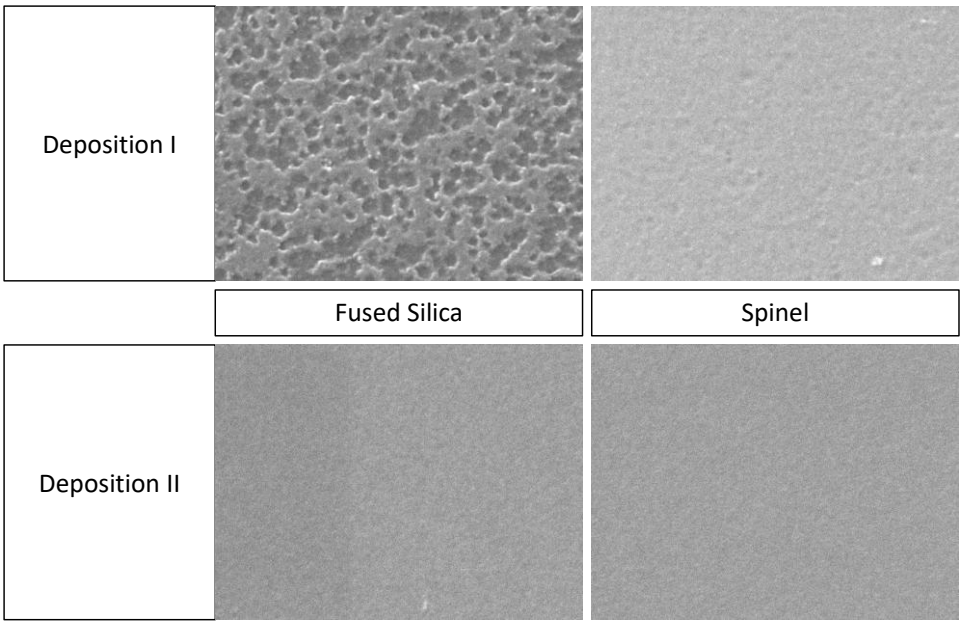


Figure 36: Scanning electron micrographs taken of deposition I and II samples on fused silica and spinel after 60 minutes of etch time. The images are taken at 25,000x, the top row is deposition I and the bottom row is deposition II. Each column shows the results of the deposition and etch on a different substrate (left, fused silica, right, spinel). SEM images were not collected of deposition III.

While these initial trials have not achieved formation of rARSS onto spinel or sapphire, they do show increased transmission which means that these GrIP coatings could be used to reduce reflection on non-vitreous materials. A benefit that would make further studies into this method worthwhile is the fact that GrIP coatings can be used on many different substrates, simply by changing the index matching and sacrificial material choices. For example, to use this process on germanium, germanium oxide could be used as the index matching layer, and silicon could be used as the sacrificial material. Also, depending on the depositing materials being used and the equipment available, the deposition process could be carried out via sputtering, rather than e-beam and thermal evaporation.

### 2.4.4 Summary

A new method of reducing reflection on non-vitreous materials called the Gradient-Optical-Index Porous (GrIP) coatings was proposed and attempted. Three different deposition trials were completed, where an index matching material ($Al_2O_3$) and a sacrificial material (SiO) were co-deposited using PVD methods and various deposition schedules. After ellipsometric measurements of the deposited films were completed, the films were then subjected to short reactive ion etching processes and the transmission was measured after each etch. The transmission measurements showed that all three deposition methods did result in increased transmission over unprocessed spinel, however only one method was able to reach the maximum transmission of a single side AR coated spinel substrate. SEM images taken over the first hour of etches showed that initial roughening of the sample surface was occurring, but the samples appeared to be smoothing out with increasing etch time. This would indicate that while the samples were showing increased transmission, it was most likely due to effective medium effects of the intermix layer.

## 2.5 Summary of Fabrication Methods Chapter

This chapter presented results from fabrication methods of rARSS applied to fused silica and non-vitreous substrates. In section 2.2, a common fabrication method for forming rARSS on fused silica was investigated. While the use of rapid thermal annealing of a thin metal film before etching a substrate has been seen in the literature, this section explored how the annealing temperature related to the feature sizes, and how that in turn affected the ultimate transmission spectrum of the sample. There are few

reports in the literature relating the size and depth of random ARSS features to the transmission properties, and this was a comprehensive look at the process and its variables. This work showed that the RTA step does not produce the desired transmission enhancement for a fused silica sample, and thus, is not necessary.

Section 2.2 addressed the fact that current methods for fabricating rARSS are typically only seen in the literature on vitreous materials, and the reason for that is because it does not work the same way on non-vitreous materials. Tests to produce rARSS on spinel using the FS fabrication method produced grains of various roughness parameters and simply increased the scatter in the system, with no noticeable increase in transmission. By depositing a thin film of $SiO_2$ onto a substrate's surface it was possible to artificially produce a uniform vitreous surface on a non-vitreous substrate, and experiments showed that this surface could be roughened on silicon substrates, but not on spinel substrates.

Finally, section 2.3 introduced a new engineered layer method to reduce reflection from the surface of non-vitreous substrates. By co-depositing an index matching material and a sacrificial (easily etched) material, and then removing the sacrificial material via reactive ion etching, it may be possible to form a porous AR surface. Initial tests showed that it was possible to reduce reflection with this method, but that it may be because of effective medium effects rather than effects from a rough or porous surface. This method can be adapted to many different substrates simply by changing the materials used as the index matching and sacrificial materials, which may be worth further study.

# CHAPTER 3: INVESTIGATION OF THE OPTICAL PERFORMANCE OF MICROLENS ARRAYS PROCESSED WITH RANDOM ANTI-REFLECTION STRUCTURED SURFACES

## 3.1 Introduction

Chapter 2 focused on characterizing the optical performance of rARSS on fused silica and non-vitreous flat substrates. It is common to find testing on flat substrates in the literature because it is simpler to evaluate. Fabrication processes that are top-down directional in nature, such as the RIE process used in this dissertation, should perform the same across the whole sample, and processes that require coating the substrate with a material should be relatively simple on flat substrates. Also, transmission measurements are straight forward as no focusing of the beam is occurring. The literature to date has numerous studies of how to fabricate ARSS on flat substrates with various methods and process parameter tests, while there is relatively little analysis and measurements found about testing ARSS on curved optical components. As mentioned in Chapter 1, Courtney Taylor did one of the first comprehensive studies of rARSS on curved surfaces, when she investigated how the transmission enhancement abilities of rARSS on 1” diameter fused silica lenses, of various effective focal lengths, compared to rARSS on flat fused silica samples as well as AR coated lenses. She carried out extensive testing of the lenses and flats, at various radial positions and angles of incidence, and found that even a rARSS fabrication process that was optimized for flat substrates can have a comparable performance to a single layer AR thin film applied to the same optic [31, 32].

Because this chapter focuses on the optical performance of rARSS on microlens arrays, it is important to thoroughly discuss any similar studies in the literature, of which

there are a few. In most cases, as discussed in Chapter 1, the only data presented by the authors is SEM and/or atomic force microscope (AFM) images of the subwavelength structures, or transmission or reflection spectra comparing ARSS processed MLAs with unprocessed ones [43, 64, 65]. There are a few papers that attempt to look closer at the optical performance of these ARSS processed MLAs, and they do it in several different ways. Baroni et al. used a Mach-Zehnder interferometric microscope to calculate the Strehl ratio of a single microlens with periodic ARSS applied to the curved surface. They show that depending on which lens is examined, their quartz microlenses without surface structures have Strehl ratios between 0.92 and 0.99. When they measured the Strehl ratio for the ARSS processed microlenses, the value went down slightly to approximately 0.9, and a phase image of the lenses showed that the outer part of the lens was responsible for the new aberrations. Since this value was still above the conventionally accepted Strehl ratio value of 0.8, the process was deemed successful [66]. Chen et al. attempted to study the diffusive properties of MLAs with ARSS applied to their curved surfaces. They did this by using a CCD camera to image a collimated beam passing through the MLA, then splitting the image into nine segments and recording the intensity value at the center of each segment. The uniformity was defined as the minimum recorded intensity value divided by the maximum recorded intensity value and it was found that for both the flat polycarbonate (PC) film and the PC film with MLAs, the ARSS increased the uniformity value [39]. The increase in uniformity with the application of ARSS indicated that the surface structures are actually increasing the scatter in their system, and the increased

transmission values presented in this paper may be misleading due to their usage of an integrating sphere as a detector.

Two papers were found that attempted to investigate the effect of the ARSS on the MLAs focusing ability. In the paper by Chen et al., they investigated the optical quality of the MLA with ARSS on the curved surface by using a light focusing system that would direct an expanded laser beam onto multiple microlenses and then used a CCD camera to image the focal spots. Unfortunately, the only data presented in the paper was the image of the focal spots of the ARSS processed MLA, which were too small to see any detail other than the general intensity and spot size throughout the image was uniform. They also did not compare the focal spots of the processed MLA to an unprocessed MLA. The authors measured the focal length of the ARSS processed MLA at various locations over the array and confirmed that the focal length was relatively uniform, but again they did not compare the focal length of the processed MLA to that of an unprocessed MLA [67]. By comparison, Jung and Jeong's paper studied the lens performance of the ARSS processed MLAs using a transmission confocal laser scanning microscope, which allowed them to produce images of how the beam converges to focus and diverges after focus. They then compared the ARSS processed MLAs with identical but unprocessed MLAs and determined that neither the focal length nor the full width at half maximum of the beam spot was effected by the application of ARSS. The authors also showed images and intensity distributions of the processed and unprocessed MLAs projecting images of a transparent letter F to demonstrate that the application of the ARSS onto the MLAs would increase the image brightness [68].

This work intends to fully characterize the optical performance of fused silica MLAs processed with rARSS that was optimized for application onto flat substrates. MLAs with three different effective focal lengths are used to investigate if the aspect ratio of the microlenses will impact the effectiveness of the rARSS. The MLAs were all purchased from Edmund Optics, all are spherical lenses laid out on a square grid, and their specifications can be found in Table 5.

Table 5: Specifications for the MLAs used in Chapter 3.

| Sample | Divergence Angle | Effective Focal Length | Lens Diameter | Lens Period | Lens Sag | Lens Radius of Curvature | MLA Thickness |
|---|---|---|---|---|---|---|---|
| A | 2.0° | 4.80 mm | 300 μm | 300 μm | 5.1 μm | 2.2 mm | 0.9 mm |
| B | 1.0° | 8.70 mm | 300 μm | 300 μm | 2.8 μm | 4.0 mm | 1.2 mm |
| C | 0.5° | 18.8 mm | 300 μm | 300 μm | 1.3 μm | 8.6 mm | 1.2 mm |

Section 3.2 will focus on the fabrication of rARSS on both sides of the FS MLAs as well as the characterization of the physical properties of the rARSS processed MLAs, such as the statistical distribution of the feature sizes and the feature depths. This section will utilize the same methods used in Chapter 2 to determine the physical characteristics of rARSS on planar FS substrates: SEM images and granulometry.

Section 3.3 is the first section dealing with the characterization of the optical properties of the MLAs, and it will specifically examine the focusing ability of rARSS processed MLAs as well as the beam propagation. In this section, as well as sections 3.4 and 3.5, there will be comparisons between rARSS processed MLAs and unprocessed MLAs, as well as between MLAs with different aspect ratios. Zemax simulations are

shown to verify the experimental design, and power measurements are also conducted to confirm the rARSS transmission enhancing abilities when applied to MLAs.

Section 3.4 is an investigation of the far-field propagation characteristics of the rARSS processed MLAs. It will examine the Fourier transforms of the MLAs and compare the far-field response of the processed MLAs to the unprocessed MLAs. The MLA is placed at the front focal plane of a 1" diameter lens and the beam profile is examined at the back focal plane. This section will be accompanied by analysis of the setup to confirm the values being obtained are correct.

Finally, section 3.5 will summarize the results from the previous sections and draw some final conclusions about the optical performance of MLAs processed with rARSS.

## 3.2 Fabrication of rARSS on Fused Silica Microlens Arrays

### 3.2.1 Fabrication Steps

Fabrication of rARSS on fused silica MLAs was carried out much like the rARSS was fabricated on planar FS in section 2.2.2. First, the MLAs and a FS flat (as a witness sample) were all sputtered together with a thin discontinuous layer of gold on the curved side of the arrays. After sputtering, the samples were transferred to the PlasmaTherm RIE 7000 where they were all etched simultaneously for 45 minutes at 24 mTorr of pressure, 550 W power, 50 sccm $SF_6$ and 5 sccm $O_2$. These etch parameters had been previously optimized for maximum transmission enhancement at 633 nm wavelength on flat FS substrates, and no further optimization was performed. After the first RIE step was

concluded, the samples were removed and the sputtering and etching process was repeated for the flat sides of the substrates (and the opposite side of the witness sample). This resulted in samples that were processed with rARSS on both sides. To inspect this process, UV laser confocal microscope images were taken of the curved sides of the MLAs before and after etching and they can be seen in Fig. 37. The images of the unprocessed MLAs are in the left column and the images of the MLAs after rARSS fabrication are in the right column. Sample letters are preceded by U for unprocessed or AR for rARSS processed and this notation will be continued throughout the chapter. It should be noted that the unprocessed samples show a much larger difference in reflected intensity over a microlens than their rARSS processed counterparts. This is because the UV laser confocal microscope measures the intensity of the reflected light. With the application of the rARSS the reflected light is reduced, resulting in the appearance of a smaller intensity gradient across a lens. Figure 37 also illustrates the difference in aspect ratio between the three different MLAs, as the Z factor is set to be equal for all six images shown.

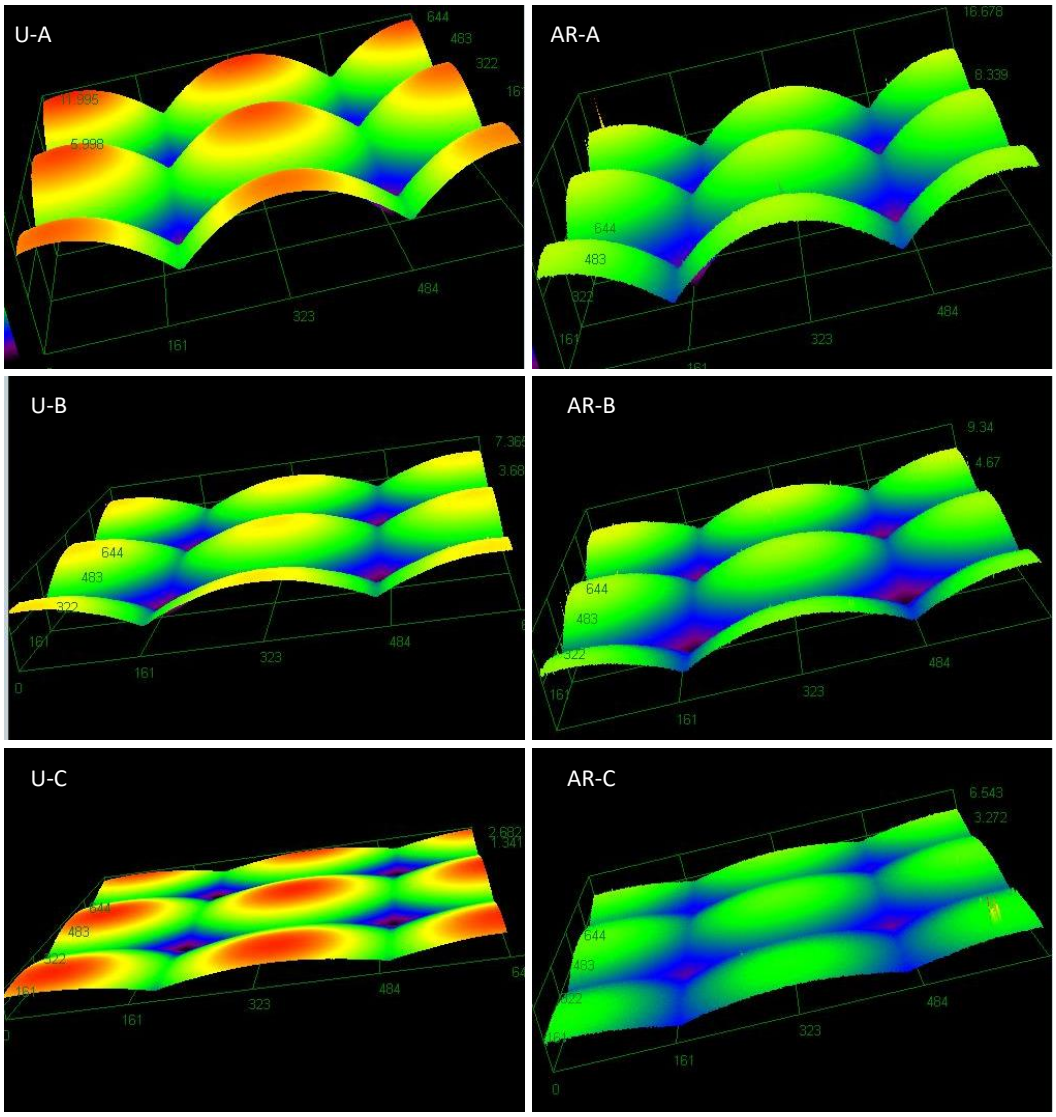


Figure 37: UV laser confocal microscope images of all three MLAs, both before any processing was done (left column) and after rARSS was applied to the curved side of the array (right column). In all images the Z factor was kept constant and unprocessed samples are indicated by a “U” in front of the sample letter and rARSS samples are indicated by an “AR” in front of the sample letter. Colors do not correspond to height differences between images.

### 3.2.2 Scanning Electron Microscope Images and Granulometry Results

Scanning electron microscope (SEM) images were taken of the curved side of the rARSS MLAs. Because it was impossible to see the individual lenses using the SEM due to the soft lens profiles, it was difficult to identify which part of a lens was being imaged. Instead, several images were taken of the surfaces, each 100 μm apart. Since the lenses were 300 μm in diameter, taking 4 images in the x direction sampled across the entire profile of a lens. Sample AR-B (1°) was experiencing too much charging from the electron beam and images were unable to be collected, but images were obtained for AR-A (2°) and AR-C (0.5°) which had larger and smaller aspect ratios respectively, so if there is a difference in physical feature sizes because of aspect ratio, this should still be able to be identified.

SEM images taken at 20,000 times magnification of samples AR-A and AR-C are shown in the top and bottom rows of Fig. 38 respectively. The second image on a sample is a minimum of 100 μm away from the location of the first image and every image was taken with the same working distance and accelerating voltage. Qualitatively, there is not a noticeable difference in physical feature size between images taken at two locations on the same sample, nor is there a noticeable difference between images of the two different MLAs. To quantitatively assess if this is true, granulometry and an image processing routine which consisted of median-gray-value thresholding, to ensure that brightness and contrast differences during imaging would not skew the granulometry results, was used. The bright pixel clusters in the images indicate elevated features, i.e. silica islands, whereas the dark clusters identify voids. Islands and voids were classified separately,

using gray-scale inversion of the images and counting the granule populations independently. The granules used for classification were octagons, varying from 5 to 50 pixels in diagonal, and scaled to the dimensional bar for each SEM image. Multiple areas of each surface were imaged, and the results were kept separate to evaluate the surface morphology at different points on the MLA. The granule pattern spectrum $\Phi(k)$ and its derivative $d\Phi(k)$, for both islands and voids of diagonal dimension $k$ were computed for each location, to obtain the FS density distribution by granule (feature), and the granule size histogram populations respectively. The difference of island to void distribution: $\Phi_{islands}(k) - \Phi_{voids}(k)$, and the population difference of islands to voids: $d\Phi_{islands}(k) - d\Phi_{voids}(k)$, were calculated to identify the effective density of FS in the imaged surfaces and the feature size dominance.

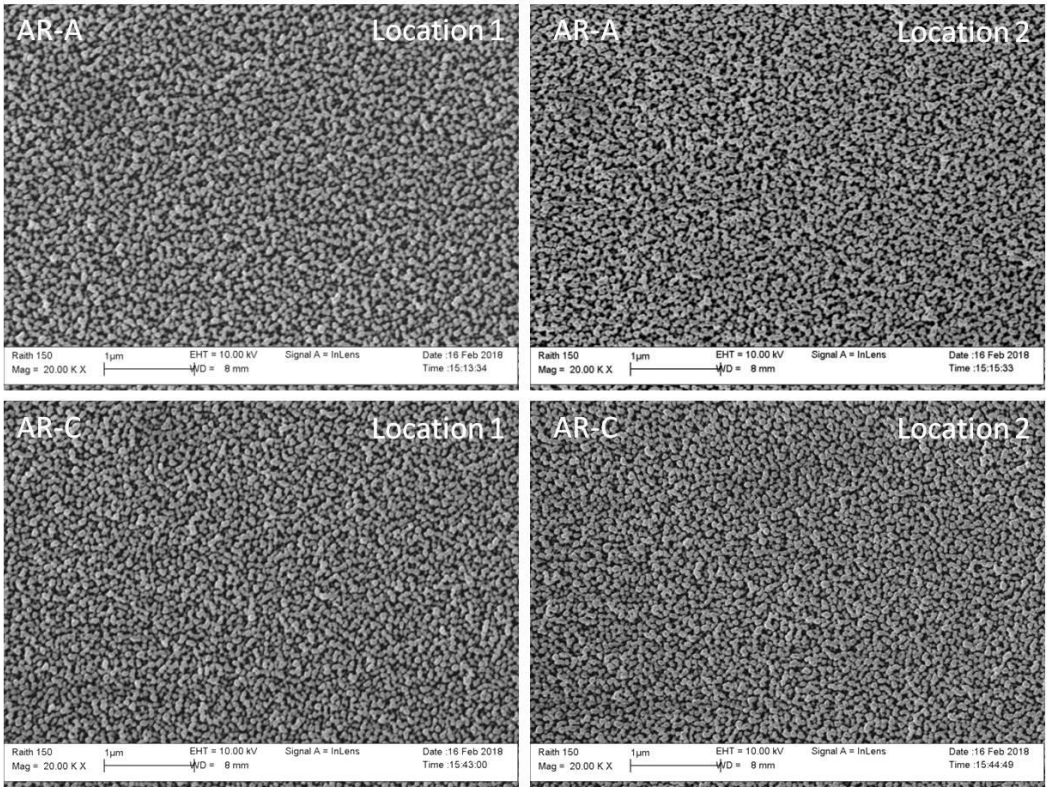


Figure 38: Scanning electron micrographs of samples AR-A (top row) and AR-C (bottom row). All samples were taken with the same working distance and accelerating voltage and all were taken at 20,000 times magnification. Images on each sample were taken a minimum of 100 μm apart to investigate the structures at different points on a microlens. Labeled locations are not necessarily the same across MLAs, due to the lack of identifying features.

The granule pattern normalized spectrums $\Phi(k)$ and their derivatives $d\Phi(k)$ were calculated for both islands and voids of diameter $k$, using SEM images similar to the ones shown in Fig. 38. These two quantities correspond respectively to the discrete probability distribution function of the respective features, and the discrete feature spectrum (histogram). Both feature-type distribution functions are bound by the condition:

$$\Phi_{islands}(k) + \Phi_{voids}(k) \leq 1 \tag{3}$$

The equality is true only for $k = \infty$, meaning that when all feature diameters are counted, the SEM image balance of islands to voids is obtained. At some value $k_{max}$ the counting will not yield new features, and the granulometry will stagnate. Conversely, if feature sizes smaller than $k_{min}$ don't exist, the population count will not start. This condition doesn't imply any type of interdependence of the distributions, which are totally independent variables. In turn, the feature spectrum is peaked at the mean value of each normalized distribution function, i.e.:

$$\mathrm{d}\,\Phi\,(k) \leq \mathrm{d}\,\Phi\,(k_{mean}) \tag{4}$$

where:

$$\Phi\,(k_{mean}) = \tfrac{1}{2}\Phi\,(\infty) \tag{5}$$

The product of each population distribution with the corresponding feature spectrum $\Phi(k)d\Phi(k)$, for each MLA is shown in Fig. 39. The product of the granulometry results was used instead of the individual values, in order to "weigh" the population histograms with the population distributions. The resulting distributed histogram displays the feature sizes and the feature balance in compact form. The mean value of each feature of interest is indicated by the histogram peak, with the population balance as the ratio of the two population mean values. Dominance of a certain feature size over the other is indicated by the bar ratios at the specific granule size.

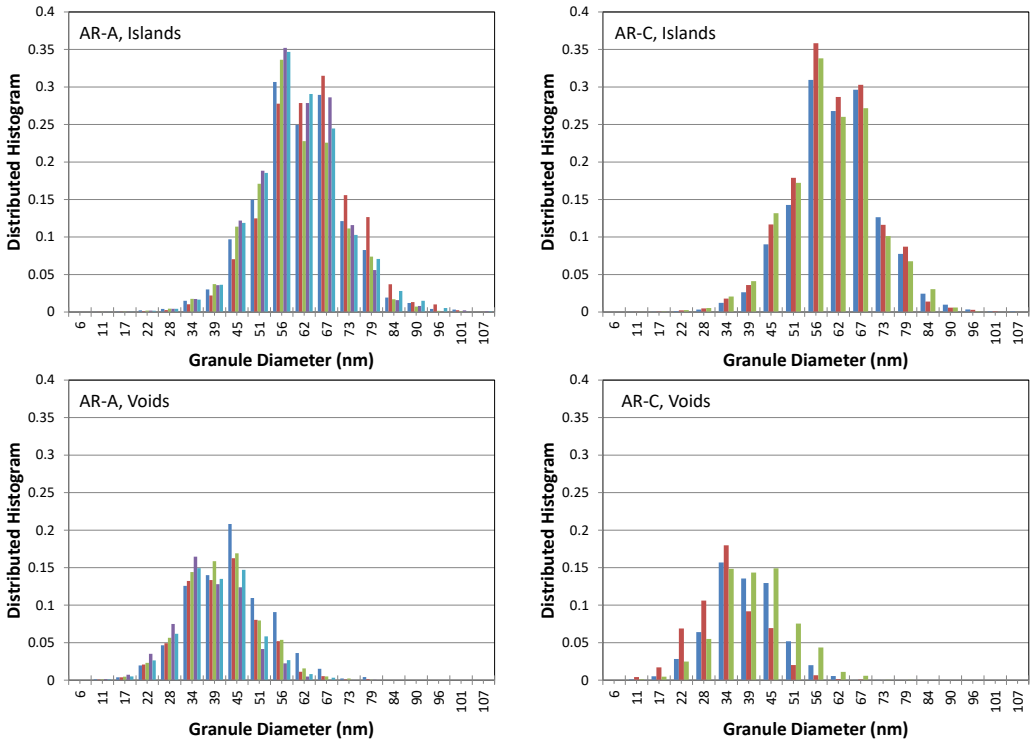


Figure 39: Distributed histograms of islands (top row) and voids (bottom row) from the feature sizes corresponding to the SEM micrographs of the random structure AR boundaries shown in Fig. 38. The identifiers (AR-A and AR-C) correspond to the rARSS processed samples from Table 5. The different color bars relate to SEM images taken from different locations on the MLA, and within a sample, one color of islands relates to the same location and same color with the voids. Since there was no way to globally orient the location of the images, the colors between samples do not necessarily correspond to the same locations. The histograms were computed using granulometry.

Figure 39 shows that both sample AR-A and AR-C have larger islands surrounded by smaller voids, with mean diameters of 56 nm and 34 nm respectively, and a roughly 65% - 35% coverage density. While there are some slight differences between the distributed histogram values for specific granule sizes across the multiple locations per sample, in general the trend is consistent between different MLAs and different locations on the MLA.

The morphological differences of the 2 MLAs and the different locations on the MLAs can also be quantified as actual differences between the constituent population normalized distributions $\Phi(k)$ and the differences of the products: $\Phi(k)d\Phi(k)$, from Fig. 39. Figure 40 (top row) displays the differential weighted-population ($\Phi_{islands}(k)d\Phi_{islands}(k) - \Phi_{voids}(k)d\Phi_{voids}(k)$) evolution, and Fig. 40 (bottom row) the population differential normalized distribution ($\Phi_{islands}(k) - \Phi_{voids}(k)$), with respect to granule size. The differential population (Fig. 40, top row) agrees with the conclusions drawn from the distributed histograms as it shows that various locations on both MLAs have similar features, with a predominance of FS islands (positive differential) in all cases. The differential distribution results (Fig. 40, bottom row) indicate that multiple locations across both MLAs have many small (< 50 nm) voids but then have a higher density of islands for larger granules (from approximately 56 nm to 102 nm). Combining the results displayed in Figs. 39 and 40, the transverse morphological constitution of the rARSS boundaries on MLAs of different aspect ratio is quantified.

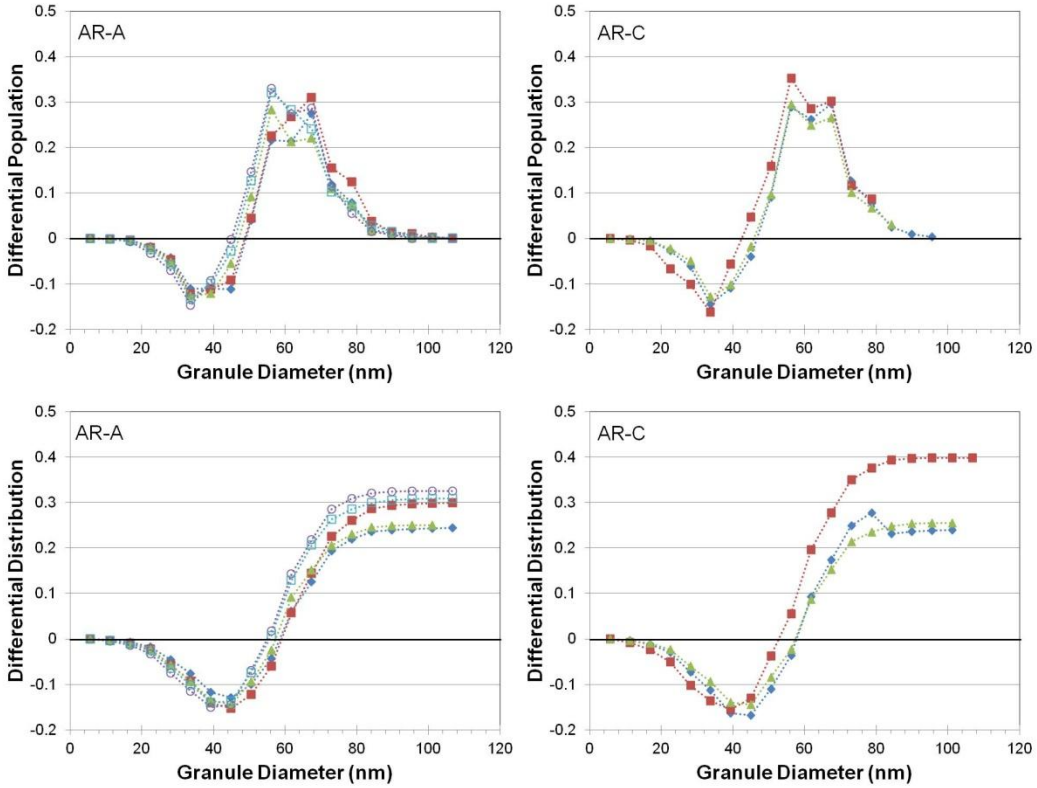


Figure 40: Differential population (top row) and differential normalized distribution (bottom row) of the granule sizes measured from the rARSS processed MLAs. The sample labels AR-A and AR-C correspond to the identifiers in Table 5. Positive numbers indicate a plurality of silica islands, where negative numbers indicate more voids (air) than islands. The trend lines are for ease in viewing.

The last detail needed to quantify the physical properties of the rARSS on MLAs was information about the depth of the features. The UV laser confocal microscope was used to obtain this information in Chapter 2, but the curved surface of the MLA makes this method unreliable because it relies on measuring reflected light that is collected by the microscope. Because the surfaces are curved, light will be reflected away from the microscope objective, resulting in skewed depth values. Cross sectional SEM images of the MLAs showing the rARSS on top would be an ideal solution in this case, but this was attempted and the curved surfaces of the MLAs again made these images unobtainable.

Instead, cross sectional SEM images of rARSS on planar fused silica are used and the depth of the structures is estimated to be an average of 265 nm [69].

## 3.3 Microlens Array Focal Spot and Beam Propagation Testing

### 3.3.1 Microlens Array Focal Spot Imaging System: Simulations and Tests

In order to test the focal spot of the processed and unprocessed MLAs a scanning slit beam profiler from Thorlabs was used. The three different MLAs all had short focal lengths, and so it was not possible to directly access their focal plane for measurement with the scanning slit. Instead, a system was built to image the focal point of the MLA to a point further away that the beam profiler could access. This system was designed and optimized in Zemax, and example results from MLA B (1.0° divergence angle) is shown in Fig. 41. The goal was to place the MLA in front of a 1" diameter lens at a distance that is the sum of their focal lengths. This would produce collimated light behind the 1" lens, which a second 1" lens could then refocus for the beam profiler to investigate. To optimize this system, lens parameters of the lenses to be used were obtained from the manufacturers' specifications and used with Zemax. To start, the MLA and the first 1" lens were placed at the sum of their focal lengths apart, and then the distance between them was optimized to have collimated light on the back side of the 1" lens. Then the second 1" lens was added to the system and the distance between it and the detector was optimized to obtain the smallest focal spot at the detector. This resulted in both the appropriate distances to use for the physical experiment, as well as a simulation of the beam profile at the focal point of the MLA to use as a comparison with the experimental

data. Figure 42 shows more detail of the optical setup, and Table 6 contains the distances used for testing each MLA investigated. In order to be able to test the beam profile of the MLAs through focus, the optical components contained within the dashed box in Fig. 42 were able to be moved along the optic axis, to allow the beam profiler to examine different points along the converging beam. For all tests, a HeNe laser at 633 nm wavelength was used with a beam expander to illuminate the entire MLA.

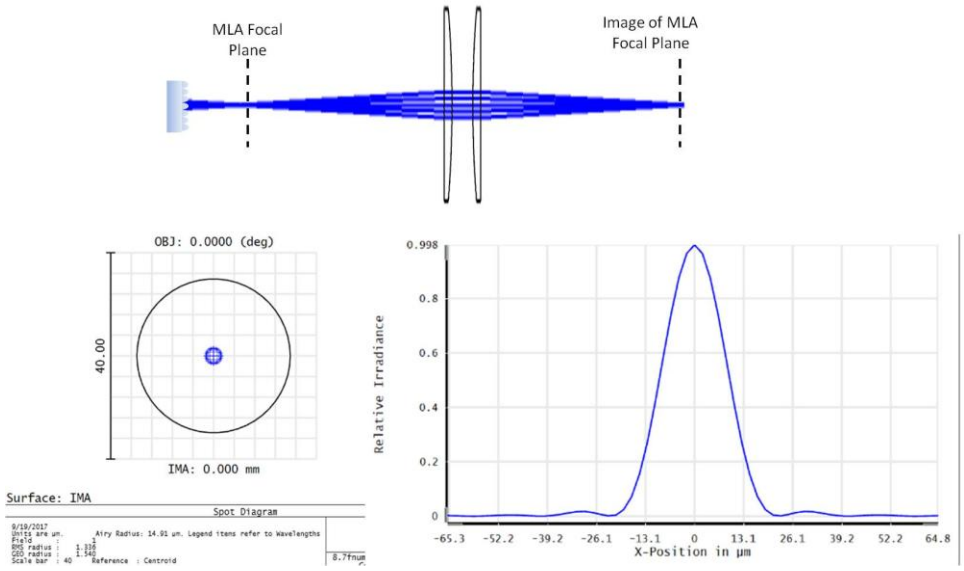


Figure 41: Example of results from Zemax simulations to optimize the testing distances with the MLA focal point imaging setup. The image on the top is a ray trace through the designed system. The image in the bottom left is a spot diagram of the beam at the detector, and the image in the bottom right is a cross-sectional slice of the beam profile at the detector.

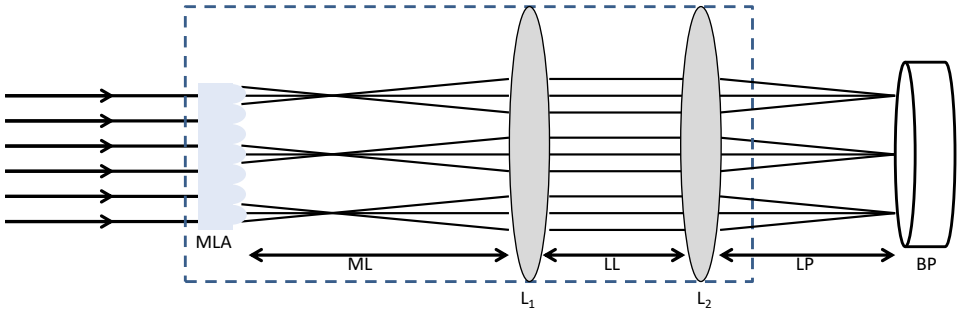


Figure 42: Diagram showing the optical test setup for investigating the beam profiles of the MLA at focus and through focus. Distance ML was roughly the sum of the MLA focal length and the focal length of $L_1$, and then further optimized in Zemax for proper collimation after $L_1$. The distance LL was determined by physical constraints on the optical system in the lab such as how much throw distance was needed in the lens tubes. Distance LP was roughly the focal length of $L_2$ but further optimized in Zemax. For the distance measurements for each MLA, see Table 6. The dashed box shown indicates the movable assembly that could be translated along the optic axis, in order to investigate the beam profile through focus.

Table 6: Distances shown in Fig. 42 for each MLA for measurements taken at focus. As the beam profile was observed through focus, the LP value would decrease.

| MLA | MLA focal length | ML | LL | LP |
|---|---|---|---|---|
| A | 4.8 mm | 105 mm | 30 mm | 88 mm |
| B | 8.7 mm | 110 mm | 25 mm | 96 mm |
| C | 18.8 mm | 115 mm | 20 mm | 90 mm |

Figure 43 shows the beam profiles of the each of the MLAs at focus. In each plot, the rARSS processed MLA is compared to the same unprocessed MLA, as well as, to the simulated beam profile from Zemax. For all aspect ratios, the width of the central peak and the first nulls on either side of the central peak are in good agreement for the rARSS, the unprocessed, and the simulated MLA. The simulations do not have the raised side lobes seen in the measured data because the simulations were of a single, apertured

microlens, while the measured data is of an unapertured microlens array as seen in Fig. 45. The lack of a hard aperture on the microlenses and the light contributed from neighboring microlenses leads to the raised side lobes in Fig. 43. To quantitatively confirm this, Fig. 44 shows the distance between the first nulls of the central peak of the beam profile for the Zemax simulations, the unprocessed, and the rARSS processed MLAs. Figure 44 shows that for all MLAs the measured values of both the unprocessed and rARSS processed MLAs agree, indicating that the spot size at focus does not change with the application of the rARSS.

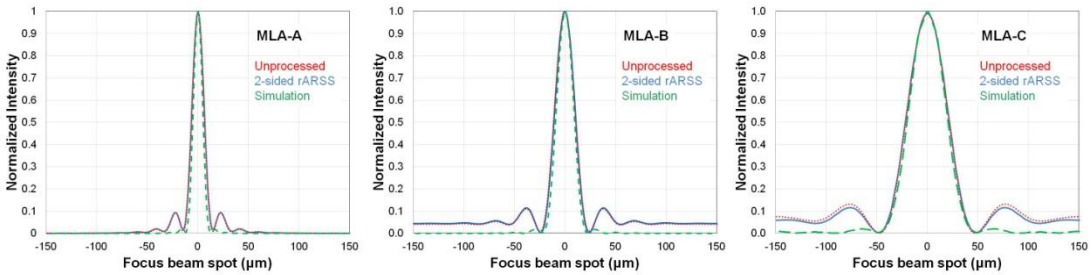


Figure 43: Beam profiles of focal point spots, comparing rARSS processed MLAs, with unprocessed MLAs, and with simulations of each MLA. The MLA sample identifier is indicated in the top right corner of each plot, and in all cases the red dotted line is the unprocessed MLA, the solid blue line is the 2-side processed rARSS MLA, and the dashed green line is the MLA simulation.

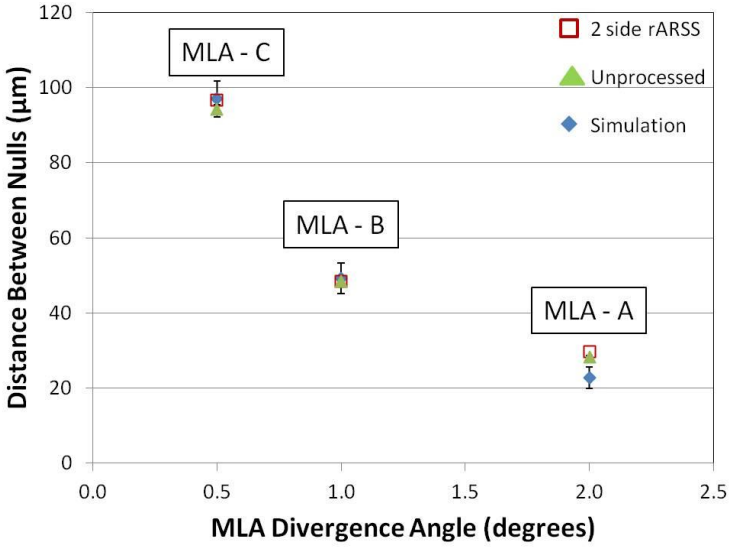


Figure 44: Plot comparing the distance between the first nulls of the central peak of the focal point spot for all three MLAs. Each MLA is marked and the blue diamonds are the Zemax simulation values, the open red squares are the 2 side rARSS processed MLA values, and the green triangles are the unprocessed MLA values. Error bars shown indicate the uncertainty caused by the resolution of each measurement or simulation, and if error bars are not seen then they are smaller than the marker.

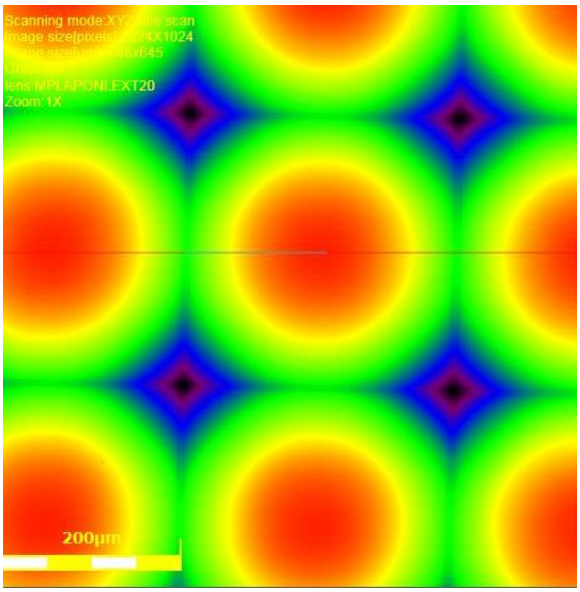


Figure 45: Top down UV laser confocal microscope image of unprocessed MLA-C showing the arrangement of the lenses in the array. The periodicity measured is 300 µm.

### 3.3.2 Microlens Array Beam Propagation Tests

After the focal point was investigated, the movable assembly shown in Fig. 42 was utilized to investigate the beam propagation after each MLA, through focus. The Rayleigh range ($z_R$) of each MLA was calculated, and the measurements through focus were taken at focus (0.0 $z_R$), 0.25 $z_R$, 0.5 $z_R$, 1.0 $z_R$, 2.0 $z_R$, 4.0 $z_R$, and 7.0 $z_R$ (6.0 $z_R$ for MLA-C because the setup could not accommodate the longer distance required to reach 7.0 $z_R$ for the longest focal length MLA). These measurements can be found in Fig. 46, with the unprocessed MLAs in the left column and the rARSS processed MLAs in the right column. The sample name for each plot can be found in the upper right hand corner and the Rayleigh range value is shown next to each profile. Figure 47 compares the full width at half maximum (FWHM) between the unfocused and rARSS processed MLAs from focus to 0.5 $z_R$ to help to quantify the differences the application of rARSS causes. It also includes dashed lines indicating how the calculated Gaussian beam profile changes with distance from the beam waist, from the equation $2w(z) = 2w_0\sqrt{1 + \left(\frac{z}{z_R}\right)^2}$ where $2w(z)$ is the beam diameter at distance $z$ from focus, $2w_0$ is the beam waist diameter, and $z_R$ is the Rayleigh range. FWHM measurements were not able to be taken beyond 0.5 $z_R$ because at that point most of the MLAs' beam profiles were no longer resembling a Gaussian due to contributions from neighboring microlenses. For MLA-A, which has the shortest effective focal length and thus, the steepest lenses of the three samples, there is not a noticeable difference between the processed and unprocessed MLAs for any of the locations through focus that were examined in Fig. 46. The FWHM measurements in Fig. 47 agree with this, as the processed and unprocessed values are identical and follow the

calculated Gaussian beam diameter values. For MLA-B, the sample with both the middle effective focal length and aspect ratio, the unprocessed and rARSS processed MLAs again look very similar in Fig. 46. There is a slight difference in the shape of the side lobes between the processed and unprocessed samples at 7.0 Rayleigh ranges and a slight difference in the central valley at 4.0 Rayleigh ranges, but up until that point the profiles look very similar. Again, Fig. 47 confirms this assessment, showing that while the FWHM of MLA-B is slightly different with and without etching away from focus, this difference is very small. Finally, for sample MLA-C, in Fig. 46 the unprocessed and rARSS MLA profiles again match very well at 0.0 $z_R$, 0.25 $z_R$, 0.5 $z_R$, 1.0 $z_R$, and 6.0 $z_R$. At 2.0 $z_R$ and 4.0 $z_R$ there are some differences between U-C and AR-C, namely a difference in the center peak of the beam profile at 2.0 $z_R$ and a slight waviness in the profile of U-C at 4.0 $z_R$ that is not seen in the AR-C sample. It is interesting that it is the sample with the longest focal length, MLA-C that shows the most variation between unprocessed and processed samples, since it is the array that is closest to a planar substrate. This is most likely because as the array with the longest Rayleigh range, it has the most distance between measurement points, and thus, the most contribution from neighboring microlenses. All three MLAs in Fig. 46 showed minimal changes to their beam profiles for a minimum period of from focus to 1 Rayleigh range with the application of the rARSS.

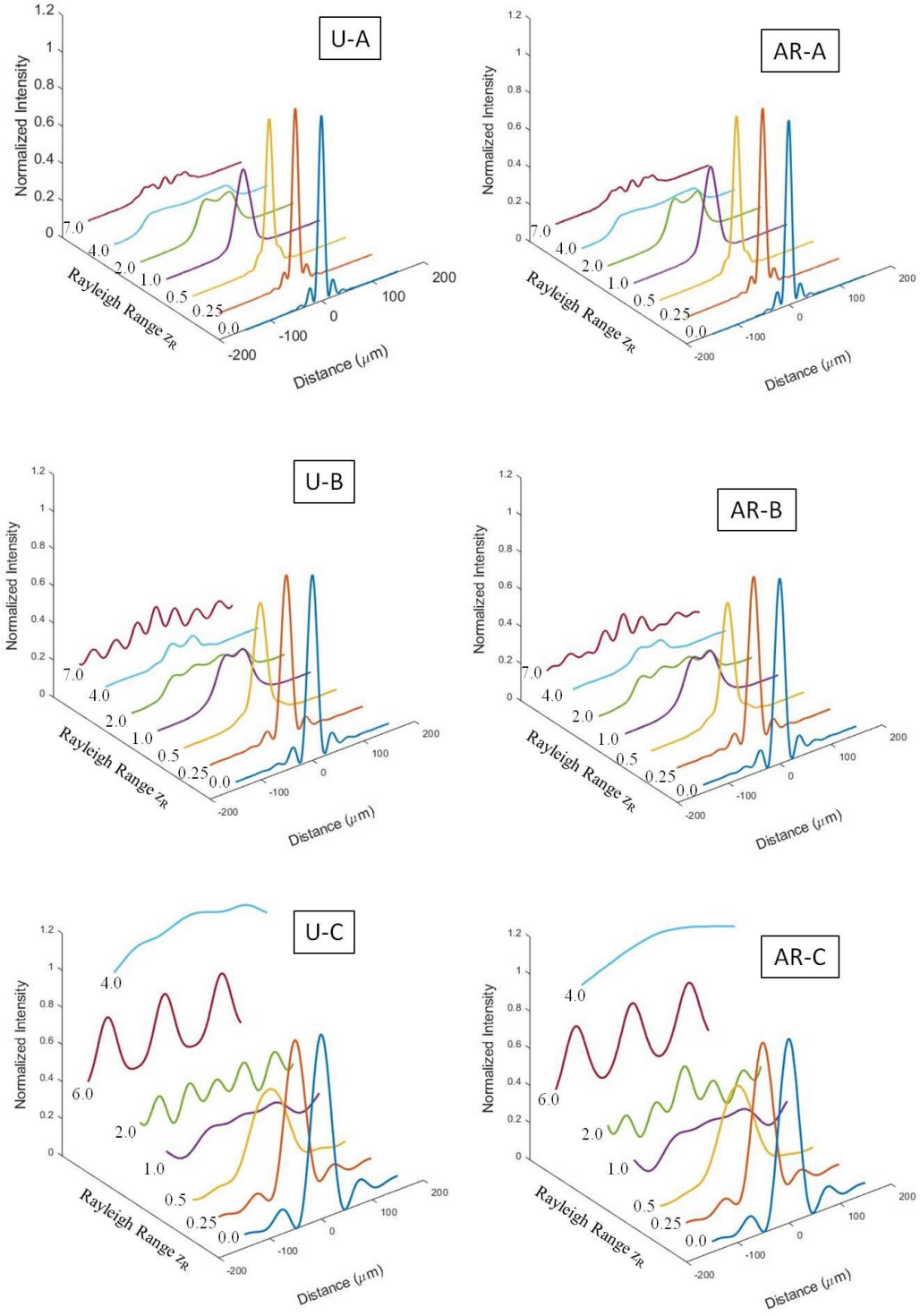


Figure 46: Beam profiles of unprocessed (left column) and rARSS processed (right column) MLAs from focus through 7 Rayleigh ranges (6 Rayleigh ranges for MLA-C).

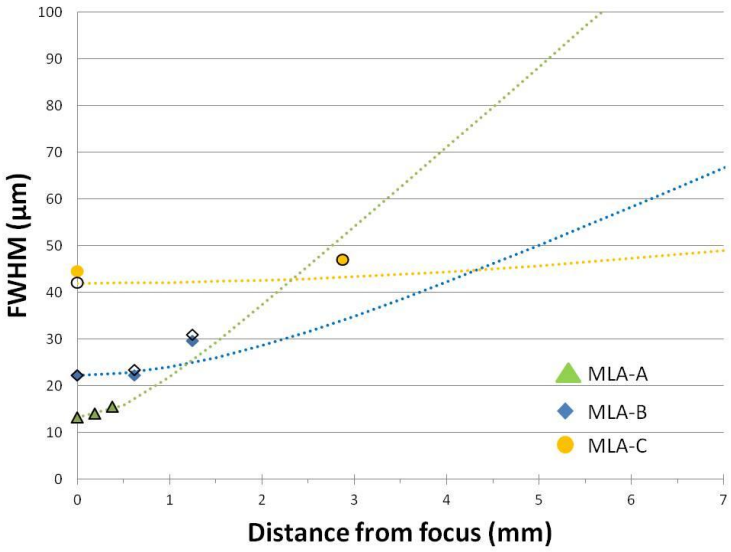


Figure 47: Plot comparing the full width at half maximum (FWHM) of all three MLAs (processed vs unprocessed) at focus, at 0.25 $z_R$, and 0.5 $z_R$. Green triangles are MLA-A, blue diamonds are MLA-B, and yellow circles are MLA-C. In all cases the colored shape represents the 2 side rARSS processed MLA value, while the black outline of the corresponding shape represents the unprocessed MLA value.

### 3.3.3 Microlens Array Transmission Enhancement Tests

The same setup shown in Figs. 41 and 42 was used to test the transmission enhancement of the rARSS on the three MLAs, with the beam profiler replaced by a photodiode power sensor and power meter from Thorlabs. The measurements were conducted with the movable assembly positioned such that the power sensor was investigating an area of the beam that was out of focus, and an aperture was placed on the front of the power sensor to reduce stray light. Planar fused silica samples, both an unprocessed sample and a 2-side rARSS sample that was processed at the same time as the MLAs were tested along with the rARSS and unprocessed MLA samples.

Transmission measurements were the average of 500 data points, one taken each second, and were calculated by dividing the measured power with the MLA or planar substrate in position by the measured power without a substrate. The transmission enhancement was calculated using the relation shown in equation 1 and is displayed in Fig. 48. The figure shows that the transmission enhancement abilities of the rARSS processed MLAs are comparable to or better than the 2 side rARSS processed FS sample, which means that the curved nature of the MLA substrates does not negatively impact the rARSS ability to reduce reflection.

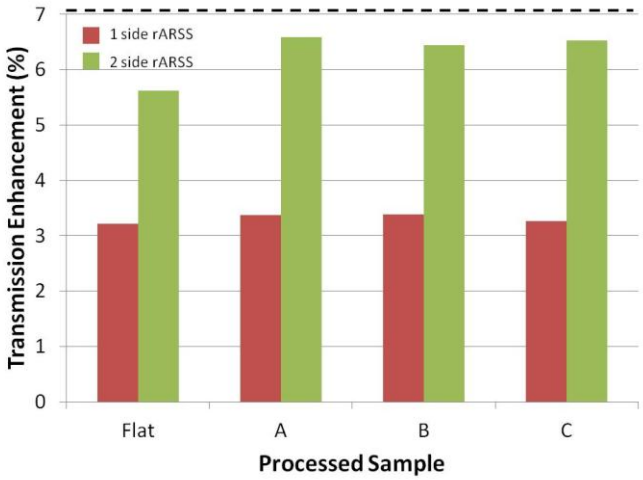


Figure 48: Measured transmission enhancement in percent, for a FS flat substrate and the three rARSS processed MLAs. The red columns were measured after processing only the curved side of the MLAs and only one side of the FS flat substrate. The green column was measured after the second side of all substrates was processed. All measurements were taken with an expanded HeNe laser at 633 nm. The black dashed line is the maximum possible transmission enhancement for double side processed fused silica, 7.2%.

## 3.4 Investigating the Far-Field Diffraction of Microlens Arrays with rARSS

### 3.4.1 Experimental Setup and Analysis

In order to test the effect of rARSS on the phase of the wavefront, a system was devised to compare the far-field diffraction of a rARSS processed and unprocessed MLA. Figure 49 shows the experimental setup, in which the MLA is placed at the front focal plane of a positive lens (L, with a focal length of 50 mm). The detector, the same scanning slit beam profiler used in section 3.3, is then placed at the back focal plane of L. This experimental layout allows for the investigation of the far-field diffraction pattern of the MLA, as the following analysis shows.

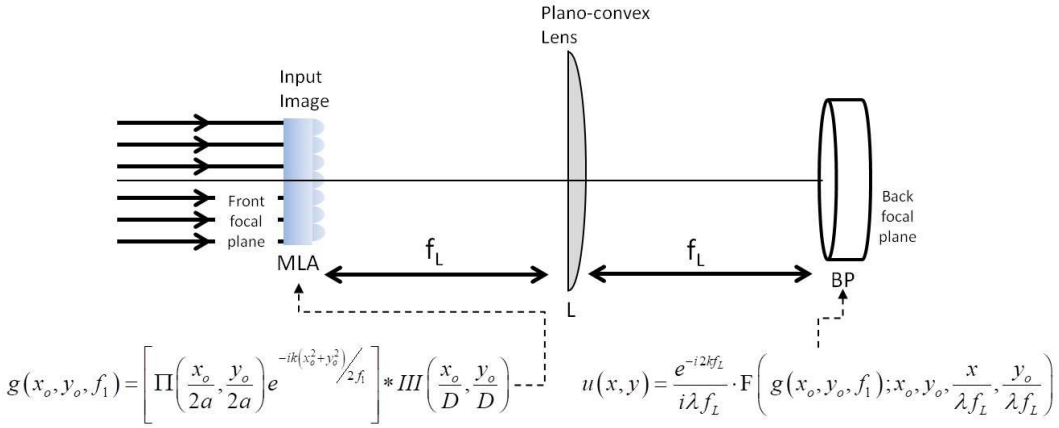


Figure 49: Diagram showing the optical setup for investigating the far-field diffraction pattern of the MLA where the MLA is placed at the front focal plane of the Fourier transforming lens, L. In this setup, L was placed one focal length away ($f_L$ = 50 mm) from the scanning slit beam profiler, BP. The MLA was then placed one focal length in front of the Fourier transforming lens.

First, it was important to determine if the propagation distances for this layout were in the Fresnel or Fraunhofer region, for both the MLA and the transforming lens L. The distance to the Fraunhofer region is determined by:

$$Z_i = \frac{D^2}{\lambda} \tag{6}$$

where λ = 633 nm, $D_{MLA}$ = 300 μm, and $D_L$ = 25.4 mm. The distance to the Fraunhofer region for the MLA was 142 mm and for L was 1.02 x $10^6$ mm and since both actual propagation distances were 50mm, it was determined that the whole system was in the Fresnel (near-field diffraction) region.

If $g(x, y, f_l)$ is the MLA aperture function at the input of the system, then first it must be Fresnel propagated through free space to the surface of the lens using:

$$g'(x, y, f_L, f_\ell) = g(x, y, f_\ell) * \left[\frac{1}{i\lambda f_L} e^{\left(ik\left(f_L + \frac{x^2+y^2}{2f_L}\right)\right)}\right] = g(x, y, f_\ell) * p(x, y, f_L) \tag{7}$$

Where $f_l$ is the MLA individual lens focal distance, and $p(x, y, f_L)$ is the point-source transfer function over a longitudinal distance $f_L$. Once the light is behind L, the wavefront function becomes:

$$g'(\mathrm{x}, \mathrm{y}, f_L, f_\ell)\mathrm{e}^{\left(-ik\left(\frac{x^2+y^2}{2f_L}\right)\right)} \tag{8}$$

Where the Fresnel propagated MLA function is multiplied by the lens phase from L. Propagating this to the beam profiler, gives:

$$u(x, y, f_L, f_\ell) = \frac{1}{i\lambda f_L} e^{\left(ik\left(f_L + \frac{x^2+y^2}{2f_L}\right)\right)} F\left\{g'(x', y', f_L, f_\ell); x', y', \frac{x}{\lambda f_L}, \frac{y}{\lambda f_L}\right\} \tag{9}$$

Where the $F\{g\}$ indicates the Fourier Transform by the lens on the incoming MLA wavefront, and by substitution of equation 7 into equation 9, we have:

$$u(x,y,f_L,f_\ell)=\frac{1}{i\lambda f_L}e^{\left(ik\left(f_L+\frac{x^2+y^2}{2f_L}\right)\right)}F\left\{g(x',y',f_\ell)*p(x',y',f_L);x',y',\frac{x}{\lambda f_L},\frac{y}{\lambda f_L}\right\} \quad (10)$$

Using the convolution theorem, equation 10 will become

$$u(x,y,f_L,f_\ell)=\frac{1}{i\lambda f_L}e^{\left(ik\left(f_L+\frac{x^2+y^2}{2f_L}\right)\right)}G\left(\frac{x}{\lambda f_L},\frac{y}{\lambda f_L}\right) \quad (11)$$

Where $G\left(\frac{x}{\lambda f_L},\frac{y}{\lambda f_L}\right)$ is the Fourier transform of the MLA. The intensity detected by the scanning aperture is:

$$I(x,y,f_L,f_\ell)=\left(\frac{1}{\lambda f_L}\right)^2\left|G\left(\frac{x}{\lambda f_L},\frac{y}{\lambda f_L}\right)\right|^2 \quad (12)$$

Equation 12 is the exact far-field diffraction intensity of the input $g(x,y,f_\ell)$. Therefore, the optical system in Figure 49 allows for the measurement of the Fraunhofer-range diffraction intensity of the MLA. The MLA input function is expressed as:

$$g(\mathrm{x},\mathrm{y},f_\ell)=\mathrm{III}\left(\frac{x}{D},\frac{y}{D}\right)*\prod\left(\frac{x}{D},\frac{y}{D}\right)\cdot e^{-i\pi(x^2+y^2)/(\lambda f_\ell)} \quad (13)$$

Where the comb-function *III(x,y)* is the array (replicating) factor, the 2-dimensional aperture of each microlens is *Π(x,y)*, and the array separation distance *D* is 300 μm. The test wavelength is 633 nm, and the last term in equation 13 is the phase imparted by each microlens. Proceeding with the Fourier transform of equation 13 and using the convolution-product properties of the transformation we have:

$$G\left(\frac{x}{\lambda f_L},\frac{y}{\lambda f_L}\right)=\mathrm{F}\left\{\mathrm{III}\left(\frac{x}{D},\frac{y}{D}\right);x',y',\frac{x}{\lambda f_L},\frac{y}{\lambda f_L}\right\}\mathrm{F}\left\{\prod\left(\frac{x}{D},\frac{y}{D}\right)\cdot e^{-i\pi(x^2+y^2)/(\lambda f_\ell)};x',y',\frac{x}{\lambda f_L},\frac{y}{\lambda f_L}\right\} \quad (14)$$

Thus separating the transform of the array factor from the transform of a single isolated microlens. The first term in equation 14 yields another comb function, whereas the second term can be expressed as Fresnel Sine and Cosine Integrals as shown in Appendix C.

### 3.4.2 Fourier Transform Results and Analysis

The data collected with the MLAs placed at the front focal plane of a Fourier transform lens is shown in this section. The normalized intensity plots in Fig. 50 show the unprocessed (red) and 2 side rARSS processed (blue) profiles for all three MLAs, and while it does not appear that the rARSS application changes the overall envelope size, there are clearly some differences in the height of individual peaks throughout the profiles. The analytical solution using the result of equation 12, for a single microlens profile without the array *III(x,y)* term in equation 13, is shown as a green curve. The details of the result, involving the Fresnel Sine and Cosine Integrals *C(x,y)* and *S(x,y)*, is included in Appendix C.

The separation between the diffraction peaks, due to the contribution of the array's transform, is constant at 105 μm for all MLAs and for both rARSS processed and unprocessed samples. This is because the spacing of the peaks in the Fourier transform of the MLA comes from the spacing of the lenses on the MLA. Since this was constant for all MLAs (300 μm) and is unchanged with the rARSS fabrication process, it results in the consistent peak separation seen in Fig. 50. To confirm that the 105 μm corresponds to the periodicity, we have $\Lambda_0 = 300\mu m$ is the period of the MLA, and then the comb function for the MLA can be expressed as

$$III\left(\frac{x_0}{\Lambda_0}\right) = \sum_{m=-\infty}^{\infty} \delta(x_0 - m\Lambda_0) \tag{14}$$

The Fourier transform of this comb function is then

$$F\left\{III\left(\frac{x_0}{\Lambda_0}\right)\right\} = \Lambda_0 III\left(\frac{\Lambda_0 x_i}{\lambda f_L}\right) \tag{15}$$

which can be expressed as:

$$III\left(\frac{\Lambda_0 x_i}{\lambda f_L}\right) = \sum_{m=-\infty}^{\infty} \delta\left(\frac{x_i}{\lambda f_L} - \frac{m}{\Lambda_0}\right) = \sum_{m=-\infty}^{\infty} \delta\left(\frac{\Lambda_0 x_i}{\lambda f_L} - m\right) \quad (16)$$

which will become 1 when $\frac{\Lambda_0 x_i}{\lambda f_L} - m = 0$. Looking at the case where $m = 1$, $\lambda = 633nm$, $f_L = 50\ mm$ and solving for $x_i$ gives a spacing between peaks value of 105.5 μm. Since the resolution of the measurement is 1.18 μm/pixel, these values are in good agreement.

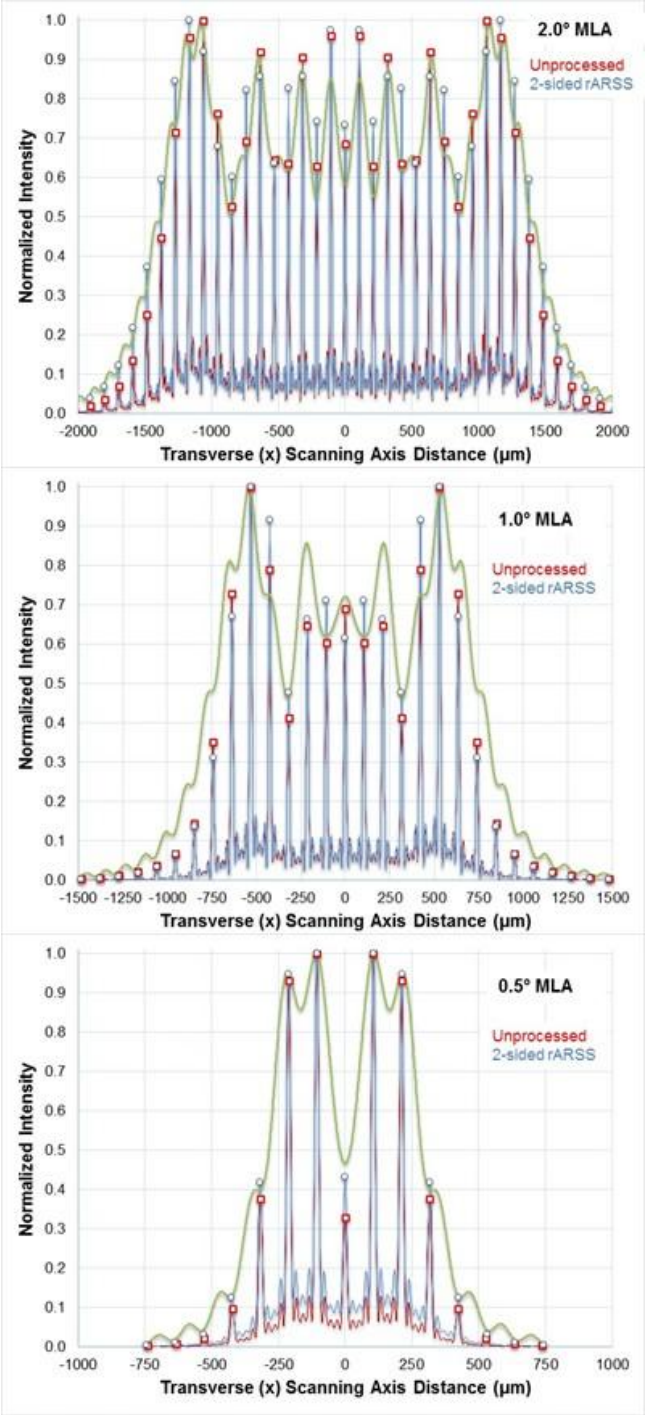


Figure 50: Normalized intensity plots for all three MLAs when they are placed at the front focal plane of a Fourier transform lens. In all plots the unprocessed MLA profile is shown in red and the 2 sided rARSS processed MLA data is shown in blue. The green curve is the analytical far-field diffraction result of a single microlens. The separation between the diffraction order peaks is 105 µm.

In order to see more detail about the profiles and to better compare the rARSS processed MLAs to the unprocessed MLAs, the analytical envelopes of the profiles shown in Fig. 50, and the individual diffraction peaks were plotted in Fig. 51, again with the unprocessed samples in red and the rARSS processed samples in blue. The analytical envelopes help to accentuate the differences in height of the individual peaks, between the unprocessed and rARSS processed samples, and show that for all three MLAs there are slight differences in the far-field diffraction pattern. It is interesting to note that of all of the MLAs, MLA-C (0.5°) shows the best agreement between the unprocessed and the rARSS diffraction peak intensities throughout the entire range of spatial frequencies; the other MLAs show larger differences in intensity between unprocessed and rARSS processed samples.

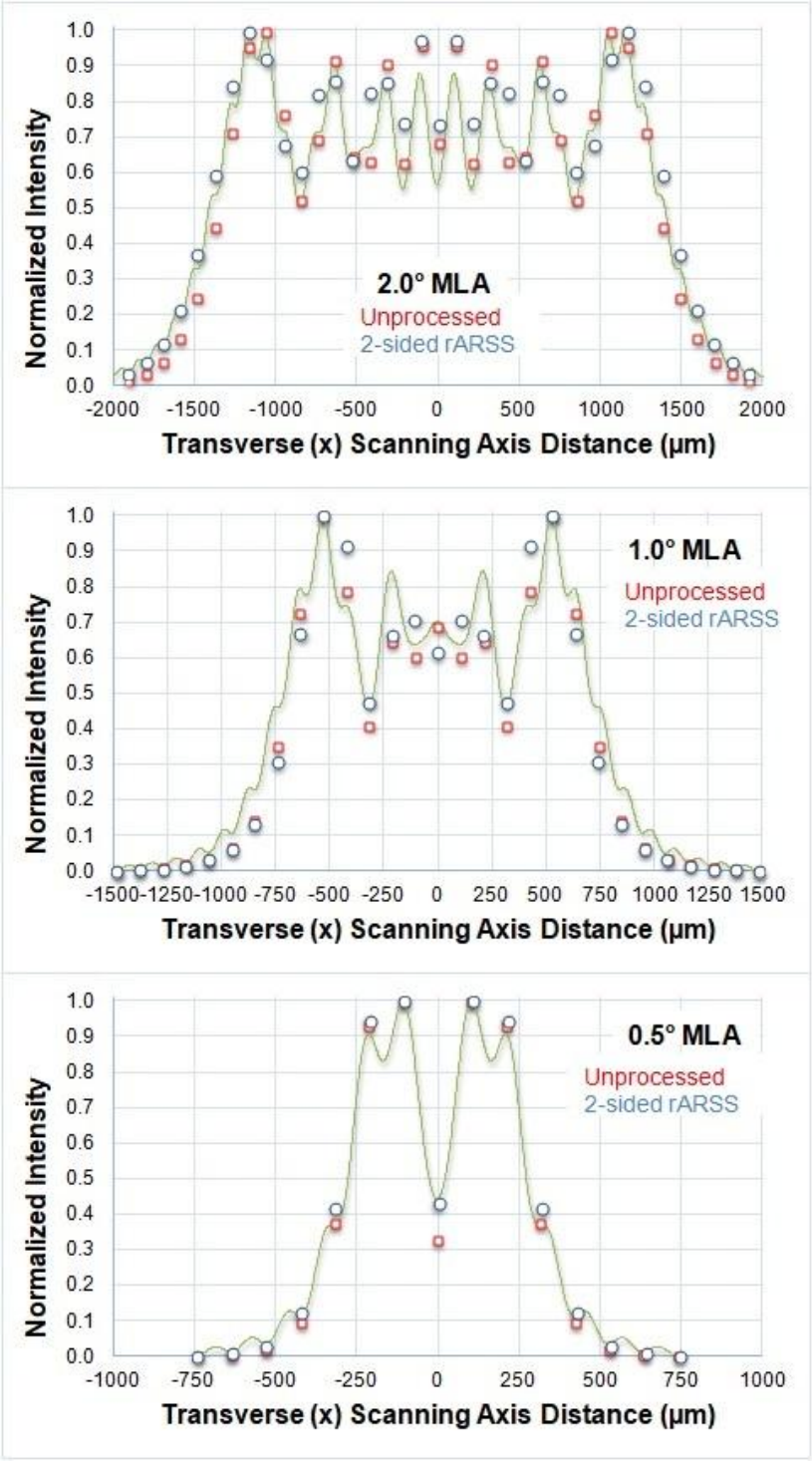


Figure 51: Normalized intensity plots of the analytical envelopes of the profiles shown in Fig. 50 for each MLA. The unprocessed data is shown in red and the two- side rARSS processed data is shown in blue. The green curve is the analytic result for a single microlens.

In order to get a better look at how the unprocessed and rARSS processed MLA results differed on the limits of the far-field diffraction patterns, the same envelopes that were shown in Fig. 51 were plotted on a logarithmic scale in Fig. 52. This shows that MLA-B (1.0°) seems to be the most unaffected by the rARSS on the high-spatial frequency range. MLA-A (2.0°) shows the most difference between the unprocessed and rARSS processed samples on the limits of the envelopes in these logarithmic plots. In all cases though, the differences caused by the application of the rARSS are slight, but measurable.

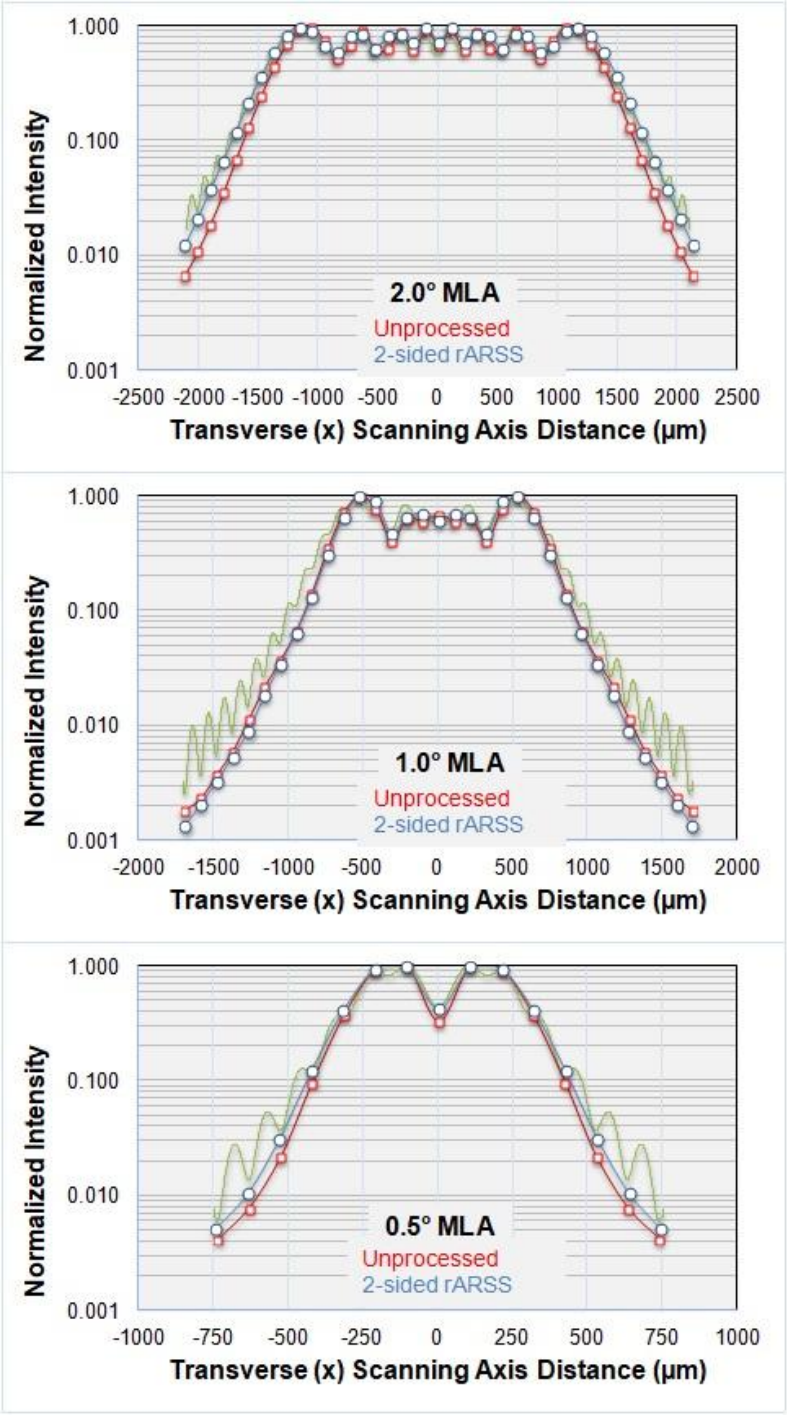


Figure 52: Normalized intensity plots of the envelopes of the profiles shown in Fig. 50 for each MLA shown on a logarithmic plot to accentuate differences between the unprocessed and 2 side rARSS processed samples on the limits of the envelopes. The unprocessed data is shown in red and the 2-side rARSS processed data is shown in blue. The green curve is the analytic result for a single microlens.

## 3.5 Summary of Microlens Array Optical Performance Chapter

This chapter presented results from an attempt to use a rARSS fabrication process designed for planar FS flats on 3 different FS MLAs with different aspect ratios. Section 3.1 reviewed the current literature for the application of both random and periodic ARSS onto MLAs, and attempted to evaluate the gaps in the testing methods used so far. It was shown that most of the work in the literature focused on transmission and reflection spectra of processed MLAs, and the work that did attempt to look at the beam propagation properties of the processed MLAs was not fully addressing beam propagation and wavefront effects.

Section 3.2 outlined the fabrication process for producing rARSS onto the MLAs, and attempted to characterize the physical properties of the random structures on the MLA surface. Granulometry was conducted on scanning electron microscope images of different locations on MLA-A (2.0°) and MLA-C (0.5°) and it was shown that there is neither a large difference in feature size between MLAs of different aspect ratio, nor between different points along the same MLA.

Section 3.3 presented results to evaluate beam propagation and wavefront effects through the MLAs. Zemax simulations and experimental results from tests of the focal points of the processed and unprocessed MLAs, as well as their beam profiles from focus through to further Rayleigh ranges were presented. Transmission enhancement values were also measured for single and double side processed MLAs as well as flat FS substrates. Qualitatively it was shown that there are small deviations in the beam profile shape from focus to around one Rayleigh range, and that beyond one Rayleigh range the

differences are mostly seen in the longer focal length MLAs. Quantitatively, measurements of the spot size (defined as the distance between the first nulls of the central peak) at focus and the FWHM from focus to 0.5 Rayleigh ranges agreed with this assessment. At focus it was shown that the processed and unprocessed MLAs had excellent agreement, and through focus it was shown that the longer effective focal length MLAs had more deviation in the FWHM away from focus than the shorter effective focal length MLAs. This was likely caused by a larger contribution from neighboring microlenses with the larger distances investigated for the longer effective focal length MLA. Transmission enhancement tests conducted at 633 nm showed that the processed MLAs were performing just as well or better than rARSS processed FS flat.

Section 3.4 investigated how the rARSS affected the phase of the wavefront through the MLA by looking at the Fourier transform of the MLA. The Fourier transform was investigated by placing the MLA at the front focal plane of a positive lens, and the beam profiler at the back focal plane of the same lens. It was shown that while there are some measurable differences between the rARSS and unprocessed results, they are very small and don't have adverse effects on the performance of the microlenses.

The results presented in this chapter show that a rARSS fabrication process designed for flat substrates is transferrable to MLAs without adversely affecting the transmission enhancement, the beam propagation, or the phase properties of the MLAs.

# CHAPTER 4: CONCLUSIONS

## 4.1 Summary of the Optical Performance of Random Antireflection Structured Surfaces on Planar Substrates

In this work, random antireflection structured surfaces were fabricated on planar fused silica substrates using the pre-masking method of fabrication. The samples were tested at three different steps in the fabrication process: after metallization, after rapid thermal annealing (RTA), and after reactive ion etching (RIE), in order to understand how the mask parameters would influence the final fused silica structure parameters. This three-step method was designed to observe if masking control processes, such as rapid thermal annealing, could outperform methods that used a discontinuous metal layer as a mask with no thermal annealing.

Surface depth and roughness measurements, as well as measurements of the statistical distribution of the lateral feature sizes were collected after the RTA step and again after the RIE step. From these measurements it was shown that a mask with taller gold islands would result in a thinner effective medium in the fused silica after RIE. Transmission spectra taken of the rARSS samples showed that this reduction of the effective medium thickness results in a decrease in transmission enhancement at longer wavelengths.

Granulometry measurements showed that as the size of the voids in the mask increased, the size of the voids would increase on the fused silica up to an RTA temperature of 600 ˚C. At RTA temperatures of 600 ˚C and up, both large and small void populations would be present in the final surface profile. The large voids found on the

samples with the highest RTA temperatures resulted in increased scatter at the short wavelengths (from 300-1300 nm). It was also noted that, while increasing the annealing temperature would result in an increase in the void coverage across a mask sample, the coverage after RIE remained around 50% for all samples, indicating that the mask parameters did not influence this variable for the fused silica samples.

The transmittance tests showed that the RTA samples could not outperform the transmission enhancement of the sample that was not thermally annealed. This led to the conclusion that the RTA step in the fabrication process was not necessary, and therefore it was not used throughout the rest of the body of work. For the non-annealed sample, the Fresnel reflectance suppression was of the order of 70%, with a maximum specular beam transmission enhancement of 3.4% and transmission enhancement values above 1.5% from 350 nm to 2120 nm. The AR effect measured is comparable or better than commercially available conventional AR thin-film multilayered coatings.

Following the process parameter guidance from the rARSS fabrication on FS flat substrates, fabrication of rARSS was attempted on a polycrystalline material: spinel. Initial characterization results showed that crystals of different orientation would etch differently, inducing increased scatter and decreased specular transmission through the substrate surfaces. In order to try to create a uniform surface on the substrate and avoid the issues with micro-crystal orientations and boundaries, a layer of $SiO_2$ was deposited on the spinel substrates using the PECVD. The $SiO_2$ layer was then sputtered with Au and etched, attempting to roughen the silica, however no roughness was produced on the spinel substrates after a series of trials.

A new process was designed and developed, in which an index matching material and a sacrificial material were co-deposited on the surface of the spinel substrates, and then the sacrificial material was removed through etching. Three different deposition-process strata recipes were tried, resulting in three different layered structures of index-matching/intermix/sacrificial layers, with transmission and roughness measurements taken after multiple short etch steps in all cases. It was found that for each separate deposition-process stratum the transmission was increased at specific steps in the etching process, but with two of the depositions the sacrificial material remained trapped in the deposited layer and was unable to be etched away completely. SEM and confocal microscope measurements showed that the surfaces of the spinel samples were not roughening, which indicates that the increased transmission was likely caused by effective medium effects in the intermix region, rather than by subwavelength structures on the surfaces.

The work shown for flat fused silica and polycrystalline substrates has resulted in an understanding of how to consistently produce fused silica rARSS, and has shown that the rapid thermal annealing step commonly found in the literature is not entirely beneficial to the final reflection suppression outcome. The work has also shown that the fused silica fabrication process is not transferrable to polycrystalline materials, but that using an index matching and sacrificial layer deposition process can give certain transmission benefits.

## 4.2 Summary of the Optical Performance of Random Antireflection Structured Surfaces on Microlens Arrays

In order to test if the fabrication method for rARSS on fused silica flats could be transferred to silica substrates with surface topography, three different microlens arrays (MLAs) were processed with the previously described optimal method. The MLAs all had the same period and lens size, but different focal lengths, leading to different aspect ratios for each MLA, and therefore different topographic variation. SEM images and granulometry measurements taken from each MLA set, as well as at different locations on each MLA, showed that the surface topography did not result in variations in the physical random nano-feature statistical distributions. Power measurements taken of all three processed MLAs, and a witness flat processed alongside the MLAs, showed that both one and two side processed MLAs performed as well or better than the processed flat, with respect to Fresnel reflection suppression and specular transmittance. This result showed that the surface topography had no negative overall effect on the transmission enhancing properties of the rARSS.

Next, the optical performance of the rARSS processed MLAs was tested with three different experiments, to determine if there were any measurable perturbations on the transmitted wavefront. First, a beam profiler was used to compare the focal spot size of the processed and unprocessed MLAs to simulated sets, and it was shown that the rARSS did not affect the focal spot size or location along the optic axis. Next, beam profile measurements from focus through multiple Rayleigh ranges showed that the rARSS had no effect on the shape of the beam profile, from focus through one Rayleigh range, and beyond that there were only subtle differences observed.

A test was developed to characterize the phase-sensitive far-field diffraction response to the presence of the rARSS. The MLA was placed at the front focal plane of a focusing lens, and the beam profiler was placed at the back focal plane which allowed the beam profiler to investigate the Fourier transform of the MLA. By comparing the peak intensities of the Fourier transforms of the unprocessed and rARSS processed MLAs, and the analytical envelopes of a single microlens, it was determined that there are subtle differences in the diffraction patterns of the MLAs after rARSS fabrication. These differences were in both the low and high spatial-frequency ranges of the diffraction pattern, within the measurement accuracy and sensitivity limits of the measurements. These differences imply that the application of the rARSS to the MLAs is subtly changing the microlens profiles. However, the differences in the unprocessed MLA peak intensities and the analytical solution for a spherical microlens, indicates that the microlenses were not perfectly spherical prior to the rARSS fabrication.

## 4.3 Potential Future Work

The work presented in this dissertation has demonstrated that the application of rARSS to the surface of MLAs increases the specular light transmittance of the devices and does not negatively impact their focusing ability or beam propagation characteristics. Subtle differences in the far-field diffraction patterns of the processed MLAs were observed however. In the future, it would be interesting to develop a non-destructive method for investigating why these differences occur, and why they are different for the various MLAs. For example, the shortest focal length MLA, the $2^{\circ}$ divergence angle,

shows the largest differences between unprocessed and rARSS processed samples at both the high and low spatial frequencies and yet it shows the least change in the beam profile tests. It is also curious that the high spatial frequencies of both the 2.0° and the 0.5° MLAs seem to match the analytical result better after the application of the rARSS, but for the 1.0° MLA there is very little change. To investigate how these changes relate to the physical profile of the microlenses, a system would need to be built that could interferometrically investigate individual microlens arrays. This could provide interesting insights into how the rARSS can cause measurable changes to the diffraction patterns of the MLAs without negatively impacting their focusing and beam propagation abilities.

# REFERENCES


[1] T. Aytug, A. R. Lupini, G. E. Jellison, P. C. Joshi, I. H. Ivanov, T. Liu, *et al.*, "Monolithic graded-refractive-index glass-based antireflective coatings: broadband/omnidirectional light harvesting and self-cleaning characteristics," *J. Mater. Chem C,* vol. 3, pp. 5440-5449, 2015.

[2] S. Chattopadhyay, Y. F. Huang, Y. J. Jen, A. Ganguly, K. H. Chen, and L. C. Chen, "Anti-reflecting and photonic nanostructures," *Materials Science and Engineering: R: Reports,* vol. 69, pp. 1-35, 2010/06/20/ 2010.

[3] A. Thelen, *Design of Optical Interference Coatings*. New York: McGraw-Hill Book Company, 1989.

[4] U. Schulz, F. Rickelt, H. Ludwig, P. Munzert, and N. Kaiser, "Gradient index antireflection coatings on glass containing plasma-etched organic layers," *Optical Materials Express,* vol. 5, pp. 1259-1265, 2015/06/01.

[5] D. H. Raguin and G. M. Morris, "Antireflection structured surfaces for the infrared spectral region," *Applied Optics,* vol. 32, pp. 1154-1167, 1993/03/01 1993.

[6] D. H. Raguin and G. M. Morris, "Analysis of antireflection-structured surfaces with continuous one-dimensional surface profiles," *Applied Optics,* vol. 32, pp. 2582-2598, 1993/05/10.

[7] E. B. Grann, M. G. Moharam, and D. A. Pommet, "Optimal design for antireflective tapered two-dimensional subwavelength grating structures," *Journal of the Optical Society of America A,* vol. 12, pp. 333-339, 1995/02/01.

[8] T. K. Gaylord, W. E. Baird, and M. G. Moharam, "Zero-reflectivity high spatial-frequency rectangular-groove dielectric surface-relief gratings," *Applied Optics,* vol. 25, pp. 4562-4567, 1986/12/15 1986.

[9] Y. Kanamori, M. Sasaki, and K. Hane, "Broadband antireflection gratings fabricated upon silicon substrates," *Optics Letters,* vol. 24, pp. 1422-1424, 1999/10/15.

[10] D. S. Hobbs and B. D. MacLeod, "Design, Fabrication, and Measured Performance of Anti-Reflecting Surface Textures in Infrared Transmitting Materials," *Proceedings of SPIE,* vol. 5786, May 18, 2005.

[11] P. Lalanne and G. M. Morris, "Design, fabrication, and characterization of subwavelength periodic structures for semiconductor antireflection coating in the visible domain," in *Optical Instrumentation and Systems Design*, 1996, p. 10.

[12] S.-Y. Han, B. K. Paul, and C.-H. Chang, "Nanostructured ZnO as biomimetic anti-reflective coatings on textured silicon using a continuous solution process," *J. Mater. Chem,* vol. 22, pp. 22906-22912, September 11, 2012.

[13] Z.-P. Yang, L. Ci, J. A. Bur, S.-Y. Lin, and P. M. Ajayan, "Experimental observation of an extremely dark material made by a low-density nanotube array," *Nano Letters,* vol. 8, pp. 446-451, 2008/02/01.

[14] J. J. Steele and M. J. Brett, "Nanostructure engineering in porous columnar thin films: recent advances," *Journal of Materials Science: Materials in Electronics,* vol. 18, pp. 367-379, April 01 2007.

[15] B. Zollars, S. Savoy, Q. Xue, J. John, K. Hoover, G. Elpers, *et al.*, "Performance measurements of infrared windows with surface structures providing broadband wide-angle antireflective properties," in *SPIE Defense, Security, and Sensing*, 2013, p. 15.

[16] N. Roxhed, P. Griss, and G. Stemme, "A method for tapered deep reactive ion etching using a modified Bosch process," *Journal of Micromechanics and Microengineering,* vol. 17, p. 1087, 2007.

[17] A. Peltier, G. Sapkota, M. Potter, L. E. Busse, J. A. Frantz, L. B. Shaw, *et al.*, "Control of spectral transmission enhancement properties of random anti-reflecting surface structures fabricated using gold masking," in *SPIE OPTO*, 2017, p. 7.

[18] C. Cardinaud, M.-C. Peignon, and P.-Y. Tessier, "Plasma etching: principles, mechanisms, application to micro- and nano-technologies," *Applied Surface Science*, vol. 164, pp. 72-83, 2000/09/01.
[19] D. J. Economou, "Modeling and simulation of plasma etching reactors for microelectronics," *Thin Solid Films*, vol. 365, pp. 348-367, 2000/04/17.
[20] R. Hsiao and J. Carr, "Si/SiO2 etching in high density SF6/CHF3/O2 plasma," *Materials science and Engineering B*, vol. 52, pp. 63-77, March 6, 1998.
[21] M. Schaepkens and G. S. Oehrlein, "A Review of SiO2 etching studies in inductively coupled fluorocarbon plasmas," *Journal of The Electrochemical Society*, vol. 148, pp. C211-C221, March 1, 2001.
[22] M. Ohring, *The Materials Science of Thin Films*. San Diego, California: Academic Press, 1992.
[23] K. J. L. Company. (2/3/18). *Evaporation Sources*. Available: https://www.lesker.com/newweb/evaporation_sources/evaporation_technicalnotes_1.cfm?pgid=0
[24] O. S. Heavens, *Optical properties of thin solid films*. New York: Dover Publications, 1991.
[25] J. Zhao, H. Qi, H. Wang, H. He, and W. Zhang, "Scattering analysis for random antireflective structures on fused silica in the ultraviolet," *Optics Letters*, vol. 40, pp. 5168-5171, 2015/11/15 2015.
[26] G. Sapkota, J. R. Case, L. E. Busse, J. A. Frantz, L. B. Shaw, J. S. Sanghera, *et al.*, "Characterization of random anti-reflecting surface structures and their polarization response at off-normal angles of incidence," in *SPIE Nanoscience + Engineering*, 2016, p. 8.
[27] Y.-F. Huang, S. Chattopadhyay, Y.-J. Jen, C.-Y. Peng, T.-A. Liu, Y.-K. Hsu, *et al.*, "Improved broadband and quasi-omnidirectional anti-reflection properties with biomimetic silicon nanostructures," *Nature Nanotechnology*, vol. 2, p. 770, 12/02/2007.
[28] G. Sapkota, J. R. Case, M. G. Potter, L. E. Busse, L. B. Shaw, J. S. Sanghera, *et al.*, "Entry and exit facet laser damage of optical windows with random antireflective surface structures," in *SPIE Laser Damage*, 2016, p. 7.
[29] D. S. Hobbs, B. D. MacLeod, and J. R. Riccobono, "Update on the development of high performance anti-reflecting surface relief micro-structures," 2007, pp. 65450Y-65450Y-14.
[30] A. Peltier, G. Sapkota, J. R. Case, and M. K. Poutous, "Polarization insensitive performance of randomly structured antireflecting planar surfaces," *Optical Engineering*, vol. 57, p. 8, 2018.
[31] C. Taylor, K. J. Major, R. Joshi, L. E. Busse, J. Frantz, J. S. Sanghera, *et al.*, "Optical performance of random anti-reflection structures on curved surfaces," 2015, pp. 935916-935916-8.
[32] C. D. Taylor, L. E. Busse, J. Frantz, J. S. Sanghera, I. D. Aggarwal, and M. K. Poutous, "Angle-of-incidence performance of random anti-reflection structures on curved surfaces," *Applied Optics*, vol. 55, pp. 2203-2213, 2016/03/20.
[33] C. D. Taylor, "Optical Performance of Random Anti-Reflection Structured Surfaces (rARSS) on Spherical Lenses," PhD, Department of Physics and Optical Science, The University of North Carolina at Charlotte, 2016.
[34] E. R. Dougherty, *Hands-on morphological image processing*. Bellingham, Wash.: SPIE Optical Engineering Press, 2003.
[35] K. O. Mersereau, C. R. Nijander, A. Y. Feldblum, and W. P. Townsend, "Fabrication and measurement of fused silica microlens arrays," in *San Diego '92*, 1993, p. 5.
[36] P. Nussbaum, R. Völkel, H. P. Herzig, M. Eisner, and S. Haselbeck, "Design, fabrication and testing of microlens arrays for sensors and microsystems," *Pure and Applied Optics: Journal of the European Optical Society Part A*, vol. 6, p. 617, 1997.
[37] S. Biehl, R. Danzebrink, P. Oliveira, and M. A. Aegerter, "Refractive microlens fabrication by ink-jet process," *Journal of Sol-Gel Science and Technology*, vol. 13, pp. 177-182, January 01 1998.
[38] K. Hermans, S. Z. Hamidi, A. B. Spoelstra, C. W. M. Bastiaansen, and D. J. Broer, "Rapid, direct fabrication of antireflection-coated microlens arrays by photoembossing," *Applied Optics*, vol. 47, pp. 6512-6517, 2008/12/10.

[39] Y.-P. Chen, C.-H. Lee, and L. A. Wang, "Fabrication and characterization of multi-scale microlens arrays with anti-reflection and diffusion properties," *Nanotechnology*, vol. 22, p. 215303, 2011.
[40] M. Zimmermann, N. Lindlein, R. Voelkel, and K. J. Weible, "Microlens laser beam homogenizer-From theory to application," *Proceedings of SPIE*, vol. 6663, 2007.
[41] R. Voelkel and K. J. Weible, "Laser beam homogenizing: limitations and constraints," in *Optical Systems Design*, 2008, p. 12.
[42] D.-H. Ko, J. R. Tumbleston, K. J. Henderson, L. E. Euliss, J. M. DeSimone, R. Lopez, *et al.*, "Biomimetic microlens array with antireflective "moth-eye" surface," *Soft Matter*, vol. 7, pp. 6404-6407, 2011.
[43] C. Pacholski, C. Morhard, J. P. Spatz, D. Lehr, M. Schulze, E.-B. Kley, *et al.*, "Antireflective subwavelength structures on microlens arrays—comparison of various manufacturing techniques," *Applied Optics*, vol. 51, pp. 8-14, 2012/01/01.
[44] S. Norrman, T. Andersson, G. Petö, and S. Somogyi, "Quantitative evolution studies of particle separation, size and shape for vapour-deposited ultrathin gold films on glass substrates," *Thin Solid Films*, vol. 77, pp. 359-366, 1981/03/20.
[45] D. Dalacu and L. Martinu, "Optical properties of discontinuous gold films: finite-size effects," *Journal of the Optical Society of America B*, vol. 18, pp. 85-92, 2001/01/01.
[46] E. S. Gadelmawla, M. M. Koura, T. M. A. Maksoud, I. M. Elewa, and H. H. Soliman, "Roughness parameters," *Journal of Materials Processing Technology*, vol. 123, pp. 133-145, 2002/04/10.
[47] J. S. Sanghera, G. Villalobos, W. Kim, S. Bayya, and I. D. Aggarwal, "Transparent Spinel Ceramic," O. S. D. Naval Research Lab, Ed., ed: Defense Technical Information Center, 2009, p. 3.
[48] M. Ramisetty, S. A. Sastri, and L. Goldman. (2013) Transparent ceramics find wide use in optics. *Photonics Spectra*. Available: https://www.photonics.com/a54521/Transparent_Ceramics_Find_Wide_Use_in_Optics
[49] J. Sanghera, S. Bayya, G. Villalobos, W. Kim, J. Frantz, B. Shaw, *et al.*, "Transparent ceramics for high-energy laser systems," *Optical Materials*, vol. 33, pp. 511-518, 2011/01/01.
[50] P. Yeh, *Optical Waves in Layered Media*. Hoboken, NJ: John Wiley & Sons, Inc., 2005.
[51] D. S. Hobbs and B. D. MacLeod, "High laser damage threshold surface relief micro-structures for anti-reflection applications," 2007, pp. 67200L-67200L-10.
[52] D. S. Hobbs, B. D. MacLeod, and E. Sabatino, "Continued advancement of laser damage resistant optically functional microstructures," in *SPIE Laser Damage*, 2012, p. 23.
[53] L. E. Busse, C. M. Florea, L. B. Shaw, J. Frantz, S. Bayya, M. K. Poutous, *et al.*, "Antireflective surface structures on optics for high energy lasers," 2014, pp. 89591L-89591L-6.
[54] M. K. Poutous, I. D. Aggarwal, A. H. Peltier, L. E. Busse, J. Frantz, B. Shaw, *et al.*, "Gradient-optical-index porous (grip) coatings by layer co-deposition and sacrificial material removal," USA Patent, 2017.
[55] I. H. Malitson, "Refraction and Dispersion of Synthetic Sapphire," *Journal of the Optical Society of America*, vol. 52, pp. 1377-1379, 1962/12/01.
[56] W. J. Tropf and M. E. Thomas, "Magnesium Aluminum Spinel (MgAl2O4) A2 - Palik, Edward D," in *Handbook of Optical Constants of Solids*, ed Burlington: Academic Press, 1997, pp. 883-894a.
[57] K. J. L. Company. (February 23, 2018). *Aluminum Oxide (Al2O3) Pieces Evaporation Materials*. Available: https://www.lesker.com/newweb/deposition_materials/depositionmaterials_evaporationmaterials_1.cfm?pgid=al6
[58] K. J. L. Company. (February 23, 2018). *Silicon Dioxide (SiO2) Pieces Evaporation Materials*. Available: https://www.lesker.com/newweb/deposition_materials/depositionmaterials_evaporationmaterials_1.cfm?pgid=si2
[59] K. J. L. Company. (February 23, 2018). *Silicon Monoxide (SiO) Pieces Evaporation Materials*. Available:

https://www.lesker.com/newweb/deposition_materials/depositionmaterials_evaporationmaterials_1.cfm?pgid=si3

[60] G. Hass and C. D. Salzberg, "Optical Properties of Silicon Monoxide in the Wavelength Region from 0.24 to 14.0 Microns*," *Journal of the Optical Society of America*, vol. 44, pp. 181-187, 1954/03/01.

[61] ISPOptics, "Guide to IR Optical Materials," ed, p. 22.

[62] T. J. Bruno and P. D. N. Svoronos, *Handbook of Basic Tables for Chemical Analysis*, 2 ed. Boca Raton, FL: CRC Press, 2004.

[63] Kyocera, "Single Crystal Sapphire," ed, 2017.

[64] T. Yanagishita, K. Nishio, and H. Masuda, "Anti-reflection structures on lenses by nanoimprinting using ordered anodic porous alumina," *Applied Physics Express*, vol. 2, p. 022001, 2009.

[65] S. S. Oh, C.-G. Choi, and Y.-S. Kim, "Fabrication of micro-lens arrays with moth-eye antireflective nanostructures using thermal imprinting process," *Microelectronic Engineering*, vol. 87, pp. 2328-2331, 2010/11/01.

[66] P.-Y. Baroni, B. Päivänranta, T. Scharf, W. Nakagawa, M. Roussey, M. Kuittinen, *et al.*, "Nanostructured surface fabricated by laser interference lithography to attenuate the reflectivity of microlens arrays," *Journal of the European Optical Society*, vol. 5, 2010.

[67] P.-L. Chen, R.-H. Hong, and S.-Y. Yang, "Hot-rolled embossing of microlens arrays with antireflective nanostructures on optical glass," *Journal of Micromechanics and Microengineering*, vol. 25, p. 095001, 2015.

[68] H. Jung and K.-H. Jeong, "Monolithic polymer microlens arrays with antireflective nanostructures," *Applied Physics Letters*, vol. 101, p. 4, 2012.

[69] K. Kunala, G. Sapkota, and M. K. Poutous, "Optical characterization of random anti-reflecting subwavelength surface structures on binary gratings," in *SPIE OPTO*, 2018, p. 7.

# APPENDIX A: PUBLICATIONS AND PRESENTATIONS

**Abigail Peltier**, Gopal Sapkota, Matthew Potter, Lynda E. Busse, Jesse A. Frantz, L. Brandon Shaw, Jasbinder S. Sanghera, Ishwar D. Aggarwal, and Menelaos K. Poutous, "Control of spectral transmission enhancement properties of random anti-reflecting surface structures fabricated using gold masking." Proc. SPIE 10115, Advanced Fabrication Technologies for Micro/Nano Optics and Photonics X, 101150B (February 20, 2017).

Menelaos K. Poutous, Ishwar D. Aggarwal, **Abigail H. Peltier**, Lynda E. Busse, Jesse Frantz, Brandon Shaw, Jas S. Sanghera, "Gradient-Optical-Index Porous (GrIP) Coatings by Layer Co-deposition and Sacrificial Material Removal", U.S. Patent Application 20170307782, filed April 2017. Patent Pending.

**Abigail Peltier Eckart,** "High-Transmission Optical Surfaces & Components", CRI Partnership Appreciation Reception Poster Presentation, December 6, 2017.

**Abigail Peltier**, Gopal Sapkota, Jason R. Case, Menelaos K. Poutous, "Polarization insensitive performance of randomly structured antireflecting planar surfaces," *Opt. Eng.* **57**(3), 037109 (2018), doi: 10.1117/1.OE.57.3.037109.

**Abigail Peltier,** Menelaos K. Poutous, "Diffraction performance of MLAs with rARSS", to be submitted April 2018.

# APPENDIX B: LIST OF OPTICAL COMPONENTS FOR MLA TESTING

Edmund Components

| Component | Stock # | Quantity |
|---|---|---|
| Microlens array 10 x 10 mm, 300 μm Pitch 0.5° Divergence | #64-478 | 2 |
| Microlens Array 10 x 10 mm, 300 μm Pitch 1° Divergence | #64-477 | 2 |
| Microlens Array 10 x 10 mm 300 μm Pitch 2° Divergence | #86-745 | 2 |
| 10x HeNe Fixed Beam Expander | #55-578 | 1 |
| 25 mm Diameter 100 mm FL, Uncoated, Laser Grade Fused Silica Plano-Convex Lens | #67-097 | 2 |
| 25 mm Diameter 50 mm FL, Uncoated, Laser Grade Fused Silica Plano-Convex Lens | #48-274 | 1 |

Thorlabs Components

| Component | Model | Quantity |
|---|---|---|
| Photodiode Power Sensor | S120C | 1 |
| Power Meter Console | PM100A | 1 |
| Graduated Ring-Actuated Iris Diaphragm | SM1D12C | 1 |
| Dual Scanning Slit Beam Profiler | BP209-IR | 1 |

Other Components

| Component | Manufacturer | Model | Quantity |
|---|---|---|---|
| 5 mW Random Polarization HeNe Laser | JDSU | 1125 | 1 |
| Power Supply for 5 mW – 7 mW HeNe Laser, 110V | JDSU | 1202-1 | 1 |

# APPENDIX C: FOURIER TRANSFORM FOR A SINGLE MICROLENS PROFILE: ANALYTICAL SOLUTION

At the far-field we have Fraunhofer diffraction:

$$U_{FF}(x_i, y_i, z_i) = \frac{1}{i\lambda z_i} e^{ikz_i} e^{ik\left(\frac{{x_i}^2+{y_i}^2}{2z_i}\right)} F\left\{g(x_0, y_0); x_0, \frac{x_i}{\lambda z_i}, y_0, \frac{y_i}{\lambda z_i}\right\}$$

The intensity is:

$$I_{FF} = (U_{FF}^* U_{FF}) = \left(\frac{1}{\lambda z_i}\right)^2 \left|F\left\{g(x_0, y_0); x_0, \frac{x_i}{\lambda z_i}, y_0, \frac{y_i}{\lambda z_i}\right\}\right|^2$$

Where $g(x_0, y_0)$ is the original object. At the near-field we have Fresnel diffraction:

$$U_{NF}(x_i, y_i, z_i) = g(x_i, y_i) * p(x_i, y_i, z_i)$$

Where $p(x, y, z)$ is the point-source transfer function. This can be reduced analytically to:

$$U_{NF}(x_i, y_i, z_i) = \frac{1}{i\lambda z_i} e^{ikz_i} e^{ik\left(\frac{{x_i}^2+{y_i}^2}{2z_i}\right)} F\left\{g(x_0, y_0) e^{ik\left(\frac{{x_0}^2+{y_0}^2}{2z_i}\right)}; x_0, \frac{x_i}{\lambda z_i}, y_0, \frac{y_i}{\lambda z_i}\right\}$$

And the intensity is:

$$I_{NF}(x_i, y_i, z_i) = \left(\frac{1}{\lambda z_i}\right)^2 \left|F\left\{g(x_0, y_0) e^{ik\left(\frac{{x_0}^2+{y_0}^2}{2z_i}\right)}; x_0, \frac{x_i}{\lambda z_i}, y_0, \frac{y_i}{\lambda z_i}\right\}\right|^2$$

In both cases $F\left\{g(x_0); x_0, \frac{x_i}{\lambda z_i}\right\}$ is the Fourier transform with respect to the input coordinates $x_0, y_0$ and the output plane coordinates (or spatial frequencies) $\frac{x_i}{\lambda z_i}, \frac{y_i}{\lambda z_i}$. For a near-field diffraction, the result can also be expressed as a Fresnel transform:

$$U_{NF}(x_i, y_i, z_i) = \frac{1}{i\lambda z_i} e^{ikz_i} \mathcal{F}\left\{g(x_0, y_0); x_0, \frac{x_i}{\lambda z_i}, y_0, \frac{y_i}{\lambda z_i}\right\}$$

$$= \frac{1}{i\lambda z_i} e^{ikz_i} \iint_{-\infty}^{\infty} g(x_0, y_0)\, e^{i\frac{\pi}{\lambda z_i}[(x_i - x_0)^2 + (y_i - y_0)^2]} dx_0 dy_0$$

If $g(x_0, y_0)$ contains a $\Pi(x_0, y_0)$, the integral limits truncate to give expressions in terms of the Fresnel Sine and Cosine Integrals

$$C(s) = \int_0^s cos\left(\frac{\pi x^2}{2}\right) dx; S(s) = \int_0^s sin\left(\frac{\pi x^2}{2}\right) dx$$

With properties:

$$\mathcal{F}\{g(x_0, y_0)\} = \big(C(s_1) + iS(s_1)\big)\big(C(s_2) + iS(s_2)\big)$$

Where $s_1$, and $s_2$ are the x and y integral limits respectively, and $\mathcal{F}\{g(x_0, y_0)\}$ is the Fresnel transform.

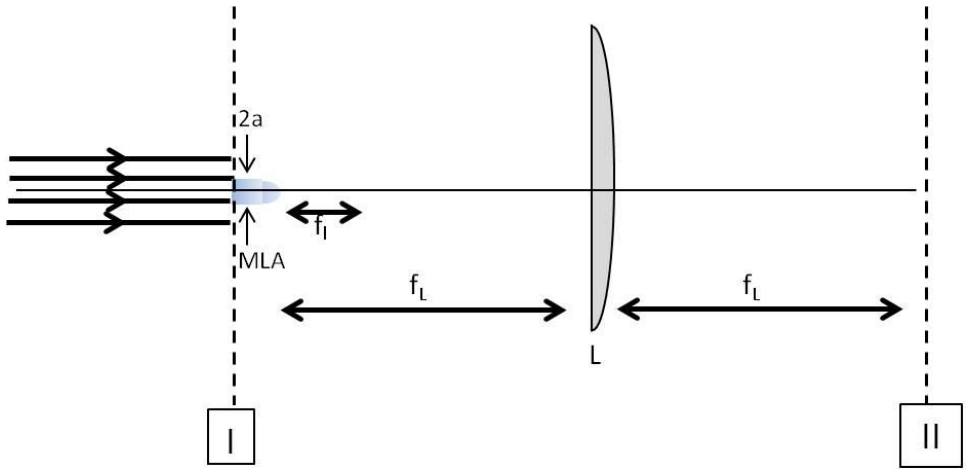


Figure 53: Schematic depicting setup used in the analytical result.

$$g(x_0, y_0) = \Pi\left(\frac{x_0}{2a}\right)\Pi\left(\frac{y_0}{2a}\right) e^{-ik\frac{\left(x_0^2+y_0^2\right)}{2f_l}}$$

$$= \Pi\left(\frac{x_0}{2a}\right) e^{-ik\frac{\left(x_0^2\right)}{2f_l}}\ \Pi\left(\frac{y_0}{2a}\right) e^{-ik\frac{\left(y_0^2\right)}{2f_l}}$$

$$= h(x_0)q(y_0)$$

Because of the symmetry of $h(x_0)$ and $q(y_0)$ we can do one of the 1D transforms and deduce solutions for both dimensions.

It has been shown that:

$$U_{II}(x_2, y_2, 2f_L) = \frac{1}{i\lambda f_L} e^{i2kf_L} F\left\{g(x_0, y_0); x_0, \frac{x_2}{\lambda f_L}, y_0, \frac{y_2}{\lambda f_L}\right\}$$

And to compute the Fourier transform:

$$F\left\{h(x_0); x_0, \frac{x_2}{\lambda f_L}\right\} = \int_{-a}^{+a} e^{-ik\frac{\left(x_0^2\right)}{2f_l}} e^{-i\pi\frac{(x_i)}{2f_l}x_0} dx_0$$

$$= e^{i\pi\left(\frac{f_l x_2^2}{\lambda f_L^2}\right)} \int_{-a}^{+a} e^{-i\left(\frac{\pi}{\lambda f_l}\right)\left(x_0 + x_2\left(\frac{f_l}{f_L}\right)\right)^2} dx_0$$

By completing the square of the exponent. Changing variables to: $\left(\frac{f_l}{f_L}\right) x_2 = X_L$ and

$\frac{1}{\lambda f_l} = \alpha_l$

$$F\{h(x_0); x_0, \alpha_l x_2\} = F\left\{h(x_0); x_0, \frac{\alpha_l f_L}{f_l} X_L\right\}$$

$$= e^{i\pi {\alpha_l}^2 {X_L}^2} \int_{-a}^{+a} e^{-i\alpha_l \pi (x_0 + X_L)^2} dx_0$$

$$= e^{i\pi {\alpha_l}^2 {X_L}^2} \left[\int_{-a}^{0} e^{-i\alpha_l \pi (x_0 + X_L)^2} dx_0 + \int_{0}^{a} e^{-i\alpha_l \pi (x_0 + X_L)^2} dx_0\right]$$

$$= e^{i\pi {\alpha_l}^2 {X_L}^2} \left[-\int_{0}^{-a} e^{-i\alpha_l \pi (x_0 + X_L)^2} dx_0 + \int_{0}^{a} e^{-i\alpha_l \pi (x_0 + X_L)^2} dx_0\right]$$

And using the Euler expression for the complex exponential:

$$= e^{i\pi {\alpha_l}^2 {X_L}^2} \left[-\int_{0}^{-a} cos(\alpha_l \pi (x_0 + X_L)^2)\, dx_0 + i\int_{0}^{-a} sin(\alpha_l \pi (x_0 + X_L)^2)\, dx_0 \right.$$

$$\left. + \int_{0}^{a} cos(\alpha_l \pi (x_0 + X_L)^2)\, dx_0 - i\int_{0}^{a} sin(\alpha_l \pi (x_0 + X_L)^2)\, dx_0\right]$$

If the argument in the cosine and sine functions is equal to: $\alpha_l \pi (x_0 + X_L)^2 = \beta^2 \frac{\pi}{2}$ we can express the result in Fresnel integral form:

$$= e^{i\pi {\alpha_l}^2 {X_L}^2} \left[ \left( \frac{-1}{\sqrt{2\alpha_l}} \right) \int_{\sqrt{2\alpha_l} X_L}^{\sqrt{2\alpha_l}(X_L - a)} cos\left(\beta^2 \frac{\pi}{2}\right) d\beta + i \left( \frac{1}{\sqrt{2\alpha_l}} \right) \int_{\sqrt{2\alpha_l} X_L}^{\sqrt{2\alpha_l}(X_L - a)} sin\left(\beta^2 \frac{\pi}{2}\right) d\beta \right.$$

$$+ \left( \frac{1}{\sqrt{2\alpha_l}} \right) \int_{\sqrt{2\alpha_l} X_L}^{\sqrt{2\alpha_l}(X_L + a)} cos\left(\beta^2 \frac{\pi}{2}\right) d\beta$$

$$\left. - i \left( \frac{1}{\sqrt{2\alpha_l}} \right) \int_{\sqrt{2\alpha_l} X_L}^{\sqrt{2\alpha_l}(X_L + a)} sin\left(\beta^2 \frac{\pi}{2}\right) d\beta \right]$$

$$= \frac{e^{i\pi {\alpha_l}^2 {X_L}^2}}{\sqrt{2\alpha_l}} \left[ - \int_0^{\sqrt{2\alpha_l}(X_L - a)} cos\left(\beta^2 \frac{\pi}{2}\right) d\beta + \int_0^{\sqrt{2\alpha_l} X_L} cos\left(\beta^2 \frac{\pi}{2}\right) d\beta \right.$$

$$+ i \int_0^{\sqrt{2\alpha_l}(X_L - a)} sin\left(\beta^2 \frac{\pi}{2}\right) d\beta - i \int_0^{\sqrt{2\alpha_l} X_L} sin\left(\beta^2 \frac{\pi}{2}\right) d\beta$$

$$+ \int_0^{\sqrt{2\alpha_l}(X_L + a)} cos\left(\beta^2 \frac{\pi}{2}\right) d\beta - \int_0^{\sqrt{2\alpha_l} X_L} cos\left(\beta^2 \frac{\pi}{2}\right) d\beta$$

$$\left. - i \int_0^{\sqrt{2\alpha_l}(X_L + a)} sin\left(\beta^2 \frac{\pi}{2}\right) d\beta + i \int_0^{\sqrt{2\alpha_l} X_L} sin\left(\beta^2 \frac{\pi}{2}\right) d\beta \right]$$

$$= \frac{e^{i\pi {\alpha_l}^2 {X_L}^2}}{\sqrt{2\alpha_l}} \left[ - \int_0^{\sqrt{2\alpha_l}(X_L - a)} cos\left(\beta^2 \frac{\pi}{2}\right) d\beta + i \int_0^{\sqrt{2\alpha_l}(X_L - a)} sin\left(\beta^2 \frac{\pi}{2}\right) d\beta \right.$$

$$\left. + \int_0^{\sqrt{2\alpha_l}(X_L + a)} cos\left(\beta^2 \frac{\pi}{2}\right) d\beta - i \int_0^{\sqrt{2\alpha_l}(X_L + a)} sin\left(\beta^2 \frac{\pi}{2}\right) d\beta \right]$$

$$= \frac{e^{i\pi\alpha_l{}^2 X_L{}^2}}{\sqrt{2\alpha_l}}\left[C\left(\sqrt{2\alpha_l}(X_L + a)\right) - C\left(\sqrt{2\alpha_l}(X_L - a)\right) + iS\left(\sqrt{2\alpha_l}(X_L - a)\right)\right.$$

$$\left. - iS\left(\sqrt{2\alpha_l}(X_L + a)\right)\right]$$

And reverting to the original coordinates gives:

$$U_{II}(x_2, y_2, 2f_L)$$

$$= \frac{e^{i2kf_L}}{i\lambda f_L} e^{i\pi\left(\frac{f_l x_2^2}{\lambda f_l^2}\right)} \left(\frac{\sqrt{\lambda f_l}}{2}\right)\left[C\left(\sqrt{\frac{2}{\lambda f_l}}\left(\left(\frac{f_l}{f_L}\right)x_2 + a\right)\right)\right.$$

$$- C\left(\sqrt{\frac{2}{\lambda f_l}}\left(\left(\frac{f_l}{f_L}\right)x_2 - a\right)\right) + iS\left(\sqrt{\frac{2}{\lambda f_l}}\left(\left(\frac{f_l}{f_L}\right)x_2 - a\right)\right)$$

$$\left. - iS\left(\sqrt{\frac{2}{\lambda f_l}}\left(\left(\frac{f_l}{f_L}\right)x_2 + a\right)\right)\right]$$

The detected intensity at $f_l$ behind the lens L is:

$$I = \left(\frac{f_l}{2f_L}\right)^2 \left[\left[C\left(\sqrt{\frac{2}{\lambda f_l}}\left(\left(\frac{f_l}{f_L}\right)x_2 + a\right)\right) - C\left(\sqrt{\frac{2}{\lambda f_l}}\left(\left(\frac{f_l}{f_L}\right)x_2 - a\right)\right)\right]^2\right.$$

$$\left. + \left[S\left(\sqrt{\frac{2}{\lambda f_l}}\left(\left(\frac{f_l}{f_L}\right)x_2 - a\right)\right) - S\left(\sqrt{\frac{2}{\lambda f_l}}\left(\left(\frac{f_l}{f_L}\right)x_2 + a\right)\right)\right]^2\right]$$